Studies of Gamma-rays from the Crab Pulsar/Nebula Complex: Spatial Morphology, Temporal Behaviour and Spectroscopy

Dissertation
zur Erlangung des Doktorgrades
des Department Physik
der Universität Hamburg

vorgelegt von

Kin Hang Yeung
aus Hongkong

Hamburg
2021

Gutachter der Dissertation:	Prof. Dr. Dieter Horns
	Prof. Dr. Olaf Reimer
Zusammensetzung der Prüfungskommission:	Prof. Dr. Marcus Brüggen
	Prof. Dr. Erika Garutti
	Prof. Dr. Dieter Horns
	Prof. Dr. Daniela Pfannkuche
	Prof. Dr. Olaf Reimer
Vorsitzende der Prüfungskommission:	Prof. Dr. Daniela Pfannkuche
Datum der Disputation:	18.01.2021
Vorsitzender Fach-Promotionsausschusses PHYSIK:	Prof. Dr. Wolfgang Hansen
Leiter des Departments Physik:	Prof. Dr. Günter Sigl
Dekan der MIN Fakultät:	Prof. Dr. Heinrich Graener

“Most people are other people. Their thoughts are someone else’s opinions, their lives a mimicry, their passions a quotation.”

Oscar Wilde

“A thousand generations live in you now. But this is your fight.”

Star Wars: The Rise of Skywalker, J.J. Abrams & Chris Terrio

Abstract

As the products of the supernova explosion SN 1054, both the Crab pulsar and its surrounding nebula harbour powerful sites of particle acceleration. They accelerate relativistic electrons which can be observed via their leptonic synchrotron and inverse-Compton emission. Such a pulsar/nebula complex is firmly detected from radio to γ-ray bands. For the Crab Nebula, the transition from synchrotron-dominated to inverse-Compton-dominated emission occurs at ≈ 1 GeV.

Through analyses on *Fermi* Large Area Telescope γ-ray data accumulated over at least 9 years of observations, we investigate the GeV–TeV spatial morphology of the inverse-Compton nebula, the temporal variability of the synchrotron nebula in the tens to hundreds of MeV energy range, and the MeV–GeV spectra of the Crab pulsar. Comparisons of our results with ground-based instruments' observations from super-GeV to TeV photon energies allow us to interpret the emission mechanisms more comprehensively.

We found that the spatial extension of the nebular inverse-Compton emission shrinks with increasing photon energy ($R_{68} \propto E_{\mathrm{IC}}^{-\alpha}$ where $\alpha = 0.155 \pm 0.035_{stat} - 0.037_{sys}$). Such a strong energy-dependence deviates from the model prediction for the dominating Thomson scattering, under an assumption of a spatially uniform seed photon field and a homogeneous magnetic field. The especially large extensions in 5–20 GeV imply that the external inverse-Compton emission is non-negligible, in addition to the synchrotron-self-Compton emission.

For the synchrotron component of the Crab Nebula, in addition to confirming the flaring behaviour, we discovered a γ-ray low-flux state with a transition time of at most ten days. This indicates that the bulk (at least three-fourth) of the synchrotron emission above 100 MeV originates in a compact volume with an apparent angular size of $\theta \approx 0\farcs4\ t_{\mathrm{var}}/(5\ \mathrm{d})$ for a given timescale of transitions between low-flux and intermediate states t_{var}. Specifically, the inner-knot feature observed near the pulsar position is discussed as a possible candidate.

For the Crab pulsar's γ-ray emission, we found an energy-dependent pulse shape and a phase-dependent spectral shape, which probably imply a multi-origin scenario involving

the polar-cap, outer-gap, and relativistic-wind regions. We propose that these three acceleration sites dominate the emissions at different phases and energies respectively. Noteworthily, we detected a relatively sharp cutoff at a relatively high energy of $\sim$8 GeV for the bridge-phase emission, and the $>$10 GeV spectrum for the second pulse peak is observed to be harder than those for other phases.

Kurzfassung

Als Produkte der Supernova-Explosion SN 1054 beherbergen sowohl der Krebspulsar als auch sein umgebender Nebel starke Orte der Teilchenbeschleunigung. Sie beschleunigen relativistische Elektronen, die durch ihre Synchrotron- und inverse Compton-Emission beobachtet werden können. Ein solcher Pulsar/Nebel-Komplex wird vom Radio- bis zum Gammastrahlen-Band fest erkannt. Für den Krebsnebel erfolgt der Übergang von der Synchrotron-dominierten zur inversen Compton-dominierten Emission bei $\approx 10^9$ eV.

Durch Analysen von Gammastrahlen Daten von *Fermi* Large Area Telescope, die über mindestens 9 Jahre Beobachtungen gesammelt wurden, untersuchen wir die räumliche GeV-bis-TeV-Morphologie des inversen Compton-Nebels, die zeitliche Variabilität des Synchrotron-Nebels in den zehn bis Hunderten von MeV Energiebereich und die MeV-bis-GeV-Spektren des Krebspulsar. Vergleiche unserer Ergebnisse mit Beobachtungen bodengestützter Instrumente von Super-GeV- zu TeV-Photonenenergien ermöglichen es uns, die Emissionsmechanismen umfassender zu interpretieren.

Wir fanden heraus, dass die räumliche Ausdehnung der inversen Compton-Emission des Nebels mit zunehmender Photonenenergie schrumpft ($R_{68} \propto E_{\mathrm{IC}}^{-\alpha}$ where $\alpha = 0.155 \pm 0.035_{stat} - 0.037_{sys}$). Eine solch starke Energieabhängigkeit weicht von der Modellvorhersage für die dominierende Thomson-Streuung unter der Annahme eines räumlich gleichmässigen Keimphotonenfeldes und eines homogenen Magnetfelds ab. Die besonders grossen Ausdehnungen in 5–20 GeV implizieren, dass die externe inverse Compton-Emission zusätzlich zur Synchrotron-Selbst-Compton-Emission nicht zu vernachlässigen ist.

Für die Synchrotron-Komponente des Krebsnebels haben wir zusätzlich zur Bestätigung des Abfackelverhaltens einen Gammastrahlen-Niedrigfluss-Zustand mit einer Übergangszeit von höchstens zehn Tagen entdeckt. Dies zeigt an, dass die Masse ($> 75\%$) der Synchrotronemission über 10^8 eV aus einem kompakten Volumen mit einer scheinbaren Winkelgrösse von $\theta \approx 0.''4\ t_{\mathrm{var}}/(5\ \mathrm{d})$ für stammt eine gegebene Zeitskala von Übergängen zwischen Niedrigfluss- und Mittel-Zuständen t_{var}. Insbesondere wird das in der Nähe der Pulsarposition beobachtete Innenknoten-Merkmal als möglicher Kandidat diskutiert.

Für die Gammastrahlen Emission des Krebspulsar fanden wir eine energieabhängige Pulsform und eine phasenabhängige Spektralform, die wahrscheinlich ein Szenario mit mehrfach Herkunftsorten implizieren, an dem die Regionen Polkappe, Aussenspalt und relativistischer Wind beteiligt sind. Wir schlagen vor, dass diese drei Beschleunigungsstellen die Emissionen jeweils in verschiedenen Phasen und Energien dominieren. Bemerkenswerterweise wird für die Brückenphasen-Emission ein relativ scharfer Cutoff bei einer relativ hohen Energie von $\sim$8 GeV beobachtet, und das für die zweite Pulsspitze beobachtete $>$10 GeV-Spektrum ist härter als das für andere Phasen.

Contents

Abstract **iv**

Kurzfassung **vi**

1 Introduction **1**
- 1.1 The Crab pulsar/nebula complex 1
- 1.2 Instrumentations of gamma-ray telescopes 2
  - 1.2.1 *Fermi* Large Area Telescope (LAT) 3
  - 1.2.2 Ground-based instruments 6
- 1.3 Scientific motivations 7
  - 1.3.1 High-energy properties of the Crab Nebula 7
    - 1.3.1.1 The inverse-Compton (IC) nebula 7
    - 1.3.1.2 The synchrotron nebula 10
  - 1.3.2 High-energy properties of the Crab pulsar 11

2 *Fermi* LAT Observations **15**
- 2.1 Criteria of Data Reduction 15
- 2.2 Analysis Scheme 17

3 The Energy-dependent Gamma-ray Morphology of the IC Nebula **23**

4 The Fast-dimming Property of the Synchrotron Nebula **35**

5 Inferring the Origins of the Pulsed Gamma-ray Emission from the Crab Pulsar **47**

6 Summary **59**

A 10-year ephemeris of the Crab pulsar **61**

B Program codes **65**
- B.1 Quantifying transitional timescales between low-flux and intermediate states 65
- B.2 Cross-calibration fit to the joint spectra of *Fermi* LAT & MAGIC 67

C Supplementary information **69**

C.1 Apparent variability of the nebular IC flux due to shot-noise 69

C.2 Moving-average analysis on a segment of the light-curve for the Synchrotron Nebula 70

C.3 Further cross-check for the low-state spectrum of the Crab Nebula 71

C.4 Supplementary information to cross-calibration fits for Crab pulsar spectra 71

C.5 Long-term temporal behaviour of the pulsed γ-ray emission 72

D Acronyms **75**

List of Figures **77**

List of Tables **79**

Bibliography **81**

List of Listings **97**

Acknowledgements **99**

Publications constituting the major parts of this thesis **101**

Dedicated to my family and friends . . . .

Chapter 1

Introduction

1.1 The Crab pulsar/nebula complex

The core-collapse supernova explosion SN 1054 was first observed on 04 July 1054, at the constellation of Taurus. Such an energetic event gave birth to the Crab Nebula and the Crab pulsar. Both these two products of the supernova explosion act as powerful particle accelerators and generate electromagnetic radiations in a broad energy range, from radio to γ-ray (e.g., Aharonian et al., 2004; Bühler and Blandford, 2014; Dubner et al., 2017). Earlier observations reveal that the entire pulsar/nebula complex is at a distance of about 2 kpc from us (Trimble, 1968, 1973). A mosaic generated from the Hubble Space Telescope observations is shown in Figure 1.1.

The Crab Nebula, like other supernova remnants (SNRs), is mainly composed of ejecta expelled during the explosion. These ejecta were swept up by an expanding shock wave. This SNR has an average angular diameter of $\sim 6'$, corresponding to a linear diameter of ~ 3.5 pc (van den Bergh, 1970). The Crab Nebula is currently expanding with an average fractional expansion rate of ≈ 0.135 % yr^{-1} (Bietenholz and Nugent, 2015).

In a central region of the SNR lies a fast-rotating compact object (with a rotational period of ≈ 34 ms; Lyne et al., 1993), which is the Crab pulsar. It spins down with a period derivative of $\approx 4.2 \times 10^{-13}$ s s^{-1} (Lyne et al., 1993). Its light cylinder radius is calculated to be $\approx 5.3 \times 10^{-11}$ pc (the spin period multiplied by the speed of light divided by 2π). As an isolated neutron star, the Crab pulsar released wind materials (electrons and positrons) interacting with and shocked by ambient medium (mainly the SNR ejecta). This led to the formation of a pulsar wind nebula (PWN) embedded within the SNR (Gaensler and Slane, 2006; Hester, 2008). The formation process of a PWN is schematically illustrated in Figure 1.2.

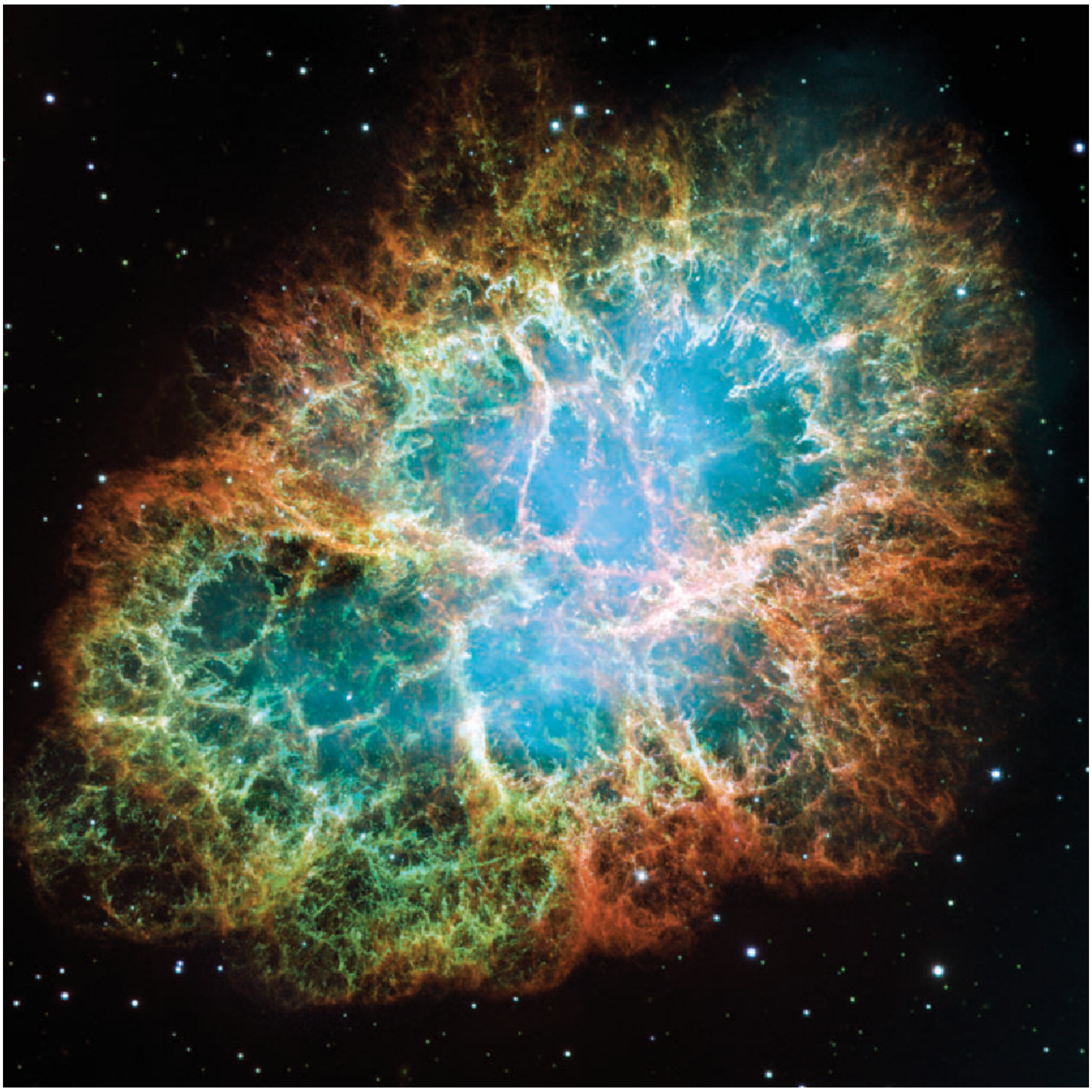

FIGURE 1.1: Mosaic image of the Crab Nebula taken by the Hubble Space Telescope (Hester, 2008). Blue, red and green respectively represent neutral oxygen ([O I]), doubly-ionized oxygen ([O III]) and singly-ionized sulfur ([S II]). Credit: NASA, ESA, J. Hester, A. Loll (ASU)

1.2 Instrumentations of gamma-ray telescopes

GeV and higher-energy γ-rays are energetic enough to penetrate lenses and mirrors with their paths unaffected. As a consequence, traditional reflecting and refracting telescopes are inapplicable to observations of such photons. Instead, two kinds of special detectors, known as pair conversion instruments and Imaging Atmospheric Cherenkov Telescopes respectively, are dedicated to the γ-ray observations.

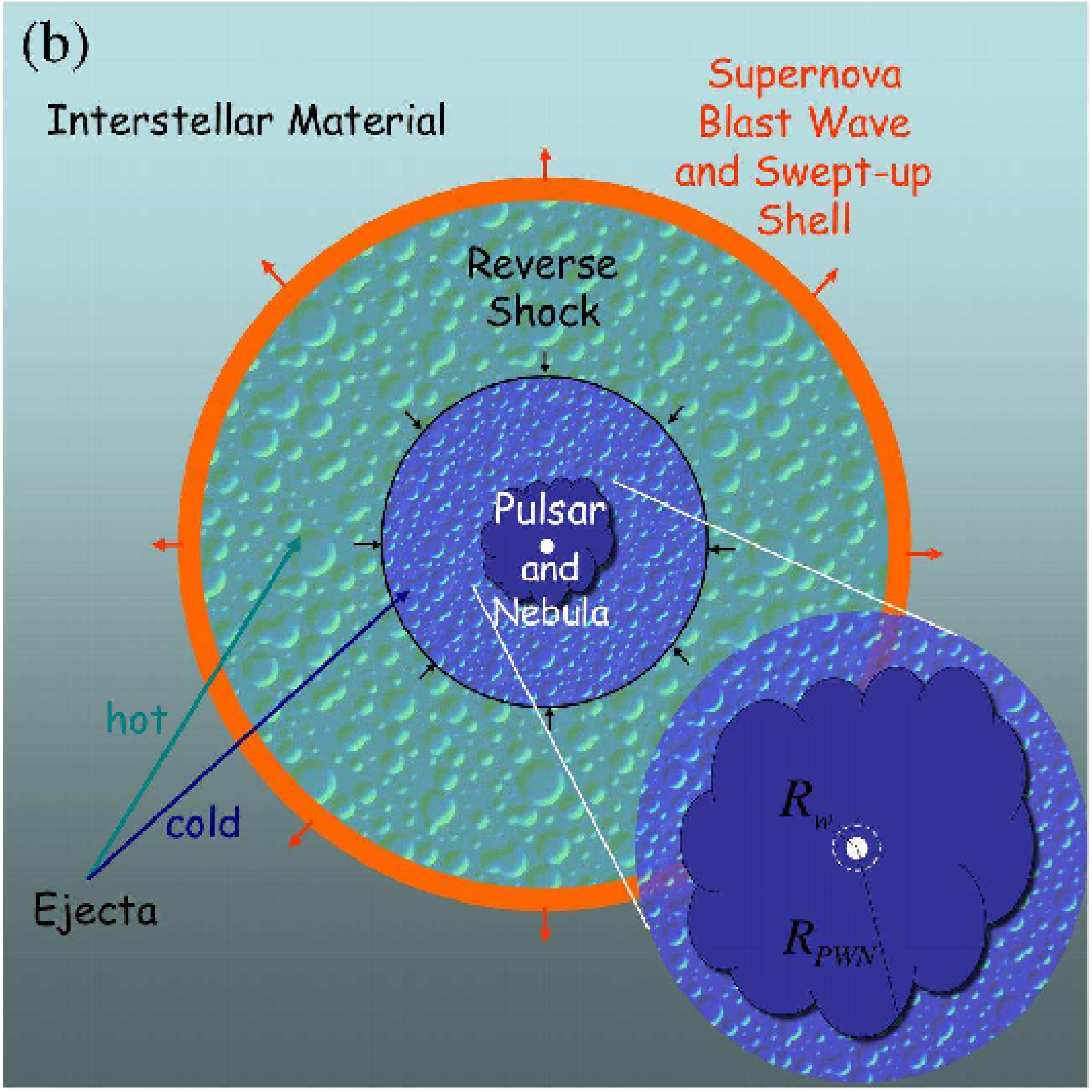

FIGURE 1.2: Formation process of a PWN (Gaensler and Slane, 2006).

1.2.1 *Fermi* Large Area Telescope (LAT)

A pair conversion instrument operates by converting the energy carried by each detected photon to the rest-mass energy and the to-be-measured kinetic energy of an electron-positron pair. Occurrence of this conversion requires the presence of other matter, usually dense metal like lead and tungsten. By measurements of the relativistic energies (i.e. the sum of rest energy and kinetic energy) of generated electrons and positrons, the telescope can reconstruct the energies of incoming photons. The principle of a pair-conversion gamma-ray telescope is schematically illustrated in Figure 1.3.

The Fermi Gamma-ray Space Telescope (FGST), which was launched into the space in 2008, is one of the largest operational pair-conversion telescopes. As an on-board telescope, it conducts an all-sky survey on astrophysical and cosmological phenomena,

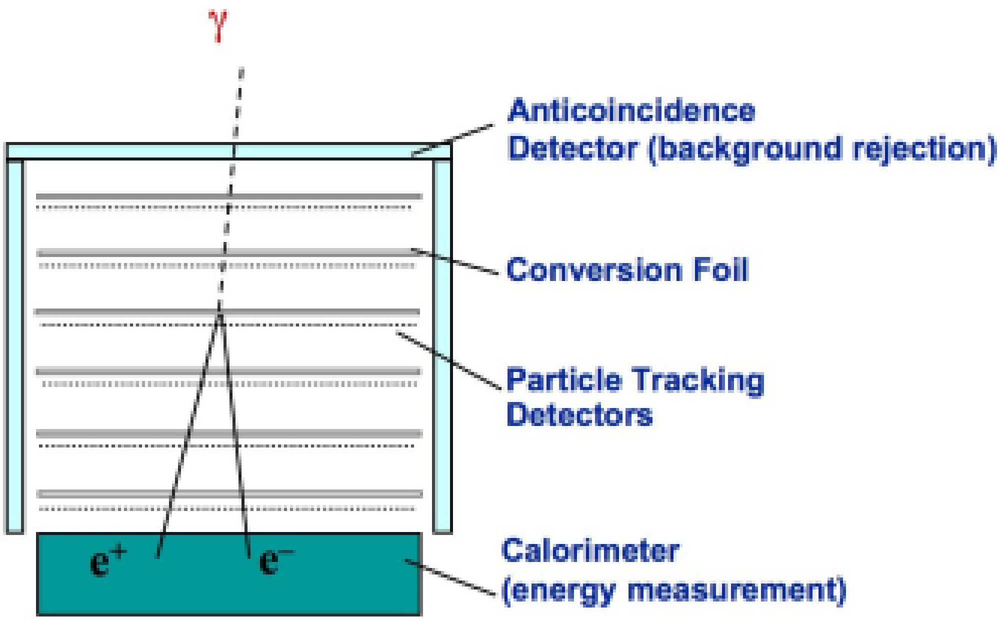

FIGURE 1.3: Schematic illustration of a pair-conversion gamma-ray telescope. Credit: glast.sites.stanford.edu (The Fermi LAT instrument: https://www-glast.stanford.edu/instrument.html)

and targets at a diversity of high-energy sources including but not limited to pulsars, PWNe and SNRs.

FGST comprises two instruments: the Large Area Telescope (LAT; Ackermann et al., 2012a) and the GLAST Burst Monitor (GBM). All works reported in this dissertation do not involve data taken by GBM, which is dedicated to observe gamma-ray bursts. The data we worked on here were all taken by LAT, which covers ∼20% of the whole sky and scans through the whole sky every 3 hours. It is considered sensitive in a photon energy range from 20 MeV to 300 GeV.

The three-dimensional structure of LAT is demonstrated in Figure 1.4. Inside LAT, there are 16 towers arranged with a configuration of a 4×4 grid. Each tower consists of:

- a tracker: It contains a stack of silicon strips for measuring the paths of the particles. Between the tracking detectors, there are thin sheets of tungsten providing environment for pair conversions;
- a calorimeter: It contains Cesium-Iodide (CsI(Tl)) detectors for measuring the energies of converted particles by converting their flashes of light (whose intensities are presumably proportional to those electron/positron energies) to voltages;
- an Anti-Coincidence Detector (ACD): It is made of plastic scintillator tiles and thus it is sensitive to charged particles (i.e. cosmic rays). Whenever it detects

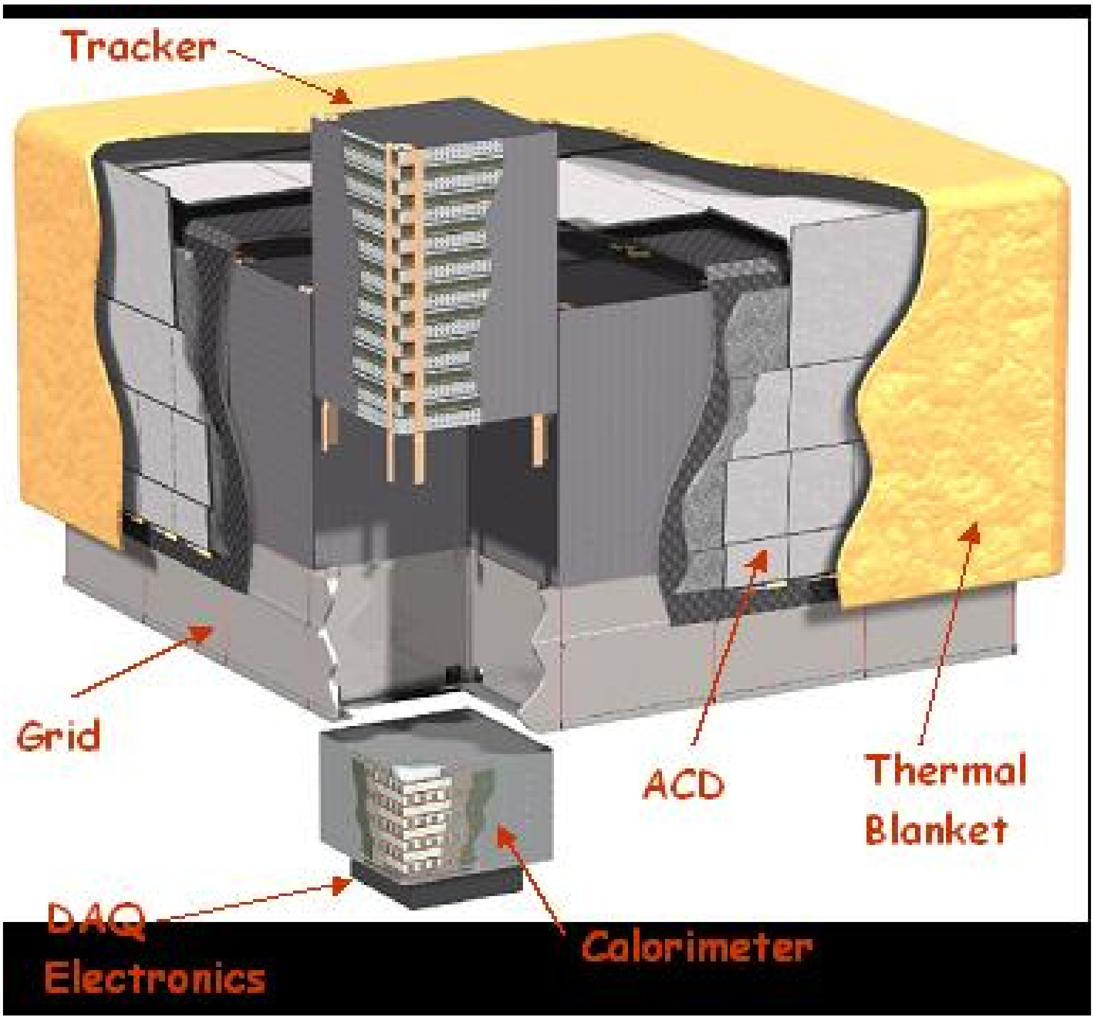

FIGURE 1.4: The three-dimensional structure of *Fermi* LAT. Credit: *Fermi* Science Support Center (Overview of the LAT: `https://fermi.gsfc.nasa.gov/ssc/data/analysis/documentation/Cicerone/Cicerone_Introduction/LAT_overview.html`)

a cosmic-ray particle which is incident on the LAT, it releases a veto signal (i.e. scintillation light); photons do not generate such signals when passing through it. This capacitates the system to distinguish between γ-rays from space and γ-rays produced by incoming cosmic-rays. The latter is identified and rejected at an efficiency of $\sim$99.999%.

The aforementioned information is adapted from webpages of *Fermi* Science Support Center [1].

Through calibrations, the uncertainty on the absolute energy scale of *Fermi* LAT was constrained to be $\leq 5\%$ (e.g., Meyer et al., 2010; Ackermann et al., 2012b).

[1]Overview of the Mission: `https://fermi.gsfc.nasa.gov/ssc/data/analysis/documentation/Cicerone/Cicerone_Introduction/mission_overview.html`; Overview of the LAT: `https://fermi.gsfc.nasa.gov/ssc/data/analysis/documentation/Cicerone/Cicerone_Introduction/LAT_overview.html`

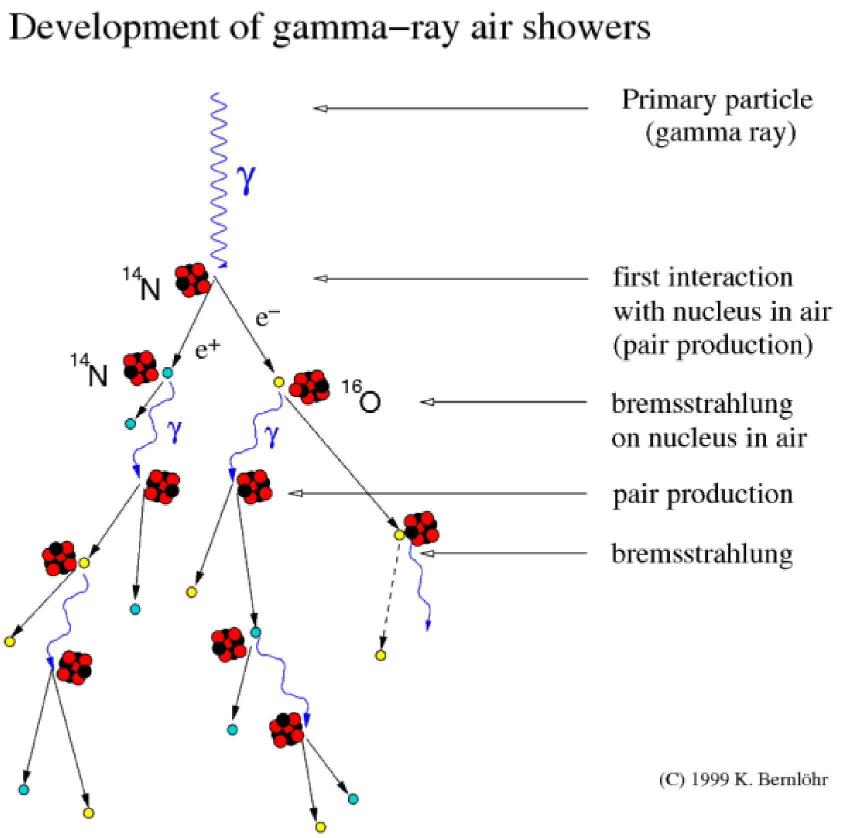

FIGURE 1.5: Schematic illustration of gamma-ray air showers. Credit: Konrad Bernlöhr (Cosmic-ray air showers: https://www.mpi-hd.mpg.de/hfm/CosmicRay/Showers.html)

1.2.2 Ground-based instruments

A common principle applied in ground-based instruments for detecting very-high-energy (VHE; >50 GeV) γ-rays is the Imaging Atmospheric Cherenkov Technique (IACT; Krennrich, 2009). Prominent IACT telescopes include High Energy Stereoscopic System (H.E.S.S.), Major Atmospheric Gamma Imaging Cherenkov Telescopes (MAGIC), and Very Energetic Radiation Imaging Telescope Array System (VERITAS).

When a VHE photon strikes an atmospheric molecule, it undergoes pair production in the vicinity of the nucleus. The primarily produced electron-positron pair is extremely energetic and immediately undergoes bremsstrahlung radiation. The generated photons, inheriting a significant portion of energy of the primary pair, undergo further pair production. As these procedures occur repeatedly, a cascade of relativistic charged particles known as an Extensive Air Shower (EAS) is initiated (see Figure 1.5 for a schematic illustration of gamma-ray air showers). An IACT telescope operates by imaging the short-lived flash of Cherenkov radiation generated by an EAS.

IACT telescopes suffer from systematic uncertainties on energy scales, which have current estimates of around 15% for the perfect atmospheric conditions (e.g., Aharonian et al., 2006; Aleksić et al., 2016). In a general case, the atmospheric quality affects IACT measurements in a number of ways. For example, the development of an EAS depends on the density profile of air molecules along its trajectory as well as the variation of the Cherenkov angle, and the loss of Cherenkov photons is affected by various absorbers and scatterings (Bernlöhr, 2000).

1.3 Scientific motivations

In this thesis, we aim to interpret the spatial, spectral and temporal properties of the Crab pulsar/nebula complex observed in γ-ray, and in turn provide insights into the relevant acceleration mechanisms of cosmic-ray particles. After all, gamma-ray has long been treated as a "smoking-gun" signature of cosmic-ray accelerations.

In this whole section, I outline the origins of our scientific motivations, which are also outlined in Section 1 of each of our refereed publications (Yeung and Horns, 2019, 2020; Yeung, 2020).

1.3.1 High-energy properties of the Crab Nebula

The exceptionally broad observable energy-range of the Crab Nebula allows us to investigate the processes of cosmic-ray acceleration supposedly occurring at the termination shock and to witness radiative energy-losses in the nebula (e.g., Spitkovsky and Arons, 2004; Fraschetti and Pohl, 2017). The discovery of its intense γ-ray emission dates back to the observations in the MeV–GeV band with the second NASA Small Astronomy Satellite (SAS-2; Kniffen et al., 1974) and in the TeV band with the Whipple Observatory 10 m reflector (Weekes et al., 1989).

Figure 1.6 shows a spectral energy distribution (SED) reconstructed for the Crab Nebula with more recent high-energy observations. It clearly demonstrates the existence of two components with different emission mechanisms, and the transition energy between domination by one component and domination by the other component is around 1 GeV.

1.3.1.1 The inverse-Compton (IC) nebula

The spectrum of the Crab Nebula observed at hard γ-ray energies (1 GeV–80 TeV) has been compared with various model calculations which use widely different approaches

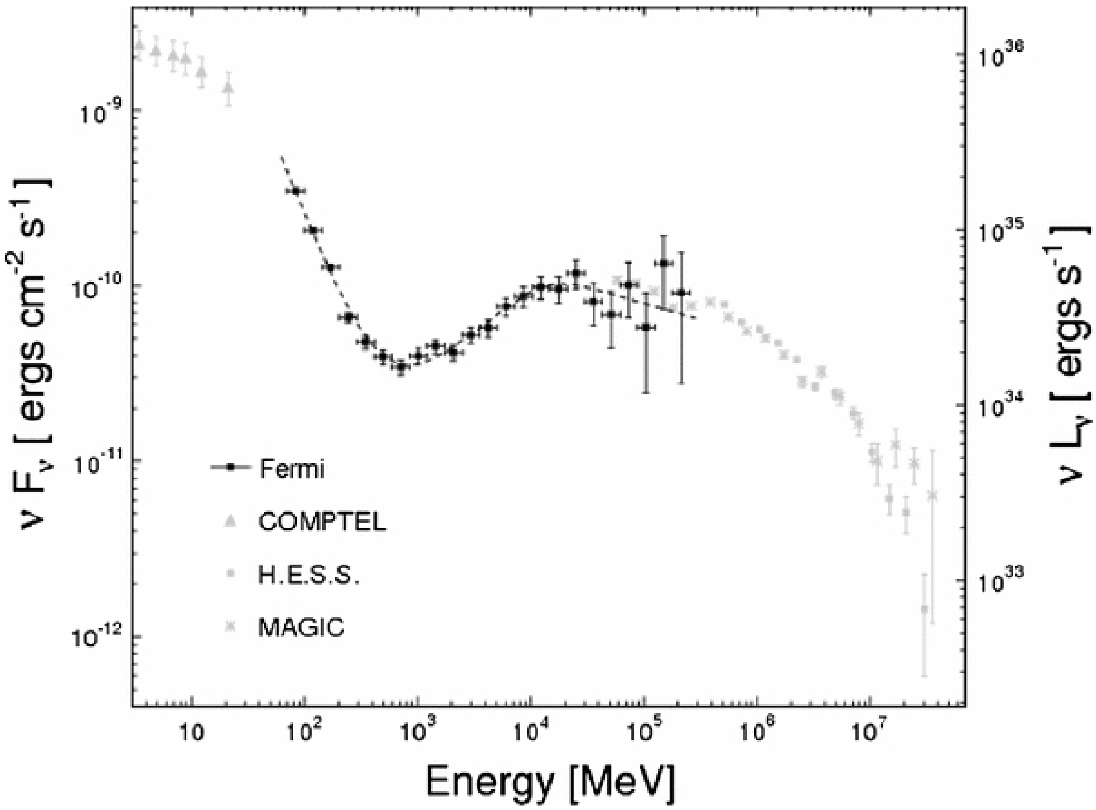

FIGURE 1.6: Previous SED of the Crab Nebula from soft γ-ray to VHE γ-ray (Buehler et al., 2012). The axis on the right side shows the isotropic luminosity. The binned spectrum averaged over the first 33 months of LAT observations is plotted. The dashed line represents the two-component (synchrotron and inverse-Compton) additive model fit to the LAT spectrum. Data from COMPTEL in the soft γ-ray band (Kuiper et al., 2001) and VHE γ-ray measurements from IACT telescopes (Aharonian et al., 2006; Zanin, 2011) are also overlaid on the plot.

(de Jager and Harding, 1992; Atoyan and Aharonian, 1996; Hillas et al., 1998; Volpi et al., 2008; Meyer et al., 2010; Martn et al., 2012). In each of these models, the gamma-ray emission in this energy range is assumed to be predominantly produced through inverse-Compton (IC) scattering of cosmic-ray electrons with synchrotron-radiated photons as initially suggested by Rees (1971) and Gunn and Ostriker (1971). Additional seed-photon field is contributed by the thermal dust emission and the cosmic microwave background (CMB).

Investigating the γ-ray spatial structure of the IC nebula is certainly important as it will provide extra indications to the concrete mechanisms of its cosmic-ray acceleration and the accompanying γ-ray emission. Among different theoretical models, the predicted characteristic size of the IC nebula differs only within a narrow range from 60" (Atoyan and Aharonian, 1996) to 80" (de Jager and Harding, 1992), despite the quite different shapes of surface brightness profiles.

A previous study by Fermi-LAT Collaboration and Biteau (2018) with *Fermi* LAT

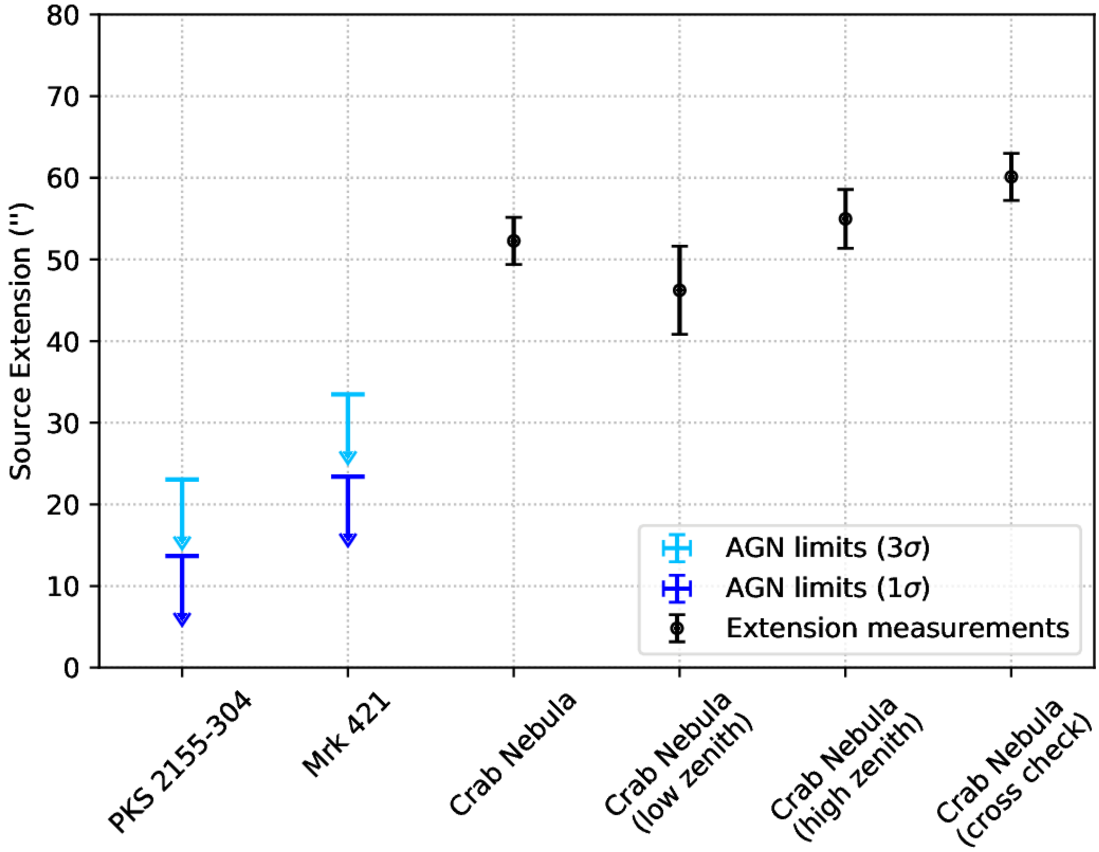

FIGURE 1.7: The gamma-ray extension sizes of the Crab IC nebula measured by H.E.S.S. under various observation conditions and analysis chains, in comparison with the upper limits on extension sizes measured for two active galactic nuclei (Holler et al., 2017; H. E. S. S. Collaboration, 2020).

indicates that an extended morphology seemingly better describes the >10 GeV γ-ray emission from the Crab Nebula compared to the point model, even when taking the systematic uncertainties related to the point spread function (PSF) into account. On the other hand, H.E.S.S. revealed that the Crab Nebula is extended in the TeV γ-ray band with a root-mean-square width of 52" (see Figure 1.7; Holler et al., 2017; H. E. S. S. Collaboration, 2020). The energy-losses of the electrons convecting in the nebula may result in the observed energy-dependent size of the synchrotron nebula. In other words, the γ-ray extension of the IC nebula, which is resulted from the spatial overlap of the electron and seed-photon distributions, is theoretically expected to decrease with increasing photon energy.

In Chapter 3 (Yeung and Horns, 2019), we investigate the γ-ray morphology of the IC nebula and its energy dependence in detail, with analysing the reduced >5 GeV LAT data accumulated over ~9.1 years and a properly refined spectral model for the Crab pulsar. We evaluated the systematic uncertainties associated with the PSF too. Then, we proceeded to compare the physics interpreted respectively from the γ-ray spectrum, the radio extension and the energy-dependent γ-ray extension.

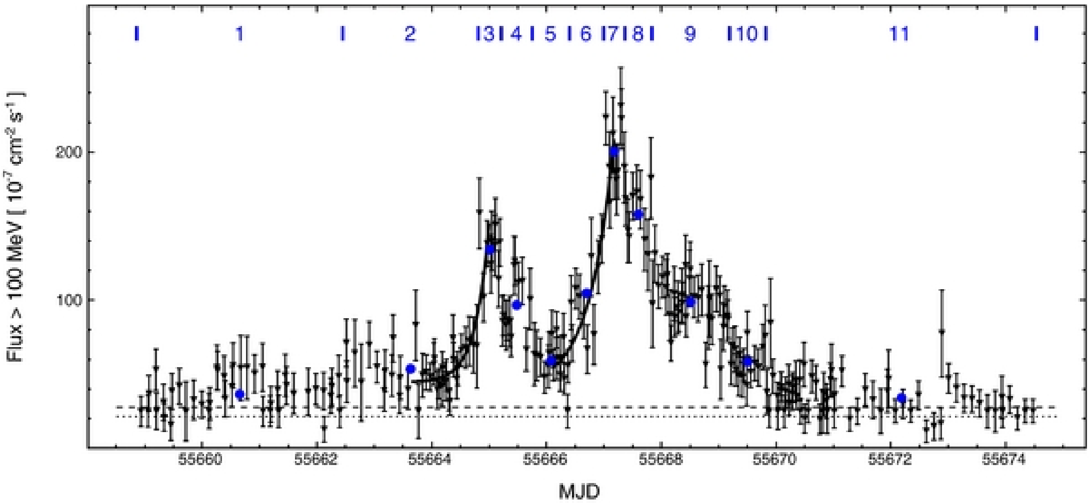

FIGURE 1.8: Time-evolution of the photon flux from the Crab integrated above 100 MeV during the 2011 April Crab flare (Buehler et al., 2012). The dotted line represents the sum of the 33-month average fluxes from the IC nebula and the pulsar. The dashed line represents the total Crab flux averaged over the 33 months. Each of the two solid black lines demonstrates the best-fit model describing the rise of a sub-flare. The blue vertical lines indicate the time intervals of each Bayesian Block during which the flux is constant within the tolerance of statistical uncertainties. The local average flux of the Crab in each block is shown by a blue marker.

1.3.1.2 The synchrotron nebula

The nebular γ-ray spectrum observed at lower energies (0.75 MeV–1 GeV) is presumably dominated by the synchrotron mechanism (Kuiper et al., 2001; Buehler et al., 2012). The spatial and spectral properties of the synchrotron nebula from optical to γ-ray bands are accurately depicted by a spherically symmetric magnetohydrodynamic model of the outflow which forms the Crab Nebula (Kennel and Coroniti, 1984).

The Crab Nebula experiences recurrent flares (roughly on a yearly basis) detected with AGILE and *Fermi* LAT, some of which raised the >100 MeV synchrotron flux by a factor of $\gtrsim 20$ (e.g., Tavani et al., 2011; Abdo et al., 2011; Buehler et al., 2012; Mayer et al., 2013). A conspicuous example of such flares which was detected in April of 2011 is demonstrated in Figure 1.8. Reinforced γ-ray emission of the synchrotron component can last for a wide variety of timescales ranging from days to weeks (Striani et al., 2013). Ongoing instability of the Crab Nebula's synchrotron emission is observed in the hard X-ray/soft γ-ray regime over a longer range of time too (Ling and Wheaton, 2003; Wilson-Hodge et al., 2011).

In Chapter 4 (Yeung and Horns, 2020), we investigate the γ-ray variability of the synchrotron nebula in detail, with analysing the reduced >60 MeV LAT data accumulated over $\sim$10 years during the off-pulse phase of the Crab pulsar. Besides the flaring periods, we consider the whole light-curve.

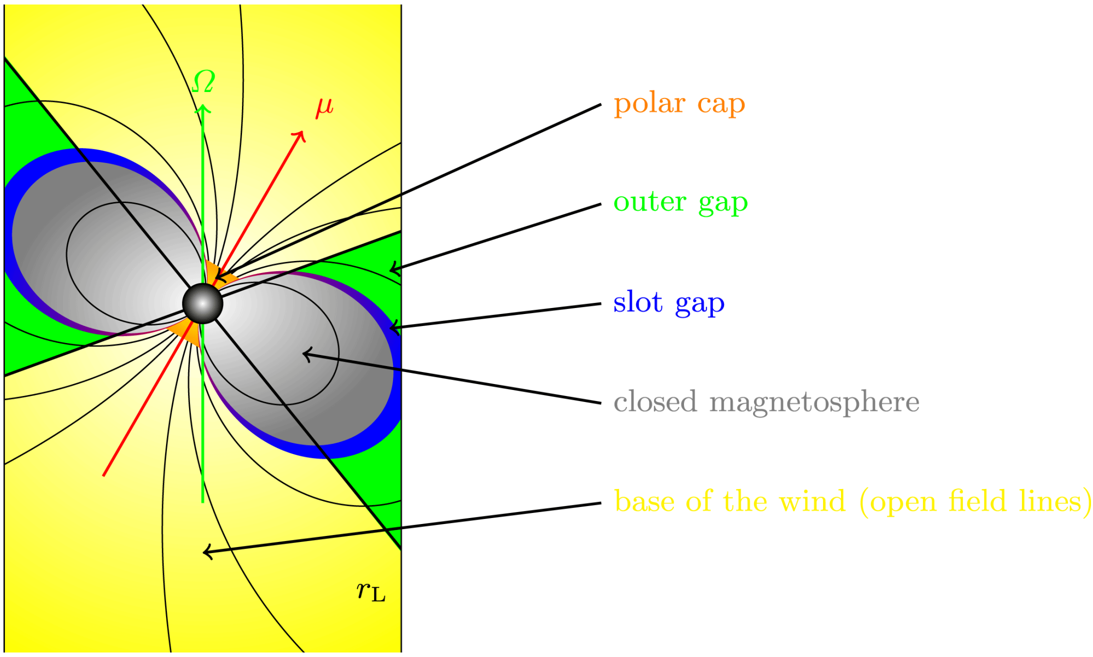

FIGURE 1.9: The structure of a pulsar magnetosphere within a light cylinder (Pétri, 2016).

1.3.2 High-energy properties of the Crab pulsar

The Crab pulsar has its γ-ray pulsation significantly detected with the on-board *Fermi* LAT (The Fermi-LAT collaboration, 2019). Uniquely, this pulsar has its pulsed emissions above 100 GeV robustly confirmed by the IACT telescopes MAGIC and VERITAS (e.g., VERITAS Collaboration et al., 2011; Aleksić et al., 2012). More recently, pulsed emission from the Crab pulsar has been detected even at $\sim$1 TeV by MAGIC (Ansoldi et al., 2016).

Figure 1.9 demonstrates the structure of a pulsar magnetosphere within a light cylinder.

According to observations with *Fermi* LAT and IACT telescopes, over a wide range of on-pulse phases, the Crab pulsar's spectrum above 10 GeV follows a rather hard power-law tail which extends beyond hundreds of GeV (Aleksić et al., 2014; Nguyen and VERITAS Collaboration, 2015; Ansoldi et al., 2016). It is certainly disfavored to explain this spectrum with polar cap models, which predict a sharp super-exponential cutoff at several GeV due to rapid pair-creations under strong magnetic field (Abdo et al., 2013). It is also disfavored to propose domination by the magnetospheric synchrotron-curvature mechanism, whose spectrum is theoretically expected to be well characterised by an exponential cutoff at several GeV due to magnetic pair-creations and/or radiation losses (Cheng et al., 1986; Romani, 1996; Muslimov and Harding, 2004; Takata et al., 2006; Tang et al., 2008).

On the other hand, it is proposed by Harding and Kalapotharakos (2015) that magnetospheric synchrotron-self-Compton (SSC) emission from leptonic pairs generated by cascades can account for the GeV spectral properties observed for the Crab pulsar. In addition, the relativistic wind located outside the light cylinder is suggested to be a responsible particle acceleration site as well (Bogovalov and Aharonian, 2000; Aharonian and Bogovalov, 2003; Aharonian et al., 2012). A more recent suggestion is that the highest energy pulsed emission could be produced in the region of the current sheet at a distance of 1–2 light cylinder radii (Harding et al., 2018) or that it even extends to tens of light cylinder radii (Arka and Dubus, 2013; Mochol and Petri, 2015), where the kinetic-energy dominated wind is presumably launched.

Noteworthily, the γ-ray pulse shape is dependent on the photon energy (Figure 1.10). Equivalently, the γ-ray spectral shape is dependent on the pulse phase (e.g., Fierro et al., 1998; Abdo et al., 2010; DeCesar, 2013). This may provide evidence that emissions at different pulse phases are dominated by different emission regions.

In Chapter 5 (Yeung, 2020), we re-investigate the γ-ray phaseograms and phase-resolved SEDs of the Crab pulsar, with the >60 MeV LAT data accumulated over $\sim$10 years. Considering our LAT results and observations of IACT telescopes synthetically, we inferred the dominating γ-ray origins for different phase intervals individually.

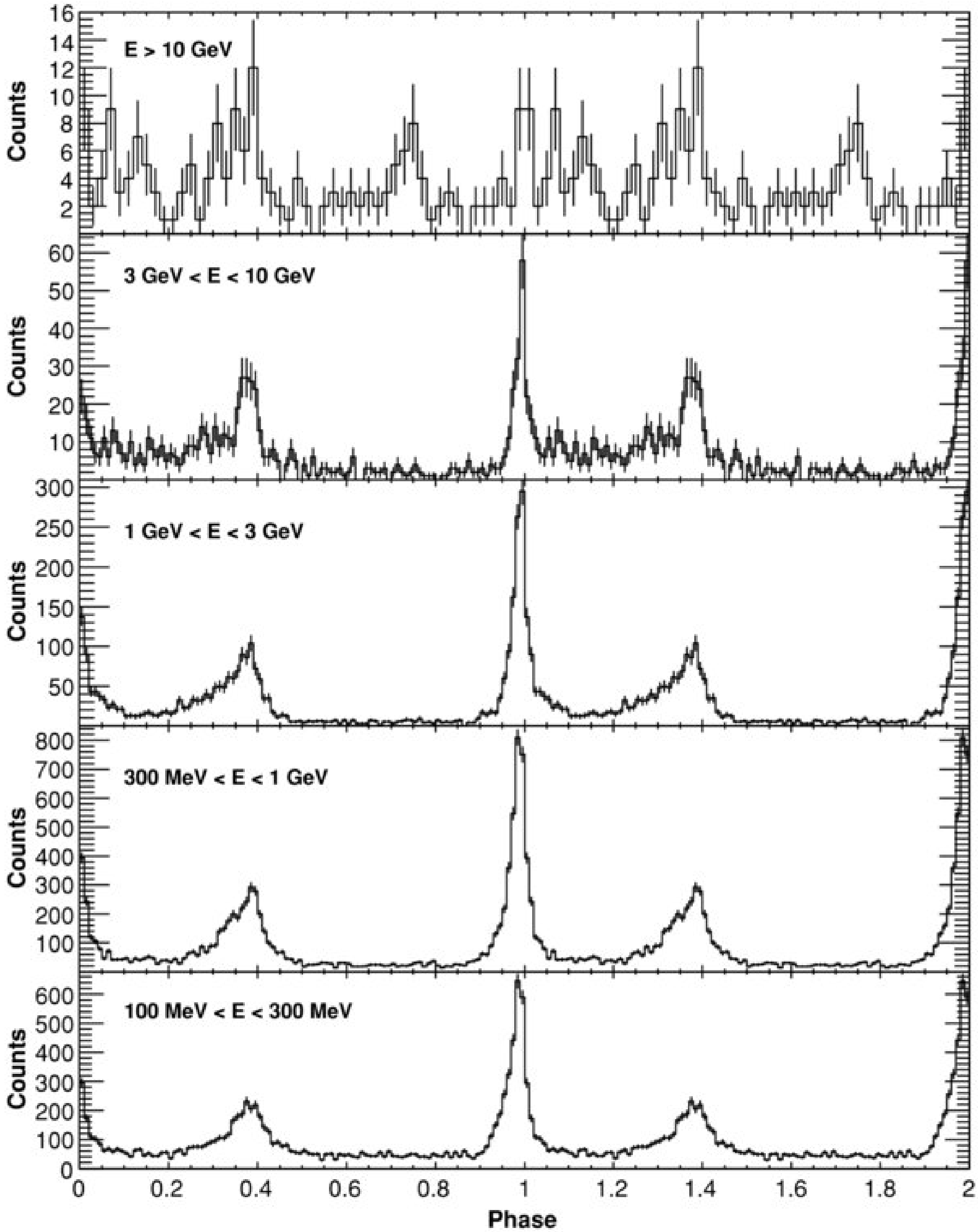

FIGURE 1.10: Previous *Fermi* LAT phaseograms of the Crab pulsar (Abdo et al., 2010). Selected photons are within an energy-dependent circular region centered at the radio pulsar position.

Chapter 2

Fermi LAT Observations

In this chapter, I describe the general data reduction criteria and analysis scheme, which are elaborated in more detail in Section 2 of each of our refereed publications (Yeung and Horns, 2019, 2020; Yeung, 2020). The consensus on the strategic details of data reductions and analyses was reached by my supervisor Prof. Dr. Dieter Horns and me.

2.1 Criteria of Data Reduction

The LAT data we worked on in this thesis are the so called Pass 8 (P8R2) data that were reprocessed with more-recent calibrations (Atwood et al., 2013). P8R2 data of LAT is classified into event classes, in descending order of both the photon statistics and extra-galactic isotropic-background contamination: "TRANSIENT", "SOURCE", "CLEAN", "ULTRACLEAN" and "ULTRACLEANVETO" [1]. Data of each class is further partitioned into "FRONT" and "BACK" types, according to the section of the LAT tracker (either the front or the back) where the conversion of each photon takes place.

A discussion about spatial and spectral resolutions of different partitions of data can be found in a webpage of SLAC [2]. The 68% containment angle of the PSF for "FRONT" events is smaller than that for "BACK" events by a factor of ∼2, at any energy in the 100 MeV–100 GeV band, as demonstrated in Figure 2.1(a). Within the same energy range, the difference in energy dispersion between "FRONT" and "BACK" data is, in general, <3% of the measured photon energy (cf. Figures 2.1(b & c)).

[1] LAT Data Products: https://fermi.gsfc.nasa.gov/ssc/data/analysis/documentation/Cicerone/Cicerone_Data/LAT_DP.html

[2] Fermi LAT Performance: http://www.slac.stanford.edu/exp/glast/groups/canda/lat_Performance.htm

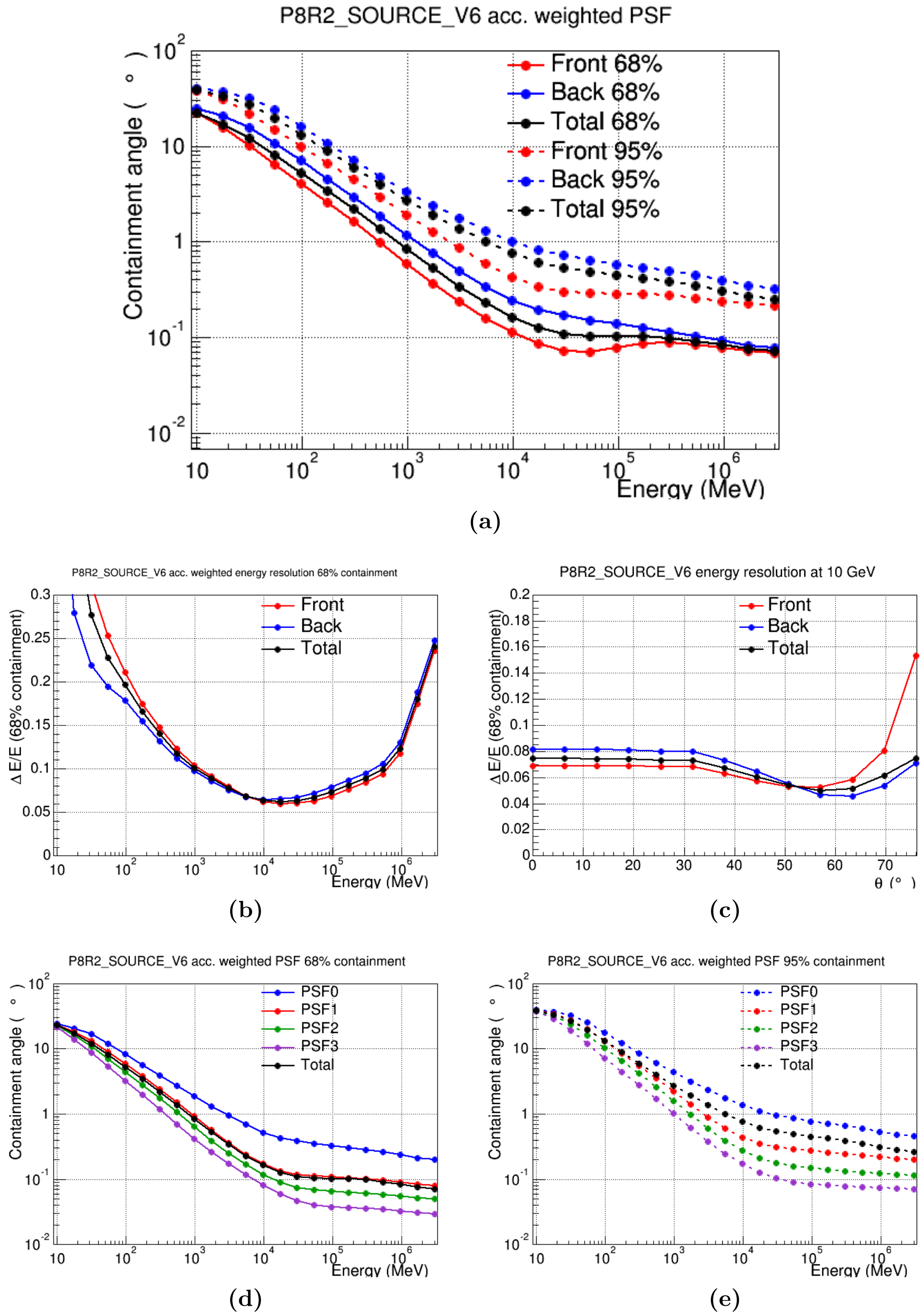

FIGURE 2.1: Spatial and spectral resolutions of LAT. Credit: SLAC [2]

Moreover, Pass 8 defines a partition of four *PSF* event types, in ascending order of the quality of the reconstructed direction: "PSF0", "PSF1", "PSF2" and "PSF3" [1], where their energy-dependent PSFs are demonstrated in Figures 2.1(d & e). Adoption of only a single *PSF* event type for an analysis tends to cause more-severe energy dispersion and in turn greater systematic uncertainties of spectral parameters. Nevertheless, for spatial analyses (i.e., morphological studies), it is recommended to cross-check the results with different spatial-quality cuts on data (for example, see Table 1 of Yeung and Horns, 2019).

With the aid of the *Fermi* Science Tools v11r5p3 package created by *Fermi* Science Support Center [3], we reduced the LAT data accumulated over at least 9 years of observations, which started at 2008 August 4, for analyses. Considering that the Crab pulsar/nebula complex is located near to the Galactic plane (with a Galactic latitude of -5.7844°), we adopt the events classified as Pass 8 "Clean" class for each analysis in order that the background is better suppressed (refer to *Fermi* Science Support Center [1]).

Throughout this dissertation, our region of interest (ROI) is centered at RA=$05^h34^m31.94^s$, Dec=$+22^\circ00'52.2$" (J2000), which is approximately the center of the Crab Nebula (Lobanov et al., 2011). We further filtered the data by accepting only the good time intervals where the ROI was observed at a zenith angle of $< 90^\circ$, for the sake of reducing the contamination from the albedo of Earth. In each phase-resolved analysis, we adopt the ten-year timing solution of the Crab pulsar provided by Dr. Matthew Kerr (documented in Appendix A) for phase cuts on data.

2.2 Analysis Scheme

By using the *Fermi* Science Tools v11r5p3 package, we performed chains of maximum-likelihood analyses. The instrument response function (IRF) "P8R2_CLEAN_V6" is adopted in analyses of the corresponding Pass 8 "Clean" class data. The flow of operation is schematically outlined in Figure 2.2 which is provided by *Fermi* Science Support Center.

In a nutshell, a maximum-likelihood analysis is about comparisons between observations and simulations. It intends to optimize the source model which describes the spectra, positions and morphologies of sources in a ROI. The likelihood L quantifies the probability that the model re-generates the data of observations, and it is maximised by

[3]Installing the Fermi Science Tools: https://fermi.gsfc.nasa.gov/ssc/data/analysis/software/v11r5p3.html; Fermi Science Tools v11r5p3 Release Notes: https://fermi.gsfc.nasa.gov/ssc/data/analysis/software/v11r5p3/ReleaseNotes_v11r5p3.txt

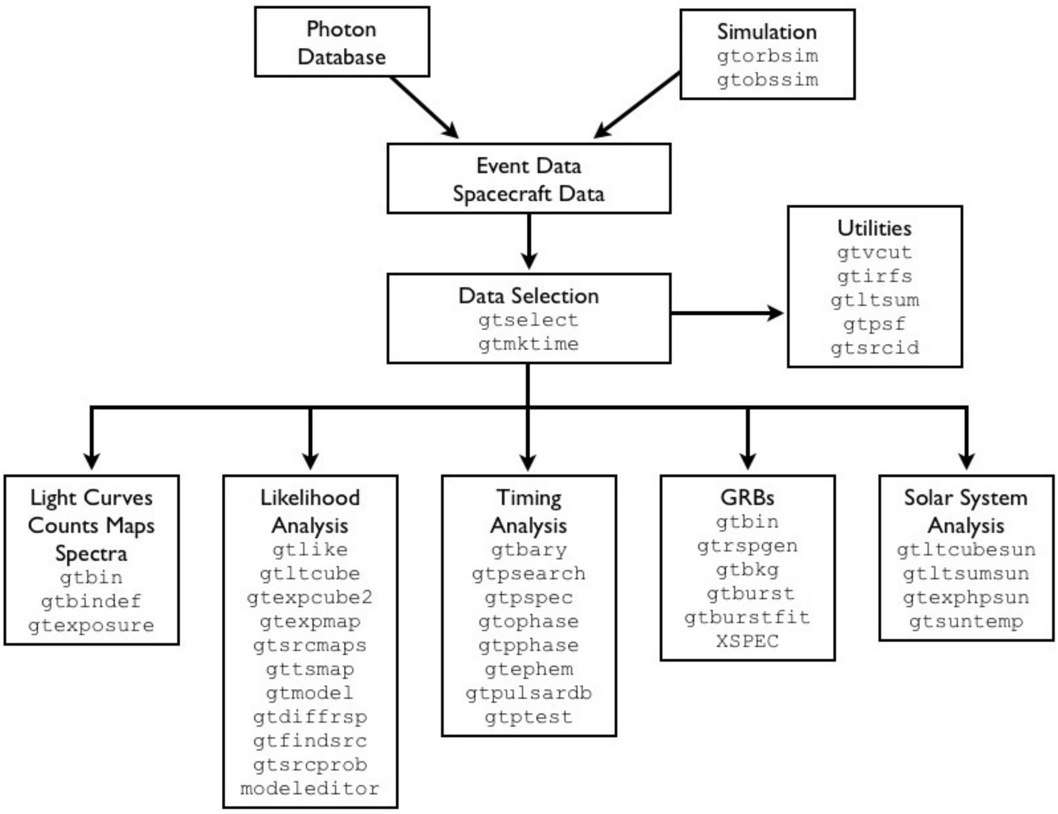

FIGURE 2.2: Flow of operation of *Fermi* Science Tools. Credit: *Fermi* Science Support Center (Overview: LAT Data Analysis Tools: https://fermi.gsfc.nasa.gov/ssc/data/analysis/scitools/overview.html)

fine-tuning the model parameters to the best-fit combination of values. More specifically, the probability p of detecting n counts in a certain bin is formulated as

$$\mathrm{p} = \mathrm{m}^{\mathrm{n}}\ \exp[-\mathrm{m}]/\mathrm{n}! \quad ,$$

where m is the model-predicted number of counts in this bin, and the likelihood L is calculated as the product of p for all bins. For model comparisons, the test-statistic (TS) is defined to quantify the significance at which an alternative hypothesis is preferred over a null hypothesis. It is formulated as

$$\mathrm{TS} = 2\ \ln\left(\frac{\mathrm{L}_{\mathrm{max},1}}{\mathrm{L}_{\mathrm{max},0}}\right) \quad ,$$

where $\mathrm{L}_{\mathrm{max},0}$ and $\mathrm{L}_{\mathrm{max},1}$ are the maximum likelihood values yielded by the null and alternative models respectively. According to Wilks' Theorem, the TS value presumably follows a Chi-Square distribution with the degree of freedom equal to the number of additional free parameters (which are free to vary only in the alternative model but are fixed in the null model). More details about likelihood analyses can be found in webpages of *Fermi* Science Support Center [4].

Taking into account the background contamination, we have included the Galactic diffuse background (gll_iem_v06.fits [5]), the isotropic background (iso_P8R2_CLEAN_V6_v06.txt) as well as all other point sources cataloged in an 8-year LAT source catalog (either FL8Y or 4FGL; The Fermi-LAT collaboration, 2019) within 25° or above from the ROI center in each source model. The distribution of the 4FGL sources of various classes is shown in Figure 2.3. It is worth mentioning that, because of the low absolute Galactic latitude of our targeted sources (the Crab Nebula and the Crab pulsar), the contamination of Galactic diffuse emission matters much more than that of extra-galactic isotropic diffuse emission.

The 4FGL catalogs exactly three point sources located within the Crab system: J0534.5+2200, J0534.5+2201i, and J0534.5+2201s, which respectively model the Crab pulsar, the IC, and synchrotron components of the Crab Nebula. In some analyses reported in this dissertation, we fix the parameters of one or two components at certain values or even remove them from the source model, for the sake of avoiding degeneracies in the fitting procedure.

In spectral analyses (especially those involving <1 GeV data), we enable the energy dispersion correction for the count spectra of the Crab pulsar and Crab Nebula as well as those of most other sources in the source model. This strategy is inspired by *Fermi* Science Support Center (refer to Figure 2.4).

[4]Likelihood Overview: https://fermi.gsfc.nasa.gov/ssc/data/analysis/documentation/Cicerone/Cicerone_Likelihood/Likelihood_overview.html; The Likelihood Functional Form: https://fermi.gsfc.nasa.gov/ssc/data/analysis/documentation/Cicerone/Cicerone_Likelihood/Likelihood_formula.html

[5]The Rescaled Galactic Interstellar Emission Model for Pass 8: https://fermi.gsfc.nasa.gov/ssc/data/access/lat/Model_details/Pass8_rescaled_model.html

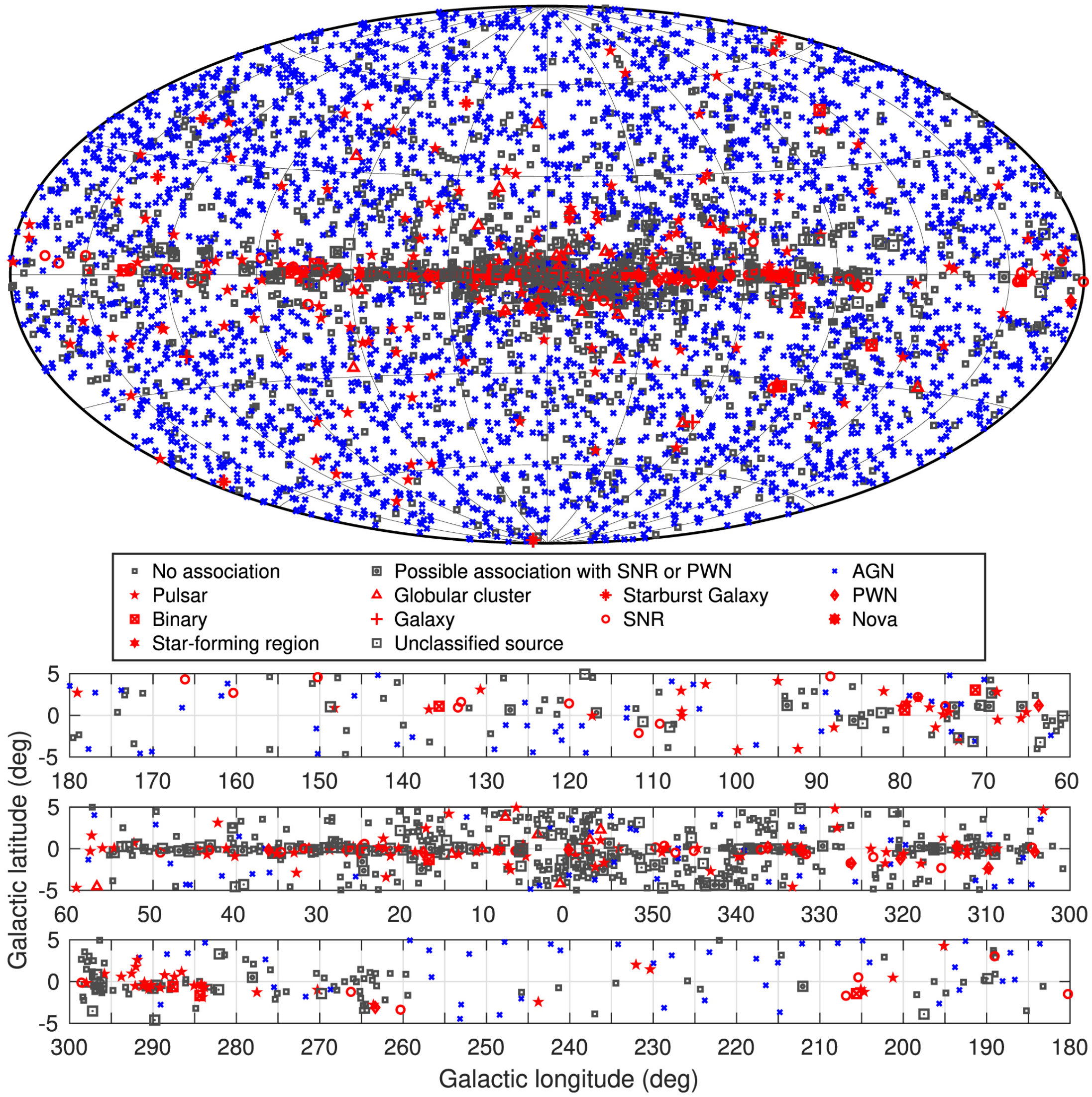

FIGURE 2.3: All-sky map (top), legend (middle) and distribution of 4FGL sources projected on the Galactic plane (bottom) (The Fermi-LAT collaboration, 2019).

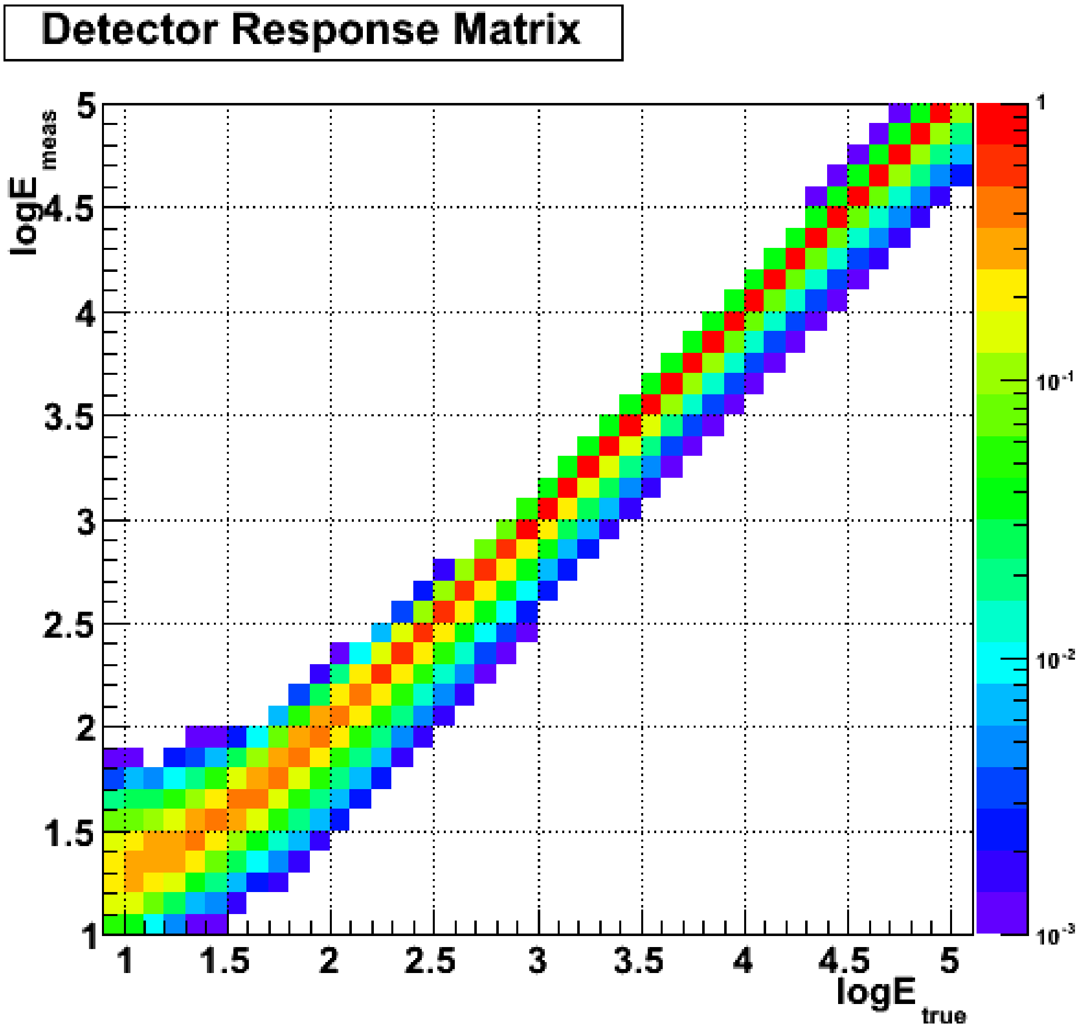

FIGURE 2.4: Detector Response Matrix internally translated by Fermitools from the energy dispersion response functions of the IRFs. Credit: *Fermi* Science Support Center (Pass 8 Analysis and Energy Dispersion: https://fermi.gsfc.nasa.gov/ssc/data/analysis/documentation/Pass8_edisp_usage.html)

Chapter 3

The Energy-dependent Gamma-ray Morphology of the IC Nebula

In this chapter, we investigate the γ-ray morphology of the IC nebula and its energy dependence in detail, with the 5 GeV–3 TeV LAT data accumulated from 2008 August 4 to 2017 September 25 and a properly refined spectral model for the Crab pulsar. We evaluated the systematic uncertainties associated with the PSF too. Then, we proceeded to compare the physics interpreted respectively from the γ-ray spectrum, the radio extension and the energy-dependent γ-ray extension. This sub-topic is directly related to our project proposal submitted to German Research Foundation (DFG), where this proposal led to our successful obtainment of the research grant HO 3305/4-1. This proposal is mainly prepared by my supervisor, with my inputs incorporated into it. Contents of this sub-topic have been published in Yeung and Horns (2019), whose publisher version is presented below *(Credit: Paul K. H. Yeung & Dieter Horns, The Astrophysical Journal, 875, 123 (2019), reproduced with permission © American Astronomical Society).*

My contributions to this publication. The concrete strategy for investigating the energy-dependence of the gamma-ray morphology of the IC nebula was created by myself based on the aforementioned project proposal, and then perfected by my supervisor Prof. Dr. Dieter Horns. I performed reductions and analyses on Fermi LAT data, with refinements suggested by my supervisor and his collaborator Dr. Joachim Hahn. The idea to establish the refined spectral model of the Crab pulsar (see Section 2 and Figure 1) was asserted by my supervisor and then implemented by me. In addition to the *Fermi* Science Tools v11r5p3 package introduced in Chapter 2, I also used the "fermipy" package [1] (Wood et al., 2017) to cross-check the 68% containment radius (R_{68}) of the IC nebula in 5–500 GeV (see Table 1), and then I used these crosscheck results to quantify the systematic uncertainty of R_{68} stemming from the analysis method, morphological model, and event selection, as suggested by my supervisor. Figure 7 is adapted by me from a high-resolution image which is provided by our guest researcher Dr. Andrei Lobanov. The ideas in Section 4 are mainly created and written by my supervisor, while I implemented the relevant fittings, calculations and checks to confirm or modify his arguments. The other parts of the manuscript are written mainly by myself. I made all figures and tables with comments from my supervisor on the formats. Through a discussion with Dr. Markus Holler, I confirmed the mathematical scaling factor for converting the root-mean-square width of the Crab Nebula's TeV γ-ray extension detected by H.E.S.S. (reported in their Holler et al., 2017) to the 68% containment radius quoted in Table 2 and Figure 6 of our Yeung and Horns (2019).

Supplementary information to Section 3.2 of this publication is presented in Appendix C.1.

Noticeably, our gamma-ray extension measurements for the Crab Nebula in this publication suffered from a deficiency stemming from the component FL8Y J0534.5+2200 which models the pulsed emission from the Crab pulsar (an erratum [2] prepared mainly by myself is submitted to ApJ for peer review). This erratum is also presented in this chapter *(Credit: Paul K. H. Yeung & Dieter Horns, The Astrophysical Journal, submitted, arXiv:1903.07527)*, following the original article.

[1] Fermipy's documentation: `https://fermipy.readthedocs.io/en/latest`

[2] The arXiv e-print version of the erratum: `https://arxiv.org/abs/1903.07527`

THE ASTROPHYSICAL JOURNAL, 875:123 (7pp), 2019 April 20 https://doi.org/10.3847/1538-4357/ab107a

The Energy-dependent γ-Ray Morphology of the Crab Nebula Observed with the *Fermi* Large Area Telescope

Paul K. H. Yeung and Dieter Horns
Institute for Experimental Physics, Department of Physics, University of Hamburg, Luruper Chaussee 149, D-22761 Hamburg, Germany; kin.hang.yeung@desy.de
Received 2019 January 31; revised 2019 March 5; accepted 2019 March 15; published 2019 April 23

Abstract

The Crab Nebula is a bright emitter of non-thermal radiation across the entire accessible range of wavelengths. The spatial and spectral structures of the synchrotron nebula are well-resolved from radio to hard X-ray emission. The unpulsed emission at GeV–TeV energies is mostly produced via inverse-Compton scattering of energetic electrons with the synchrotron-emitted photons. The spatial structure observed at these energies provides insights into the distribution of electrons and indirectly constrains the so-far unknown structure of the magnetic field in the nebula. Analyzing the Large Area Telescope (LAT) data accumulated over $\sim$9.1 yr with a properly refined model for the Crab pulsar's spectrum, we determined the 68% containment radius (R_{68}) of the Crab Nebula to be $(0.0330 \pm 0.0025_{\rm stat}{}^{+0.0012}_{-0.0075\,{\rm sys}})^{\circ}$ $(1\rlap{.}'98 \pm 0\rlap{.}'15_{\rm stat}{}^{+0\rlap{.}'07}_{-0\rlap{.}'45\,{\rm sys}})$ in the 5–500 GeV band. The estimated systematic uncertainty is based on two factors: (1) different analysis methods, morphological models and event types, and (2) the point-spread function evaluated with observations of Mkn 421. When comparing the *Fermi*-LAT and High Energy Stereoscopic System results on the spatial extension, we find evidence for an energy-dependent shrinking of the Crab Nebula's γ-ray extension ($R_{68} \propto E_{\rm IC}^{-\alpha}$, where $\alpha = 0.155 \pm 0.035_{\rm stat} - 0.037_{\rm sys}$).

Key words: gamma rays: ISM – ISM: individual objects (Crab Nebula)

1. Introduction

Isolated neutron stars are efficient particle accelerators, leading to the formation of pulsar wind nebula (PWN) systems. The extended cloud of non-thermal plasma radiates in a broad energy range, from radio to X-ray and even extends toward the highest gamma-ray energies (Aharonian et al. 2004; Bühler & Blandford 2014; Dubner et al. 2017).

The Crab Nebula is a PWN powered by a $\sim$1 kyr old pulsar (Hester 2008). It is a part of the core-collapse supernova remnant located in the constellation of Taurus, at a distance of 2 kpc (Trimble 1968). The exceptionally broad energy range observed from the Crab Nebula enables us to study the processes of particle acceleration occurring at the termination shock (e.g., Spitkovsky & Arons 2004; Fraschetti & Pohl 2017).

The discovery of its intense γ-ray emission dates back to the observations at MeV–GeV energies with the second *NASA Small Astronomy Satellite* (Kniffen et al. 1974) and at TeV energies with the Whipple Observatory 10 m reflector (Weekes et al. 1989). The observed γ-ray spectrum of the Crab Nebula from 1 GeV to 80 TeV has been compared to various model calculations that use widely different approaches (de Jager & Harding 1992; Atoyan & Aharonian 1996; Hillas et al. 1998; Volpi et al. 2008; Meyer et al. 2010; Martín et al. 2012). However, all these models are based upon the assumption that the gamma-ray emission in this energy range is predominantly produced via inverse-Compton scattering of relativistic electrons with synchrotron-radiated photons, as initially suggested by Rees (1971) and Gunn & Ostriker (1971). The spatial and spectral properties of the synchrotron nebula from optical to γ-rays are accurately described by a spherically symmetric magnetohydrodynamic model of the outflow forming the Crab Nebula (Kennel & Coroniti 1984). The thermal dust emission and the cosmic microwave background (CMB) contribute to an additional seed-photon field.

An investigation of the spatial structure of the Crab Nebula in γ-ray is certainly required, as it will provide additional insights into the concrete mechanisms of the nebula's γ-ray emission. Among the different theoretical models, the predicted characteristic size of the γ-ray nebula varies only a little from 60″ (Atoyan & Aharonian 1996) to 80″ (de Jager & Harding 1992), even though the surface brightness shape is quite different.

In a previous study by Ackermann et al. (2018) with the *Fermi* Large Area Telescope (LAT), an extended morphology seemingly fit the >10 GeV γ-ray emission from the Crab Nebula better than the point model did, even when taking the systematic uncertainties related to the point-spread function (PSF) into account. On the other hand, the High Energy Stereoscopic System (H.E.S.S.) revealed that the Crab Nebula is extended at TeV γ-ray energies with an rms width of 52″ (Holler et al. 2017).

The energy losses of the electrons diffusing outward in the nebula lead to the observed energy-dependent size of the synchrotron nebula. Similarly, the γ-ray extension of the inverse-Compton nebula may decrease with increasing energy.

In this work, we study the γ-ray morphology of the Crab Nebula and its energy dependence in detail, with the >5 GeV LAT data accumulated over $\sim$9.1 yr and a properly refined model for the Crab pulsar's spectrum. The systematic uncertainties associated with the PSF are evaluated as well. We compare the physics interpreted from the γ-ray spectrum, the radio extension, and the energy-dependent γ-ray extension.

2. Observation and Data Reduction

We perform a series of unbinned maximum-likelihood analyses for a region of interest (ROI) of 15° radius centered at R.A. = $05^{\rm h}34^{\rm m}31\rlap{.}^{\rm s}94$, decl. = $+22°00'52\rlap{.}''2$ (J2000), which is approximately the center of the Crab Nebula (Lobanov et al. 2011). We use the data of >5 GeV photon energies, registered with the LAT between 2008 August 4 and 2017 September 25.

The Astrophysical Journal, 875:123 (7pp), 2019 April 20 Yeung & Horns

The data are reduced and analyzed with the aid of the *Fermi* Science Tools v11r5p3 package. Considering that the Crab Nebula is quite close to the Galactic plane (with a Galactic latitude of $-5^\circ\!.7844$), we adopt the events classified as Pass8 "Clean" class for the analysis so as to better suppress the background. The corresponding instrument response function (IRF) "P8R2_CLEAN_V6" is used throughout the investigation. We further filter the data by accepting only the good time intervals where the ROI was observed at a zenith angle of less than 90° so as to reduce the contamination from the albedo of Earth.

In order to subtract the background contribution, we include the Galactic diffuse background (gll_iem_v06.fits), the isotropic background (iso_P8R2_CLEAN_V6_v06.txt), as well as all other point sources cataloged in the most updated *Fermi*/LAT catalog (FL8Y[1]) within 25° from the ROI center in the source model. We set free the spectral parameters of the sources within 5° from the ROI center in the analysis. For the sources beyond 5° from the ROI center, their spectral parameters are fixed to the catalog values.

The two point sources located within the nebula are cataloged as FL8Y J0534.5+2200 and FL8Y J0534.5+2201i, which respectively model the Crab pulsar and the Crab Nebula. We leave the point-source morphology of the pulsar component unchanged throughout our work. For the PWN component, we choose a point-source model as well as disk models of different radii, in order to determine the most likely morphology in each energy range we chose.

We fix the spectral parameters of FL8Y J0534.5+2200 (the pulsar component) at certain values so as to avoid degeneracies in the fitting procedure. Since it is the most contaminating "background" source in our work and its spectral fitting of a power law (PL) with a sub-exponential cutoff (PLEC) in the FL8Y catalog is dominated by the <1 GeV data, we refine its spectral model at larger energies based on the phase-folded spectrum of the Crab pulsar in 69–628 GeV measured with MAGIC (Ansoldi et al. 2016). We thereby determine a PL spectrum (see Figure 1): $\frac{dN}{dE} = 2.19 \times 10^{-10}\left(\frac{E}{\mathrm{GeV}}\right)^{-3.13}$ photons cm^{-2} s^{-1} MeV^{-1}. This PL model intersects with the catalog PLEC model at $\sim$38 GeV, below which the PL seriously underpredicts the Crab pulsar's flux. Below 38 GeV, the more recent PLEC model (FL8Y) is in a good agreement with the binned spectrum reported in the LAT Second Pulsar Catalog (Abdo et al. 2013)—see also Figure 1. Therefore, we keep the FL8Y spectrum of the Crab pulsar for energies below 38 GeV, while we replace the PLEC with the PL for other energies.

As presented in Figure 1 and Section 3.3, such a hybrid model for FL8Y J0534.5+2200 (the pulsar component) yields a >5 GeV spectrum of FL8Y J0534.5+2201i (the PWN component), which essentially matches the off-pulse spectrum reported by Buehler et al. (2012). In particular, above 20 GeV (and 40 GeV), the predicted flux of the Crab pulsar only accounts for $\leqslant 21\%$ (and $<5\%(E/40\,\mathrm{GeV})^{-1}$) of the Crab system's total flux. Clearly, the spectral model assigned to the Crab pulsar is not expected to introduce any obvious bias in our analyses for such high energies, due to its minor contribution of flux.

[1] *Fermi*-LAT 8 yr Source List: https://fermi.gsfc.nasa.gov/ssc/data/access/lat/fl8y.

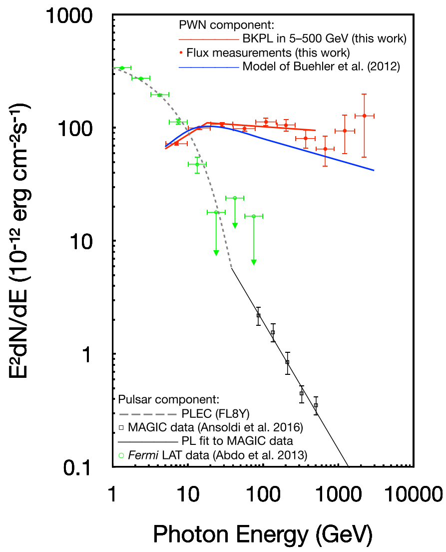

Figure 1. GeV–TeV spectral energy distribution of the Crab pulsar (in gray, black, and green) and the Crab PWN (in red and blue). The gray dashed curve represents the PLEC pulsar model in FL8Y, which is kept for energies below 38 GeV. The phase-averaged pulsar spectrum as reported in the LAT Second Pulsar Catalog (Abdo et al. 2013) is shown as green open circles for comparison. The black solid line represents the PL model fit to the 69–628 GeV pulsar spectrum measured with MAGIC (open squares), where the data are taken from Ansoldi et al. (2016). It replaces the PLEC for energies above 38 GeV. The red dots are the *Fermi*-LAT fluxes of the PWN determined in our analyses. The red line represents the maximum-likelihood broken-power-law (BKPL) model we determined for the 5–500 GeV PWN spectrum (see Section 3.3 for more details). The blue solid curve represents the off-pulse model of the PWN reported by Buehler et al. (2012).

3. Data Analysis and Results

3.1. The Centroid of the Nebula Emission

The 5–500 GeV test-statistic (TS) map is shown in Figure 2, where all FL8Y catalog sources except FL8Y J0534.5+2201i (the PWN component of the Crab system) are subtracted. The pixel size of the map is chosen that the PSF is oversampled ($0^\circ\!.001 \times 0^\circ\!.001$). Therefore, the map covers a small field of view ($0^\circ\!.014 \times 0^\circ\!.014$). The TS map demonstrates that the catalog position of FL8Y J0534.5+2201i (marked as a red cross in Figure 2) is comfortably located within the 68% error circle of the centroid for four degrees of freedom (d.o.f.), where the TS value is lower than the maximum by 4.7.[2] This centroid is within 2σ consistent with the centroid position of the radio nebula (marked as red box in Figure 2) but offset from the radio position of the Crab pulsar at a $>3\sigma$ level.

We divide the entire 5–3000 GeV band into several energy intervals: 5–10, 10–20, 20–40, 40–80, 80–150, 150–300 GeV, and 0.3–3 TeV.[3] For each spectral segment, we repeated creating the TS map with the same pixel size and field of view. The separations of Crab Nebula's centroids from the radio position of the Crab pulsar are plotted in Figure 3. The

[2] A χ^2 Distribution is assumed. There are four d.o.f. because of the four variables: R.A., decl., flux normalization, and photon index.

[3] The spectral coverages of the Galactic diffuse background (gll_iem_v06.fits) and the isotropic background (iso_P8R2_CLEAN_V6_v06.txt) are up to $\sim$0.5 TeV and $\sim$0.9 TeV, respectively. Yet, their contamination becomes negligible above 0.3 TeV. Therefore, we remove them from the source model for the 0.3–3 TeV analyses.

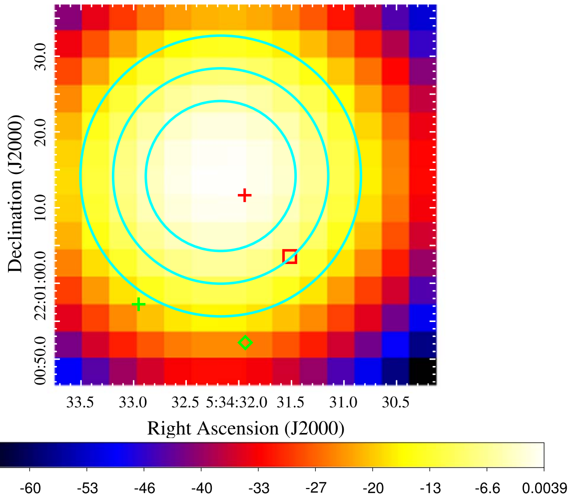

Figure 2. δTS map of the field around the Crab system in 5–500 GeV, where all FL8Y catalog sources except FL8Y J0534.5+2201i (the Crab PWN) are subtracted. The color scale represents the TS value subtracting the maximum. The pixel size ($0\overset{\circ}{.}001 \times 0\overset{\circ}{.}001$) oversamples the PSF and the map covers a field of view of $0\overset{\circ}{.}014 \times 0\overset{\circ}{.}014$. The green and red crosses represent the catalog positions of FL8Y J0534.5+2200 (the Crab pulsar) and FL8Y J0534.5+2201i, respectively. The 68%, 95%, and 99.7% error circles of the γ-ray centroid for four degrees of freedom, where the TS value is lower than the maximum by 4.7, 9.5, and 16.0 respectively (see footnote 2), are plotted in cyan (from innermost to outermost). The red square indicates the radio centroid of the Crab Nebula, which is determined from a VLA (5.5 GHz) image published in Bietenholz et al. (2004; see Section 4.2 and Figure 7 for more detail). The green diamond indicates the radio position of the Crab pulsar taken from Lobanov et al. (2011).

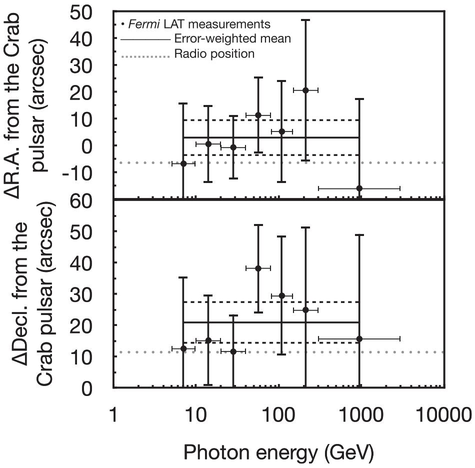

Figure 3. Difference of the Crab Nebula's centroid position from the radio position of the Crab pulsar taken from Lobanov et al. (2011) in different energy segments, along the axes of R.A. and decl., respectively. On each panel, the black solid line indicates the best-fit constant-value function (i.e., the error-weighted mean), and sandwiched between the black dashed lines is its 1σ error range. The gray dotted lines indicate the position of the Crab Nebula's radio centroid (determined from Figure 7) relative to the radio position of the Crab pulsar.

centroids in all seven segments are consistently offset from the pulsar by ΔR.A. $= (3.05 \pm 6.51)''$ ($\chi^2 \sim 1.41$ for 6 d.o.f.) and Δdecl. $= (20.86 \pm 6.51)''$ ($\chi^2 \sim 2.60$ for 6 d.o.f.).

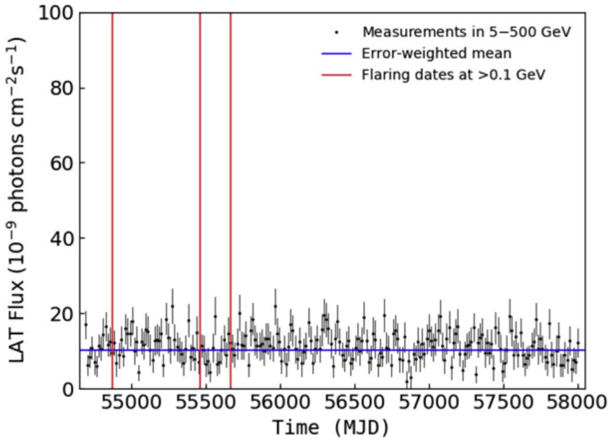

Figure 4. 5–500 GeV light curve of FL8Y J0534.5+2201i, with a bin size of 15 days. The red vertical lines indicate the dates of the flares detected at >0.1 GeV by Buehler et al. (2012). The blue solid line indicates the best-fit constant flux (i.e., the error-weighted mean).

Because *no* discrepancy among the centroids in different energy bands and the FL8Y position can be robustly claimed, we consistently leave the position of FL8Y J0534.5+2201i unchanged in subsequent analyses (i.e., there are no additional d.o.f. from the centroid position).

3.2. Variability of the Flux

We divide the first ~9.1 yr of *Fermi*-LAT observation into a number of 15 day segments, and perform an unbinned maximum-likelihood analysis for 5–500 GeV data in each individual temporal segment. Considering that the isotropic background γ-ray emission *cannot* noticeably change within a short timescale of 10 yr, we fix it at the ~9.1 yr average obtained from the full-timespan analysis, so the statistical fluctuations from the isotropic background model are avoided. The light curve of FL8Y J0534.5+2201i is shown in Figure 4.

A constant flux satisfactorily fits the entire temporal distribution with $\chi^2 \sim 256$ for 221 d.o.f. ($p(>\chi^2) = 0.05$). In order to check for significant deviations where subsequent flux points are either above or below the average, we perform an additional Wald–Wolfowitz run test (where we define two kinds of runs: runs of bins above the average and runs of those below it), the observed number of runs deviates from the expected number by only $\sim 0.6\sigma$. Furthermore, the 5–500 GeV flux of the nebula shows no correlation with the flares that enhanced its >0.1 GeV flux by a factor of >5 (see Figure 3 of Buehler et al. 2012). This is as expected because the γ-ray spectra during the flaring states have their cutoff energies well below 1 GeV (see Figures 6 and 7 of Buehler et al. 2012).

We hereby confirm that the γ-ray flares of the Crab system at lower energies do not perturb the results above 5 GeV and the 5–500 GeV flux is essentially steady. It is therefore appropriate to accept all the good time intervals between 2008 August 4 and 2017 September 25 in subsequent analyses (i.e., no further screening of data is required).

3.3. Extension and Its Energy Dependence

In order to examine whether the γ-ray emission from the PWN is spatially extended, we perform a likelihood-ratio test to quantify the significance of extension in the 5–500 GeV band.

The Astrophysical Journal, 875:123 (7pp), 2019 April 20 Yeung & Horns

Table 1
Morphological Studies for FL8Y J0534.5+2201i in 5–500 GeV with Different Analysis Methods, Morphological Models, and Event Types

Event Type	Morphological Model	Radius (deg)	R_{68} (deg)[a]	TS_{ext}[b]
		Unbinned maximum-likelihood analysis		
FRONT+BACK	Disk	0.040 ± 0.003	0.0330 ± 0.0025	57.81
		Binned maximum-likelihood analysis in "fermipy," bin size = $0.^{\circ}01$		
FRONT+BACK	Disk	$0.0385^{+0.0033}_{-0.0036}$	$0.0317^{+0.0028}_{-0.0030}$	45.50
	Gaussian	…	$0.0307^{+0.0029}_{-0.0030}$	45.59
PSF2+PSF3	Disk	$0.0400^{+0.0028}_{-0.0032}$	$0.0330^{+0.0023}_{-0.0027}$	62.34
	Gaussian	…	$0.0308^{+0.0025}_{-0.0026}$	60.93
PSF3	Disk	$0.0405^{+0.0033}_{-0.0036}$	$0.0334^{+0.0027}_{-0.0030}$	51.48
	Gaussian	…	$0.0311^{+0.0028}_{-0.0029}$	50.54

Notes.
[a] The 68% containment radius. For a disk model, it is the radius multiplied by $\sqrt{0.68}$.
[b] The $2\Delta\ln$(likelihood) between the best-fit morphology and the point-source model.

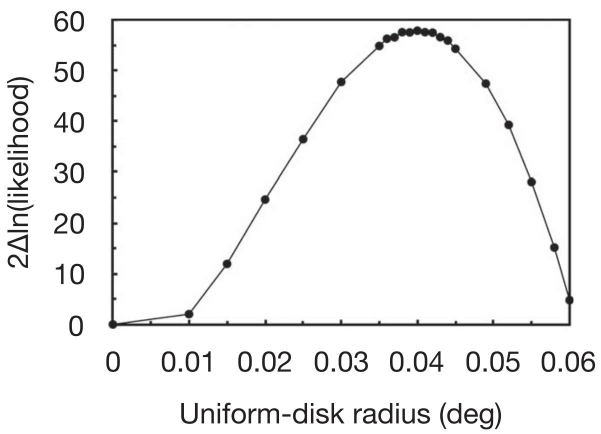

Figure 5. The $2\Delta\ln$(likelihood) in 5–500 GeV, when uniform disks of different radii replace the point-source model to be the morphology of FL8Y J0534.5+2201i.

After refinement of the Crab pulsar's spectrum, we found that a BKPL spectral model is preferred over a PL by $\sim 5.4\sigma$ for the PWN ($\Delta TS \sim 32.7$ for 2 d.o.f.). The spectrum of the PWN softens from $\Gamma_1 = 1.585 \pm 0.067$ to $\Gamma_2 = 2.047 \pm 0.036$ at $E_b = 18.05 \pm 1.60$ GeV, consistent with the spectral model determined for the off-pulse phase by Buehler et al. (2012; see Figure 1). Therefore, we assign it a BKPL spectral model. We attempt uniform-disk morphologies of different sizes as well as a point-source model on it. The $2\Delta\ln$(likelihood) of different sizes relative to the point-source model are plotted in Figure 5.

The most likely disk radius is determined to be $(0.040 \pm 0.003)^{\circ}$ and this morphology is preferred over a point-source model by $\sim 7.6\sigma$. The corresponding 68% containment radius (R_{68}; the uniform-disk radius multiplied by $\sqrt{0.68}$) of $(0.0330 \pm 0.0025)^{\circ}$ resp. $(1.98 \pm 0.15)'$ is consistent with that determined in Ackermann et al. (2018) with 1 GeV–1 TeV data and a Gaussian morphology ($0.^{\circ}030 \pm 0.^{\circ}003_{stat} \pm 0.^{\circ}007_{sys}$), within the tolerance of statistical uncertainties. Motivated by the uncertainties in the Crab pulsar's spectrum, we repeated this analysis while altering the flux normalization of the Crab pulsar by $\pm 20\%$. It turns out that the maximum-likelihood radius remains unchanged even though Γ_1 is altered by $^{+0.28}_{-0.43}$ (i.e., the spectral model of the Crab pulsar has no noticeable contribution to the systematic uncertainty).

We further verified the robustness of the 5–500 GeV result by performing binned maximum-likelihood analyses with the aid of the "fermipy" package[4] (Wood et al. 2017). We adopted a bin size of $0.^{\circ}01$, which is sufficiently small to sample the PSF as well as the γ-ray nebula. In addition to the analysis with "FRONT+BACK" data, we also performed a joint analysis with "PSF2" and "PSF3" data, and an analysis with only "PSF3" data (respectively sacrificing the photon statistics by a factor of $\sim 1/2$ and $\sim 1/4$ for better spatial resolution). For each data set we worked on, we examined both uniform-disk and Gaussian morphologies.

As can be seen in Table 1, regardless of the event type and morphological model, the values of R_{68} are all consistent with $0.^{\circ}0330 \pm 0.^{\circ}0025$ (the result of the unbinned maximum-likelihood analysis) within the tolerance of statistical uncertainties. For each event type we attempted, the two morphological models have roughly the same goodness of fit ($\Delta TS_{ext} \leqslant 1.4$), and their difference in R_{68} is negligible ($\leqslant 0.6\sigma$). Also, screening out the data partitions of poorer resolution did not lead to a noticeable drop in TS_{ext}. We hereby compute a systematic uncertainty of R_{68} of $\pm 0.^{\circ}0012$, which stems from the analysis method, morphological model, and event selection.

In order to investigate whether the γ-ray morphology changes with photon energy, we divide the entire 5–3000 GeV band in the same way as in Section 3.1. We repeat the likelihood-ratio test for each spectral segment, with a PL assigned to the PWN spectrum. The results are tabulated in Table 2. We sum up the differences between $2\ln(L_{ext,max}/L_{pt})$ and $2\ln(L_{ext,0.04}/L_{pt})$ over all seven segments, hence we get a TS value of the energy dependence of 18.2 for 7 d.o.f.. In other words, based on our *Fermi*-LAT results only, an energy-dependent morphology with the nebula size shrinking with increasing energy is preferred over a constant size by $\sim 2.5\sigma$. In addition, the PWN's flux in each segment is consistent with the off-pulse spectrum reported by Buehler et al. (2012). This confirms that the systematic uncertainties associated with the Crab pulsar's spectral model are not a serious issue.

[4] Fermipy's documentation: https://fermipy.readthedocs.io/en/latest.

Table 2
Morphological Studies for the Crab PWN in Different Energy Segments, with *Fermi*-LAT and H.E.S.S.

Energy Range (GeV)	Disk Radius (deg)	R_{68} (deg)[a]	$2\ln(L_{\mathrm{ext,max}}/L_{\mathrm{pt}})$[b]	$2\ln(L_{\mathrm{ext,0.04}}/L_{\mathrm{pt}})$[c]
Fermi-LAT result				
5–500	0.040 ± 0.003	0.0330 ± 0.0025	57.81	57.81
5–10	$0.073^{+0.010}_{-0.011}$	$0.0602^{+0.0082}_{-0.0091}$	15.75	8.40
10–20	$0.057^{+0.005}_{-0.006}$	$0.0470^{+0.0041}_{-0.0049}$	33.80	26.27
20–40	$0.034^{+0.007}_{-0.005}$	$0.0280^{+0.0058}_{-0.0041}$	11.14	10.52
40–80	$0.038^{+0.005}_{-0.006}$	$0.0313^{+0.0041}_{-0.0049}$	13.78	13.46
80–150	$0.032^{+0.010}_{-0.008}$	$0.0264^{+0.0082}_{-0.0066}$	5.06	4.40
150–300	$0.028^{+0.009}_{-0.010}$	$0.0231^{+0.0074}_{-0.0082}$	3.34	1.63
300–3000	$0.041^{+0.013}_{-0.016}$	$0.0338^{+0.0107}_{-0.0132}$	2.78	2.76
H.E.S.S. result (Holler et al. 2017)				
700–10000	…	$0.0219 \pm 0.0012_{\mathrm{stat}} \pm 0.0033_{\mathrm{sys}}$	83	…

Notes.
[a] The 68% containment radius, which is the disk radius multiplied by $\sqrt{0.68}$.
[b] The $2\Delta\ln$(likelihood) between the best-fit uniform-disk morphology and the point-source model.
[c] The $2\Delta\ln$(likelihood) between the uniform-disk morphology of a $0\overset{\circ}{.}04$ radius and the point-source model.

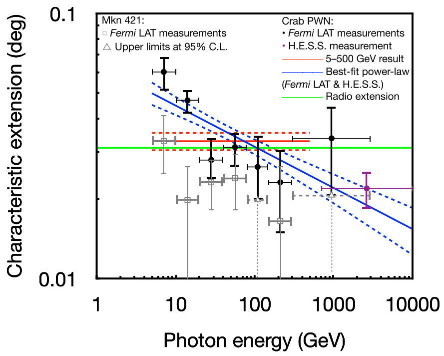

Figure 6. Characteristic extensions (defined as R_{68}; for a uniform-disk model, it is the disk radius multiplied by $\sqrt{0.68}$) of the Crab PWN in different energy segments, from the *Fermi*-LAT band to the H.E.S.S. band (in which the data are taken from Holler et al. 2017). For the H.E.S.S. bin, we take its combined uncertainty (where statistical and systematic uncertainties are added in quadrature). The red solid line indicates the characteristic extension of the energy-independent morphology (disk) fit to the 5–500 GeV emission, and sandwiched between the red dashed lines is its 1σ error range. The blue line is the power-law function that best describes the relation of characteristic extension to the photon energy, and sandwiched between the blue dashed lines is its 1σ error range. The green solid line indicates the characteristic radio extension, based on a VLA (5.5 GHz) image published in Bietenholz et al. (2004; see Section 4.2 and Figure 7 for more details about how the measurement is done). The "apparent" extensions of Mkn 421 determined through the same procedures (for evaluating the PSF) are plotted in gray, and we place upper limits of a 95% confidence level for those segments in which a point model is preferred over any uniform-disk model.

We scale the disk radii determined with LAT to R_{68}, so that they can be compared with the H.E.S.S. Gaussian extension reported by Holler et al. (2017), as plotted in Figure 6. The R_{68} in 5–500 GeV observed with *Fermi*-LAT is larger than that observed at higher energies of 0.7–10 TeV with H.E.S.S. at a $\sim 2.6\sigma$ level. A constant-value function yields a poor fit to the distribution of R_{68} ($\chi^2 \sim 29.4$ for 7 d.o.f.; i.e., it deviates from a uniform distribution at a $\sim 3.8\sigma$ level). When we fit a PL function instead, the goodness of fit greatly improves ($\chi^2 \sim 8.7$ for 6 d.o.f.). An F-test yields a statistic of ~ 14.3 for (1, 6) d.o.f., implying a chance probability of $\leqslant 0.9\%$ for the energy-dependent shrinking. Thus, the dependence of R_{68} on the photon energy (E) can be formulated as $R_{68} = (0.0357 \pm 0.0021)\left(\frac{E}{44.0\ \mathrm{GeV}}\right)^{-0.155 \pm 0.035}$ deg without any correlation between the prefactor and index.

The extension of the nebula at energies between 20 and 40 GeV appears to deviate from the PL ($\sim 1.8\sigma$). Interestingly, the energy flux of the nebula levels off to an almost flat peak at the same energy (see Figure 1).

4. Discussion

4.1. Evaluation of the PSF

Because the radius of the most likely uniform-disk morphology of FL8Y J0534.5+2201i is at least two times smaller than the 68% containment radius of the acceptance weighted PSF for all energy bands we investigate (see SLAC[5]), it is necessary to evaluate the accuracy of the IRF "P8R2_CLEAN_V6" we used. We did this by determining the "apparent" γ-ray extension of Mkn 421, a GeV- and TeV-bright blazar at high Galactic latitude, through the same procedures.

It turns out that the best-fit uniform-disk morphology of Mkn 421 in 5–500 GeV has a radius of $0\overset{\circ}{.}025^{+0\overset{\circ}{.}003}_{-0\overset{\circ}{.}004}$ with a $\mathrm{TS_{ext}}$ of 10.2, which are significantly smaller than those determined for the Crab Nebula. Also, the most likely extensions of Mkn 421 in the divided energy segments are, as overlaid in Figure 6, collectively smaller than those of the Crab Nebula. Assuming that the extension determined for Mkn 421 is purely an instrumental effect, we estimate a systematic uncertainty of $-0\overset{\circ}{.}009$ for the disk radius of the Crab Nebula in 5–500 GeV (corresponding to a systematic uncertainty of $-0\overset{\circ}{.}0074$ for R_{68}). Combining this with the effects of changing the analysis method, morphological model, event type, and Crab pulsar's spectrum, we estimate the total systematic uncertainty of R_{68} to be $\left({}^{+0.0012}_{-0.0075}\right)^{\circ}$.

[5] *Fermi*-LAT Performance: http://www.slac.stanford.edu/exp/glast/groups/canda/lat_Performance.htm.

The Astrophysical Journal, 875:123 (7pp), 2019 April 20 Yeung & Horns

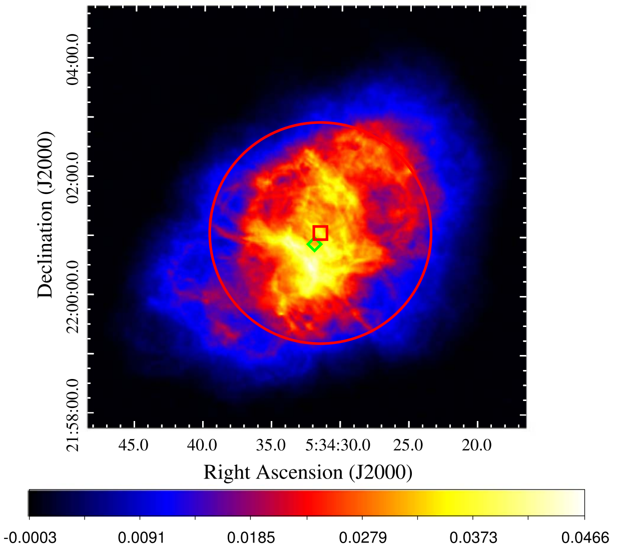

Figure 7. VLA radio (5.5 GHz) image of the Crab Nebula retrieved from Bietenholz et al. (2004). The red square indicates the intensity-weighted centroid, which is also overlaid in Figure 2. The green diamond indicates the radio position of the Crab pulsar taken from Lobanov et al. (2011). The position of the intensity-weighted centroid relative to the Crab pulsar is indicated in Figure 3. The red circle centered at the centroid indicates the 68% containment radius, which is overlaid in Figure 6.

4.2. Comparison of the γ-Ray Nebula to the Radio Nebula

In order to compare the γ-ray morphology with the radio morphology for the Crab Nebula, we retrieved a Very Large Array (5.5 GHz) image (Figure 7) published in Bietenholz et al. (2004). First of all, we determined the intensity-weighted centroid and overlaid it in Figure 2. The position of this centroid relative to the Crab pulsar is indicated in Figure 3. Then, we determined the 68% containment circle centered at this centroid; its radius is overlaid in Figure 6.

As shown, the radio centroid is on the very edge of the 95% error circle of the 5–500 GeV centroid. Both the γ-ray and radio centroids of the PWN are northward offset from the Crab Pulsar. Neglecting the systematic uncertainties associated with the PSF, the average of 5–20 GeV extensions is larger than the radio extension by $\sim 4.7\sigma$, while the >20 GeV extensions do not exceed the radio extension. Even after reducing the 5–20 GeV extensions based on the assumption that the LAT extensions determined for Mkn 421 are purely instrumental effects, their average still exceeds the radio extension by $\sim 2.9\sigma$.

The comparison of the size of the inverse-Compton nebula at 5–20 GeV with the size of the synchrotron nebula at 5 GHz provides a measure of the ratio of seed photon field energy density and magnetic field energy density. The synchrotron emission at 5 GHz is mainly produced by electrons with Lorentz factors $\gamma \approx 6 \times 10^3 \; (B/120\,\mu\mathrm{G})^{-1/2}$. The same electrons will produce inverse-Compton emission at energies below a GeV. Therefore, the ratio of $r_{\mathrm{IC}}/r_{\mathrm{Sy}}$ is a measure of the size of the seed photon field r_{seed} and the size of the magnetized nebula r_B. In a more detailed modeling approach, it is therefore necessary to include the spatial distribution of additional seed photon fields, including the emission of the dusty plasma in which the synchrotron nebula is embedded.

4.3. Comparison of the Observed Energy Dependence of the γ-Ray Extension to Theoretical Models

We found that, as the photon energy (E_{IC}) increases from 5 GeV to 10 TeV, the spatial extension of the Crab Nebula is shrinking with a PL index such that $R_{68} \propto E_{\mathrm{IC}}^{-0.155\pm0.035}$. Even after we modified the spectral distribution of the Crab Nebula's extensions based on the assumption that the LAT extensions determined for Mkn 421 are purely instrumental effects, the size of the Crab Nebula still deviates from a uniform distribution at a $\sim 2.9\sigma$ level, and it still shrinks with a PL index of ~ 0.118, which is a reasonable estimate of the systematic lower bound. Such an observed energy dependence of the γ-ray extension is comparable to the energy dependence of the size of the underlying electron distribution, which was found to be $r_e \propto \gamma^{-0.17}$ (Meyer et al. 2010) when assuming a homogeneous magnetic field. This approach effectively models the radiative cooling of electrons while expanding into the nebula.

For Thomson-type inverse-Compton scattering with $E_{\mathrm{IC}} \approx \gamma^2 \epsilon$ (where ϵ is the seed photon energy), provided that the spectral number density of the seed photon field is uniform (e.g., like the CMB), the resulting nebula size should shrink with a harder PL: $R_{68} \propto \sqrt{r_e} \propto E_{\mathrm{IC}}^{-0.17/2}$, which is similar to the energy dependence of the synchrotron nebula size. However, at energies larger than a few 100 GeV, inverse-Compton scattering with the synchrotron seed-photon field starts to be affected by Klein–Nishina effects. In the case of dominating Klein–Nishina effects, the energy dependence of the inverse-Compton nebula will proceed with $R_{68} \propto r_e \propto E_{\mathrm{IC}}^{-0.17}$. Even though this is apparently a closer match to the observed energy dependence, Klein–Nishina effects are not expected to dominate in the low-energy part ($E < 500$ GeV) covered with the measurement presented here.

The stronger energy dependence can be interpreted through a change in the ratio of energy densities $u_*(r)/u_B(r)$ in the seed-photon field u_* and in the magnetic field u_B. In turn, this may be an indication of an unknown magnetic field structure in the nebula. Further details on the interpretation of the energy dependence of the spatial extent of the inverse-Compton nebula require a careful modeling of the interplay of the spatial distribution of seed-photon and magnetic fields and of the transition between Thomson and Klein–Nishina scattering, which are beyond the scope of this publication.

5. Summary

With the proper refinement of the spectral model of the Crab pulsar, we unbiasedly determined the 68% containment radius (R_{68}) of the inverse-Compton nebula to be $(0.0330 \pm 0.0025_{\mathrm{stat}}{}^{+0.0012}_{-0.0075}{}_{\mathrm{sys}})^\circ$ ($1\rlap{.}'98 \pm 0\rlap{.}'15_{\mathrm{stat}}{}^{+0\rlap{.}'07}_{-0\rlap{.}'45}{}_{\mathrm{sys}}$) in the 5–500 GeV band. The particularly large 5–20 GeV extensions, compared with the radio size of the synchrotron nebula, imply that additional sources of seed photons (e.g., CMB and dust) must be taken into account in theoretical modeling. The strong energy dependence of its extension from 5 GeV to 10 TeV ($R_{68} \propto E_{\mathrm{IC}}^{-\alpha}$, where $\alpha = 0.155 \pm 0.035_{\mathrm{stat}} - 0.037_{\mathrm{sys}}$), deviates from the synchrotron nebula, where the size shrinks with $E_{\mathrm{Sy}}^{-0.085}$. Possible explanations have been considered (transition from Thomson to Klein–Nishina regime and a non-uniform magnetic field). While the former explanation appears to be unrealistic, the latter is a well-known feature of the downstream flow, as expected for the Crab Nebula (Kennel & Coroniti 1984).

P.K.H.Y. acknowledges the support of the DFG under the research grant HO 3305/4-1. We thank J. Hahn and M. Holler for useful discussions. We thank the anonymous referee for very useful comments that helped to improve the manuscript.

Software: fermipy (Wood et al. 2017) and *Fermi* Science Tools (v11r5p3).

ORCID iDs

Paul K. H. Yeung https://orcid.org/0000-0003-3476-022X
Dieter Horns https://orcid.org/0000-0003-1945-0119

References

Abdo, A. A., Ajello, M., Allafort, A., et al. 2013, ApJS, 208, 17
Ackermann, M., Ajello, M., Baldini, L., et al. 2018, ApJS, 237, 32
Aharonian, F., Akhperjanian, A., Beilicke, M., et al. 2004, ApJ, 614, 897
Ansoldi, S., Antonelli, L. A., Antoranz, P., et al. 2016, A&A, 585, A133
Atoyan, A. M., & Aharonian, F. A. 1996, MNRAS, 278, 525
Bietenholz, M. F., Hester, J. J., Frail, D. A., & Bartel, N. 2004, ApJ, 615, 794
Buehler, R., Scargle, J. D., Blandford, R. D., et al. 2012, ApJ, 749, 26
Bühler, R., & Blandford, R. 2014, RPPh, 77, 066901
de Jager, O. C., & Harding, A. K. 1992, ApJ, 396, 161
Dubner, G., Castelletti, G., Kargaltsev, O., et al. 2017, ApJ, 840, 82
Fraschetti, F., & Pohl, M. 2017, MNRAS, 471, 4856
Gunn, J. E., & Ostriker, J. P. 1971, ApJ, 165, 523
Hester, J. J. 2008, ARA&A, 46, 127
Hillas, A. M., Akerlof, C. W., Biller, S. D., et al. 1998, ApJ, 503, 744
Holler, M., Berge, D., Hahn, J., et al. 2017, ICRC (Busan), 35, 676
Kennel, C. F., & Coroniti, F. V. 1984, ApJ, 283, 710
Kniffen, D. A., Hartman, R. C., Thompson, D. J., Bignami, G. F., & Fichtel, C. E. 1974, Natur, 251, 397
Lobanov, A. P., Horns, D., & Muxlow, T. W. B. 2011, A&A, 533, A10
Martín, J., Torres, D. F., & Rea, N. 2012, MNRAS, 427, 415
Meyer, M., Horns, D., & Zechlin, H.-S. 2010, A&A, 523, A2
Rees, M. J. 1971, NPhS, 230, 55
Spitkovsky, A., & Arons, J. 2004, ApJ, 603, 669
Trimble, V. 1968, AJ, 73, 535
Volpi, D., Del Zanna, L., Amato, E., & Bucciantini, N. 2008, A&A, 485, 337
Weekes, T. C., Cawley, M. F., Fegan, D. J., et al. 1989, ApJ, 342, 379
Wood, M., Caputo, R., Charles, E., et al. 2017, ICRC (Busan), 301, 824

Draft version February 1, 2021
Typeset using LaTeX default style in AASTeX63

Erratum: "The Energy-dependent γ-ray Morphology of the Crab Nebula Observed with the *Fermi* Large Area Telescope" (2019, ApJ, 875, 123)

Paul K. H. Yeung[1] and Dieter Horns[1]

[1] Institute for Experimental Physics, Department of Physics, University of Hamburg, Luruper Chaussee 149, D-22761 Hamburg, Germany

(Received February 1, 2021)

Submitted to ApJ

In our original article Yeung & Horns (2019), the superimposed spatial model assigned to the whole Crab (i.e. a superposition of a point component [pulsar] and an extended component [nebula]) was following the analysis scheme of Fermi-LAT Collaboration & Biteau (2018). Nevertheless, there is a deficiency of our γ-ray extension measurements for the Crab Nebula, which is stemming from the Crab pulsar's model. There is not only deviation in spectral modelling for the pulsar component, but also inaccuracy in convolving the pulsar's spatial morphology (i.e. the point source morphology) with the PSF. According to Figure 3 of our Yeung (2020), the pulsar's differential flux accounts for $\sim$(15–72)% of the Crab's total differential flux from 5 to 40 GeV. Therefore, the aforementioned systematic effect associated with the pulsar component was particularly large for the 5–40 GeV extension measurements reported in our original article.

With regards to this issue, we perform follow-up checks for the 5–40 GeV extension sizes by selecting only off-pulse phase data for analyses and, accordingly, removing the pulsar component from the source model. We adopt the timing solution of the Crab pulsar provided by M. Kerr. We define the off-pulse phase in the same way as in our Yeung & Horns (2020). We perform binned maximum-likelihood analyses, with an angular bin size of 0.01°, on P8R3 data accumulated over the first 10 years of observations. We adopt the 4FGL point source catalogue (The Fermi-LAT collaboration 2019), the Galactic diffuse model "gll_iem_v07" and the isotropic diffuse model "iso_P8R2_CLEAN_V6_v07". Other details of data reduction criteria and analysis procedures roughly follow our original article.

It turns out that the disk radius of the Crab Nebula is revised to be $0.041^{+0.016}_{-0.025}$, $0.070^{+0.008}_{-0.009}$ and $0.042^{+0.009}_{-0.011}$ deg in 5–10, 10–20 and 20–40 GeV respectively. Moreover, the revised disk radii in the combined 5–20 GeV segment and the broad 5–500 GeV band are $0.064^{+0.007}_{-0.008}$ and $0.047^{+0.005}_{-0.006}$ deg respectively.

As demonstrated in Figure 1, these revised results do not throw doubt on the conclusions on excess 5–20 GeV extensions (relative to the radio extension) and on energy-dependent shrinking in our original paper.

REFERENCES

Fermi-LAT Collaboration, & Biteau, J. 2018, ArXiv e-prints, 1804, arXiv:1804.08035. http://adsabs.harvard.edu/abs/2018arXiv180408035F

H. E. S. S. Collaboration. 2020, Nature Astronomy, 4, 167, doi: 10.1038/s41550-019-0910-0

The Fermi-LAT collaboration. 2019, arXiv e-prints, arXiv:1902.10045. https://arxiv.org/abs/1902.10045

Yeung, P. K. H. 2020, A&A, 640, A43, doi: 10.1051/0004-6361/202038166

Yeung, P. K. H., & Horns, D. 2019, ApJ, 875, 123, doi: 10.3847/1538-4357/ab107a

—. 2020, A&A, 638, A147, doi: 10.1051/0004-6361/201936740

Corresponding author: Paul K. H. Yeung
kin.hang.yeung@desy.de

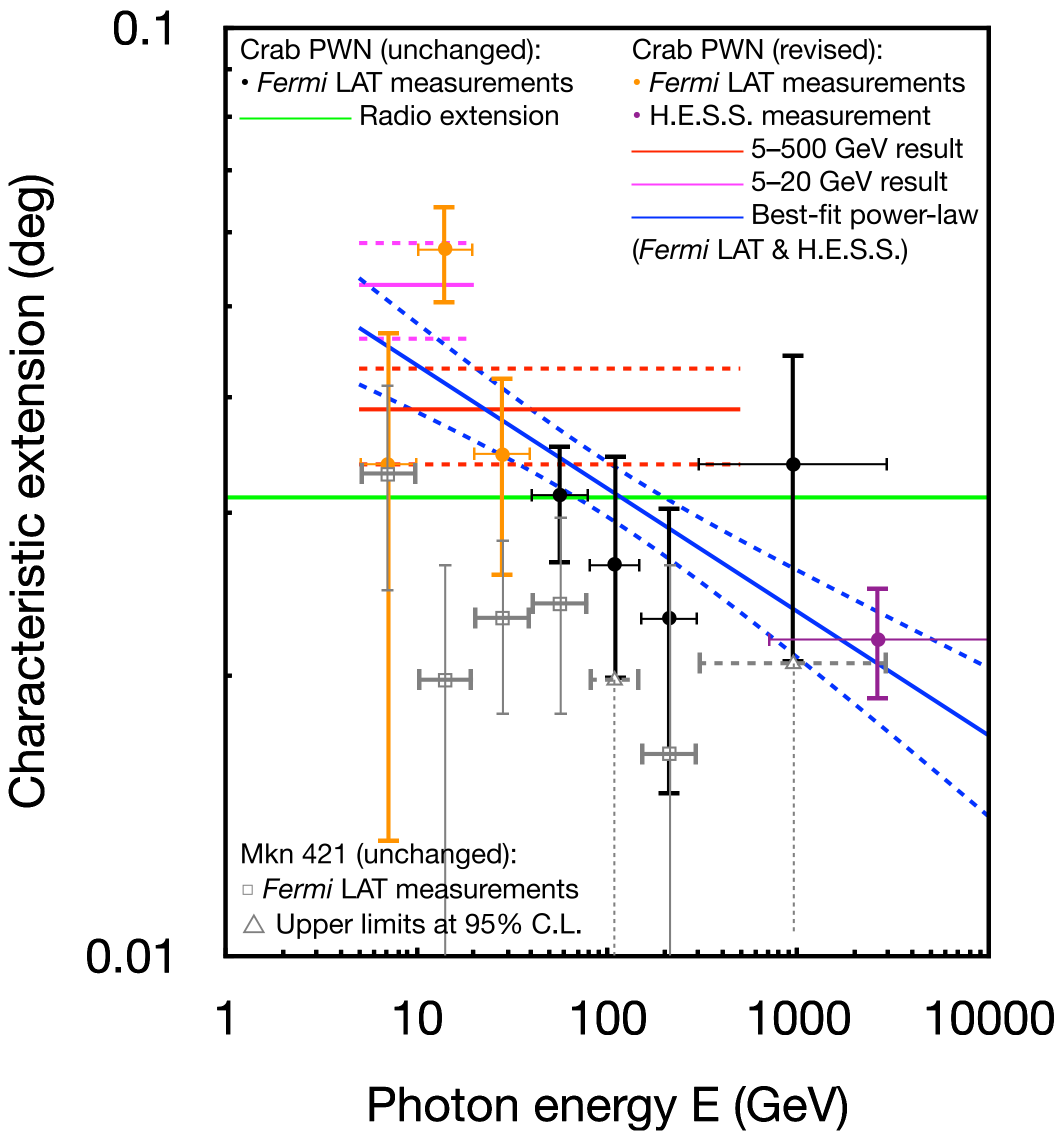

Figure 1. Spectral distribution of characteristic extensions (defined as the 68% containment radius R_{68}; either the uniform-disk radius multiplied by $\sqrt{0.68}$ or the Gaussian rms width multiplied by $\sqrt{2ln(1/0.32)}$) of the Crab PWN (modified from Figure 6 of our original paper). The orange bins are our revised LAT results in this erratum, and the black bins are the LAT results taken from our original article. The H.E.S.S. bin (purple) is revised to be the result of H. E. S. S. Collaboration (2020), where the best-fit value remains the same as before but the uncertainty becomes smaller. The revised R_{68} of the energy-independent disk morphologies fit to the 5–500 and 5–20 GeV datasets are plotted in red and magenta respectively. The blue line is revised to be the power-law fit to all orange, black and purple bins of this modified figure: $R_{68} = (0.0317 \pm 0.0022)(\frac{E}{103.8\ \mathrm{GeV}})^{-0.133\pm0.037}$ deg, where the prefactor and index are decorrelated.

Chapter 4

The Fast-dimming Property of the Synchrotron Nebula

In this chapter, we investigate the γ-ray variability of the synchrotron nebula in detail, with the 60 MeV–10 GeV LAT data accumulated from 2008 August 4 to 2018 August 20 during the off-pulse phase of the Crab pulsar. Besides the flaring periods, we consider the whole light-curve. Contents of this sub-topic have been published in Yeung and Horns (2020), whose publisher version is presented below *(Credit: Paul K. H. Yeung & Dieter Horns, Astronomy & Astrophysics, 638, A147 (2020), reproduced with permission © European Southern Observatory).* The work presented in Section 3.1 of this publication is also a part of our project proposal which is associated with our research grant HO 3305/4-1 from the DFG.

My contributions to this publication. By using the *Fermi* Science Tools v11r5p3 package introduced in Chapter 2, I performed reductions and analyses on Fermi LAT data, with refinements suggested by my supervisor Prof. Dr. Dieter Horns. In phase-resolved analyses in Sections 3.1, 3.2, 3.3 and 3.6, I adopt the timing solution of the Crab pulsar provided by Dr. Matthew Kerr (documented in Appendix A). The initial ideas of Sections 3.3, 3.4, 3.5 and 3.6 (as well as the relevant figures and tables) are created by my supervisor and are implemented by me under his guidance. The program code for Section 3.4, mainly developed by my supervisor Prof. Dr. Dieter Horns and then further modified by me, and our respective contributions are documented in Appendix B.1. I implemented the Bayesian block segmentations (Scargle et al., 2013) in Sections 3.4 and 3.5, with the "astropy.stats.bayesian_blocks" [1]. I implemented the light-curve simulations in Section 3.5, with the "DELightcurveSimulation" package [2]

[1] bayesian_blocks – Astropy v4.0.2: https://docs.astropy.org/en/stable/api/astropy.stats.bayesian_blocks.html

[2] Code in GitHub: https://github.com/samconnolly/DELightcurveSimulation

(Connolly, 2015) whose development is based on the recipe of Emmanoulopoulos et al. (2013). The ideas of interpretations in Section 4.2 are mainly created and written by my supervisor, while I performed some relevant calculations to confirm that he interpreted my results reasonably. The other parts of the manuscript are written mainly by myself. I made all figures and tables with comments from my supervisor on the formats.

Supplementary information to Section 3.6 of this publication is presented in Appendix C.3. In addition to the contents of this publication, I found that the synchrotron flux of the Crab Nebula varies at a broad range of timescales and we have no strong evidence for existence of a steady baseline state (see Appendix C.2).

Thanks to the responsible editor, this publication is included in A&A highlights [3].

[3] A highlight on our Yeung and Horns (2020) written by the editor: https://www.aanda.org/2020-highlights/1854

A&A 638, A147 (2020)
https://doi.org/10.1051/0004-6361/201936740

Astronomy & Astrophysics

Fermi Large Area Telescope observations of the fast-dimming Crab Nebula in 60–600 MeV

Paul K. H. Yeung and Dieter Horns

Institute for Experimental Physics, Universität Hamburg, Luruper Chaussee 149, 22761 Hamburg, Germany
e-mail: kin.hang.yeung@desy.de

Received 19 September 2019 / Accepted 5 May 2020

ABSTRACT

Context. The Crab pulsar and its nebula are the origin of relativistic electrons which can be observed through their synchrotron and inverse Compton emission. The transition between synchrotron-dominated and inverse-Compton-dominated emissions takes place at $\approx 10^9$ eV.

Aims. The short-term (lasting for one week to months) flux variability of the synchrotron emission from the most energetic electrons is investigated with data from ten years of observations with the *Fermi* Large Area Telescope in the energy range from 60 MeV to 600 MeV.

Methods. We reconstructed the off-pulse light curve reconstructed from phase-resolved data. The corresponding histogram of flux measurements was used to identify distributions of flux-states and the statistical significance of a lower-flux component was estimated with dedicated simulations of mock light curves. The energy spectra for different flux states were also reconstructed.

Results. We confirm the presence of flaring-states which follow a log-normal flux distribution. Additionally, we discovered a low-flux state where the flux drops to as low as 18.4% of the intermediate-state average flux and remains there for several weeks. The transition time is observed to be as short as two days. The energy spectrum during the low-flux state resembles the extrapolation of the inverse-Compton spectrum measured at energies beyond several GeV energy, implying that the high-energy part of the synchrotron emission is dramatically depressed.

Conclusions. The low-flux state found here and the transition time of at most ten days indicate that the bulk (>75%) of the synchrotron emission above 10^8 eV originates in a compact volume with apparent angular size of $\theta \approx 0.''4\ t_{\rm var}/(5\ {\rm d})$. We tentatively infer that the so-called inner knot feature is the origin of the bulk of the γ-ray emission.

Key words. ISM: individual objects: Crab Nebula – gamma rays: ISM

1. Introduction

Isolated neutron stars and their environments are powerful sites of particle acceleration, which result in the formation of pulsar wind nebula (PWN) systems. In the case of the Crab Nebula, the extended cloud of non-thermal plasma is radiating in multi-wavelength, from radio to gamma-ray (Aharonian 2004; Bühler & Blandford 2014; Dubner et al. 2017).

The Crab Nebula is a PWN powered by a ~1 kyr old pulsar (Hester 2008). It is a part of the core-collapse supernova remnant located in the constellation of Taurus and at a distance of 2 kpc (Trimble 1968). Due to the exceptionally wide observable energy range, we can study the processes of particle acceleration that are presumably happening at the termination shock and witness energy losses in the nebula (e.g., Spitkovsky & Arons 2004; Fraschetti & Pohl 2017).

The observed hard γ-ray (1 GeV–80 TeV) spectrum of the Crab Nebula has been compared with various model calculations which use widely different approaches (de Jager & Harding 1992; Atoyan & Aharonian 1996; Hillas et al. 1998; Volpi et al. 2008; Meyer et al. 2010; Martín et al. 2012). All these models assume that the gamma-ray emission in this energy range is predominantly produced via inverse-Compton (IC) scattering of relativistic electrons with synchrotron-radiated photons, as initially suggested by Rees (1971) and Gunn & Ostriker (1971).

Meanwhile, at lower energies, the observed nebular γ-ray (0.75 MeV–1 GeV) spectrum is presumably dominated by the synchrotron mechanism (Kuiper et al. 2001; Buehler et al. 2012). The Crab Nebula experiences recurrent flares (roughly one per year) detected with AGILE and *Fermi* Large Area Telescope (LAT), some of which boosted up the >100 MeV synchrotron flux by a factor of $\gtrsim$20 (e.g., Tavani et al. 2011; Abdo et al. 2011; Buehler et al. 2012; Mayer et al. 2013). Enhanced γ-ray emission of the synchrotron component can last for a broad variety of timescales ranging from days to weeks (Striani et al. 2013). Ongoing instability of the synchrotron emission from the Crab Nebula is also observed in the hard X-ray/soft γ-ray regime over a longer range of time (Ling & Wheaton 2003; Wilson-Hodge et al. 2011).

In this work, we study the γ-ray variability of the Crab Nebula in detail, with the >60 MeV LAT data accumulated over about ten years during the off-pulse phase of the Crab pulsar. In addition to the flaring periods, we consider the entire light curve.

2. Data reduction and analysis

We performed a series of binned maximum-likelihood analyses (with an angular bin size of 0.1°) for a region of interest (ROI) of 30° × 30° centered at RA = $05^{\rm h}34^{\rm m}31.94^{\rm s}$, Dec = +22°00′52.2″ (J2000), which is approximately the center of the Crab Nebula (Lobanov et al. 2011). We use the data of 60 MeV–10 GeV photon energies, registered with the LAT between 2008 August 4

A&A 638, A147 (2020)

Table 1. Time-averaged spectral properties of the Crab Nebula measured from 60 MeV to 10 GeV.

Component	PL Γ	PLEC Γ	PLEC E_c (GeV)	$TS_{PLEC} - TS_{PL}$ [(a)]	Integrated flux [(b)] (10^{-9} cm^{-2} s^{-1})
IC	1.415 ± 0.023	...	...	...	107 ± 5
Synchrotron	3.278 ± 0.011	3.250 ± 0.026	6.6 ± 5.7	1.7	2534 ± 15

Notes. [(a)]Γ is the photon index. E_c is the energy of the exponential cutoff. $TS_{PLEC} - TS_{PL}$ is the difference in test-statistic (TS) between PLEC and PL. [(b)]The integral fluxes are based on PL models.

and 2018 August 20. The data were reduced and analyzed with the aid of the *Fermi* Science Tools v11r5p3 package.

Considering that the Crab Nebula is quite close to the Galactic plane (with a Galactic latitude of −5.7844°), we adopt the events classified as Pass8 "Clean" class for the analysis so as to better suppress the background. The corresponding instrument response function (IRF) "P8R2_CLEAN_V6" is used throughout the investigation. Only the data collected during the off-pulse phase (0.56–0.88; adopting the same convention of phase as in Buehler et al. 2012) of the Crab pulsar are selected for analysis. Correspondingly, a correction factor of 1/0.32 is taken into account in calculations of phase-averaged fluxes. We further filter the data by accepting only the good time intervals where the ROI was observed at a zenith angle less than 90° so as to reduce the contamination from the albedo of Earth.

In order to account for the contribution of diffuse background emission, we include the Galactic background (gll_iem_v06.fits), the isotropic background (iso_P8R2_CLEAN_V6_v06.txt), as well as all other point sources cataloged in the LAT 8-year Point Source Catalog (4FGL; The Fermi-LAT Collaboration 2019) within 32° from the ROI center in the source model. We set free the spectral parameters of the sources within 10° from the ROI center (including the prefactor and index of the Galactic diffuse background as well as the normalization of the isotropic background) in the analysis. For the sources at angular separation beyond 10° from the ROI center, their spectral parameters are fixed to the catalog values.

The three point sources located within the nebula are cataloged as 4FGL J0534.5+2200, 4FGL J0534.5+2201i, and 4FGL J0534.5+2201s, which respectively model the Crab pulsar, the IC, and synchrotron components of the Crab Nebula. We remove 4FGL J0534.5+2200 from the source model because the on-pulse data has been screened out. In broadband spectral analyses, we enable the energy dispersion correction which operates on the count spectra of most sources including the Crab Nebula, following the recommendations of the *Fermi* Science Support Center.

3. Spectral properties and variability of the Crab Nebula

3.1. Time-averaged spectrum

The energy spectrum of the off-pulse nebular component at energies between 60 MeV and 10 GeV is reconstructed using the combined observational data of approximately ten years (see previous section for an overview of the data reduction steps including the pulsar gating).

The data are fit by a two-component (additive) model. Similar to a previous study (Buehler et al. 2012), we use the superposition of a soft power law (PL) with a photon index constrained to the interval 3–5 for the synchrotron component and a hard PL with a photon index constrained within 0–2 for the IC component of the nebular emission. It is known that the spectrum of the IC component at energies beyond 10 GeV requires a more complex model. However, within our fitting range up to 10 GeV, two PL models are sufficient to characterize the broad-band spectrum (see Table 1 for the resulting parameters). More complex models including a "power law with exponential cutoff" (PLEC) for the synchrotron component are not significantly preferred, as a likelihood ratio test indicates that the improvement is not significant (∼1.3σ). It is comforting to see that the sum of these two components (thereafter "Syn+IC"), extrapolated to the >100 MeV band, agrees within 20% with that computed from the model of Buehler et al. (2012).

For the purpose of evaluation, we repeated the fit with disabled energy dispersion correction. It turns out that the measured photon index of the synchrotron component becomes steeper by ∼0.07, while the difference in the synchrotron photon flux is measured to be only ∼1%. This indicates that despite the migration of photon energies, the integrated photon flux in a broad band is approximately conserved.

Then, we divide the entire energy band into 13 discrete energy bins (six bins per decade from 60 MeV to 6 GeV, and a bin between 6 GeV and 10 GeV). In the spectral fitting for each bin, we use a single PL component to model the total Syn+IC emission from the Crab Nebula so as to avoid degeneracies. Both the photon index and flux normalization are left free in this procedure. The measured differential fluxes multiplied by the squared geometrical average energy of each bin and the corresponding 1σ uncertainties, as well as the broadband spectral model, are plotted in Fig. 1. The relative systematic uncertainty of the differential flux stemming from disabling the correction for energy dispersion is estimated to be (6–12)% in 60–600 MeV and (3–6)% in 600 MeV–10 GeV (see[1] Pass 8 Analysis and Energy Dispersion).

3.2. Long-term light curve

In order to explore the time-variability of the synchrotron flux, we generated a light curve for the 60 MeV–600 MeV band. In this energy range, we estimate that the IC component only accounts for <8% of the integrated average flux. It is therefore justified to use a single PL as the model of the total Syn+IC emission for energies between 60 MeV and 600 MeV. Prior to temporal analyses, we performed an analysis for this energy band with the complete ten-year data set. The flux normalization of the isotropic diffuse model is found to be ≈1.13 (scaled to the full phase), and the PL spectral index for energy-dependent scaling of the Galactic diffuse model is found to be ≈0.018. Since these two parameters are not expected to noticeably change within ten years, in analyses for individual temporal segments, we fix them

[1] https://fermi.gsfc.nasa.gov/ssc/data/analysis/documentation/Pass8_edisp_usage.html

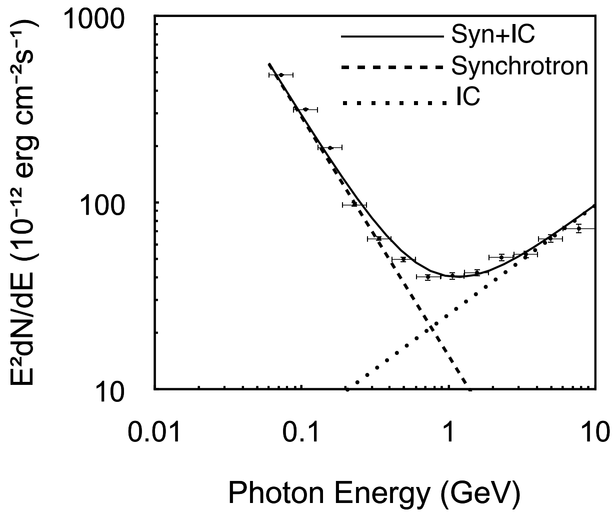

Fig. 1. Time-averaged spectral energy distributions (SED) of the Crab Nebula. The solid line and the binned spectrum represent the total Syn+IC emission, while the dashed and dotted lines represent the synchrotron and IC components respectively.

at the ten-year averages, while the prefactor of the Galactic diffuse model is still left free.

For the binning of the light curve we choose a time interval of five days which strikes a compromise between time-resolution and statistical uncertainties. The average photon detection rate from the Crab Nebula during the off-pulse interval chosen here is approximately 100 photons per day. In general, the statistical uncertainties of fluxes are conspicuously greater than the photon shot-noise, reflecting a small signal-to-noise ratio. For those time intervals with insufficient photon statistics ($\lesssim$4 photons per day), we also place upper limits of a 95% confidence level on the nebular flux. The resulting light curve is shown in Fig. 2.

The analysis confirms the finding of previous studies that the Crab Nebula experiences a series of flares, including those reported by Buehler et al. (2012), Mayer et al. (2013), Striani et al. (2013), ATELs #8519 (Jan.-2016, around MJD 57400) and #9586 (Oct-2016, around MJD 57700). The light curve is however not well-characterized by a constant flux state superimposed by flaring activity with a small duty-cycle, resembling flicker noise. For the first time, we find that the flux occasionally drops well-below the average flux value.

This impression is confirmed when investigating the light curve in the frequency domain. The periodogram (Fig. 3) is determined via a discrete Fourier-transformation (DFT) of the real-valued light curve normalized to the average flux. The power-spectral density (PSD) is calculated from the complex valued coefficients of the DFT. The resulting PSD is characterized by a smooth PL such that $\mathrm{PSD}(f) = (0.18 \pm 0.08) \times (f/d^{-1})^{-0.73\pm0.12}$.

The histogram of the flux measurements (Fig. 4) can be described by the superposition of two log-normal distributions (see Table 2 for the best-fit paramaters). The component A represents the extrapolated IC flux fluctuating below and around the detection threshold, with a relative normalization left free to vary in a Poissonian log-likelihood fit of the histogram. The component B characterises the variable synchrotron emission. This model is preferred over a single log-normal distribution by $\sim$13σ, indicating the presence of at least two different flux states. Based upon this two-component model, we set the threshold of the "low" state at 4.8×10^{-7} cm^{-2} s^{-1}, so that the extrapolated tail of the component B below this threshold predicts only less than one-fourth of the observed low-state bins to be contaminated by the component B. The threshold of the "high" state is set at 5.7×10^{-6} cm^{-2} s^{-1} so that only the top 23 bins are included in the high state. In Sect. 3.5, by using simulated light curves, we confirm that a two-component model is necessary and sufficient for reproducing the continuous low-flux episodes observed (Fig. 5).

After introducing a third log-normal component, the fitting is further improved by $>6\sigma$. The component X represents the extrapolated IC flux and it accounts for the bottom (3.3 ± 1.0)% of measurements. This corresponds to an expected 23 ± 7 out of the 68 observed low-state bins. The strongly variable component Y spans from the low flux state to the highest flux state. The component Z is mostly confined within intermediate flux states. In Sect. 3.6, we infer the relative contributions of the synchrotron nebula and IC nebula during the low state, based on spectral analyses.

We proceeded to perform an analysis with 60–600 MeV data excluding the high- and low-state bins we defined. In this way, the intermediate-state average flux is determined to be $(2.61 \pm 0.02_{\mathrm{stat}} \pm 0.20_{\mathrm{sys}}) \times 10^{-6}$ cm^{-2} s^{-1}, where the systematic uncertainty is determined by altering the prefactor of the Galactic diffuse model by ±10%. The statistical uncertainty in a five-day interval is generally more than a double of this systematic uncertainty. The low-state threshold we set is 18.4% of this intermediate-state average flux.

3.3. Systematic effects on the variability

The instrument, its calibration, and data analysis contribute various systematic effects that may lead to variability in excess of the limiting photon shot-noise. Similar to the approach presented by Ackermann et al. (2012), we use a data-driven method to investigate systematic effects and the stability of the light curve. Fortunately, we can use the Crab pulsar itself to establish an estimate of the instrumental variability.

We selected data collected during the phase around the highest pulse peak (0–0.02, and 0.97–1; recall that the phase convention in Buehler et al. 2012 is adopted). Then, from the total Crab flux of each bin, we subtract the nebular flux which is measured at the same bin and scaled to match the phase interval covering 5% of the total phase. The resulting light curve for the pulsar emission is based on a photon count statistics that matches the off-pulse light curve, making it suitable to be used as a control light curve.

This control light curve displays a fractional root-mean-square (RMS) variability of 14% with a PSD that is close to white noise. The resulting PSD can be readily compared with the one measured from the off-pulse emission (see Fig. 3) with a fractional RMS variability of 76%. The control light curve shows some excess noise when compared with the expected fractional variability for shot-noise only which should be $\approx N_{\mathrm{phot}}^{-1/2} \approx 4.5\%$ with the number of photons expected in a five-day interval ($N_{\mathrm{phot}} \approx 500$). We conservatively consider the noise in the control light curve as an estimate of the instrumental and photon shot noise present in the data.

The fractional RMS variability of 76% displayed in the off-pulse light curve has a significant portion accounted for by flaring bins. Even if we exclude all bins which are above the intermediate-state average, the fractional RMS variability still remains at a high value of 50%. This is a strong indication that

A&A 638, A147 (2020)

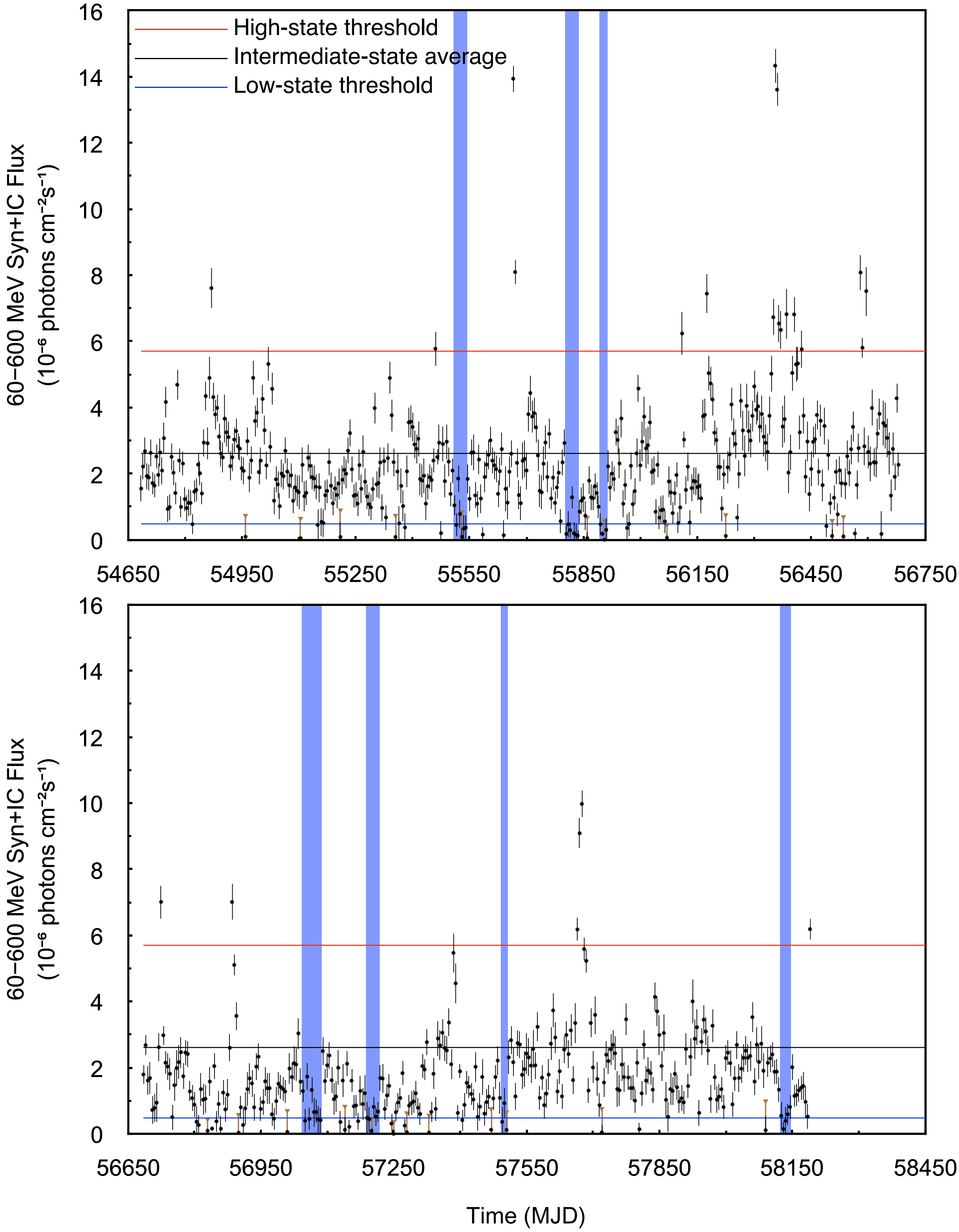

Fig. 2. Long-term light curve of the Crab Nebula (the total Syn+IC emission) for the 60 MeV–600 MeV band. The size of each bin is five days. The flux measurements of all bins are plotted as black circles with statistical uncertainties, while the upper limits of a 95% confidence level (only for the bins with insufficient photon statistics) are plotted as brown triangles. The black horizontal line indicates the intermediate-state average flux, while the red and blue lines respectively indicate the thresholds of the "high" and "low" states we define (see the text for detail). Blue vertical bands indicate continuous (≥15 d) "dip" features which are reported in Table 3.

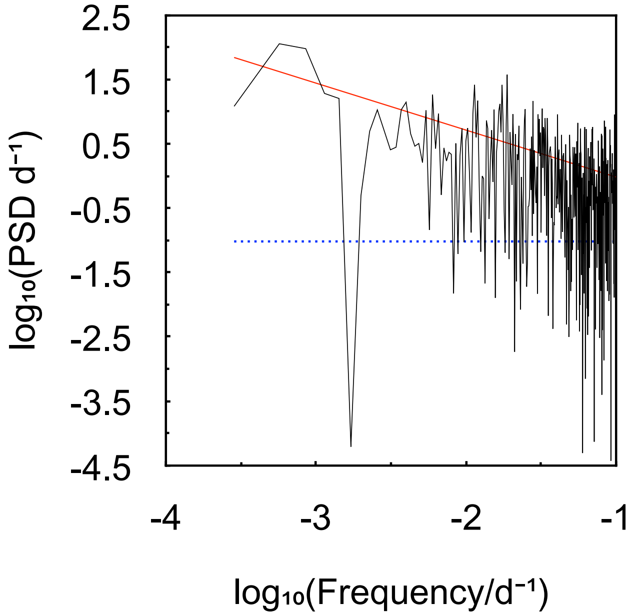

Fig. 3. Periodogram obtained from the long-term light curve of the Crab Nebula. The PSD is normalized to fractional variance per frequency unit. The red-solid curves in the periodogram respectively indicate the best-fit PL (whose index is 0.73 ± 0.12). The blue-dotted line indicates the white-noise PSD of a control light curve.

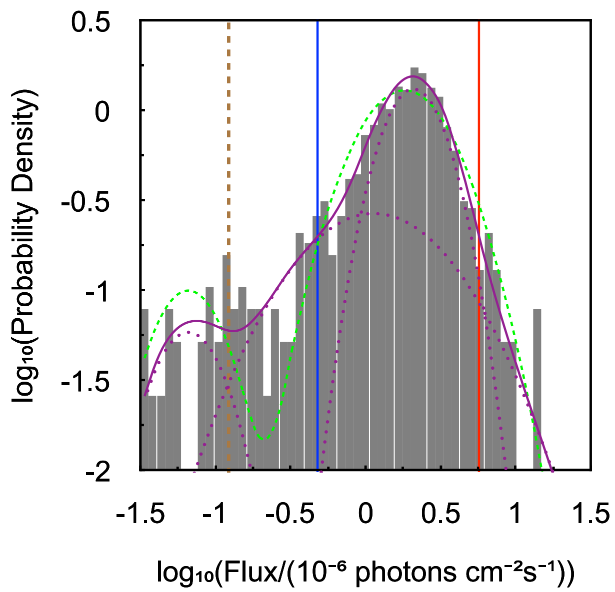

Fig. 4. Probability density function (PDF) obtained from the long-term light curve of the Crab Nebula. The histogram is normalised in a way such that the integration of the probability density over the $\log_{10}$(Flux) is 1. The double and triple log-normal models fit to the PDF are overlaid as green-dashed and purple-solid curves respectively. Their lowest-flux components model the shot-noise limited distribution of the extrapolated IC flux. The three components of the triple log-normal model are overlaid as purple-dotted curves. The blue and red vertical lines indicate the threshold of the "low" and "high" states respectively. The brown-dashed vertical line indicates the flux sensitivity corresponding to a detection significance of $\sim 3\sigma$ and a photon count of ~20 in a five-day interval.

the flux variations in the nebular light curve exceed the combined systematic and shot noise estimated from the control light curve at all frequencies (see also Fig. 3).

A limitation of the control light curve is that the 60 MeV–600 MeV spectrum of the Crab pulsar is harder than that of the nebula (Buehler et al. 2012). Any energy-dependent systematic uncertainties of *Fermi* LAT would, therefore, have different impacts on the nebular and pulsar light curves. As an additional check, we compute the exposure within 1° from the Crab for each five-day bin of the light curve, assuming a photon index of 3.3. Based upon this study, we have no evidence that the variability is related to fluctuations in the exposure.

Transient effects due to the relative position of the Sun or the Moon to the Crab Nebula could affect the light curve. An excess of the solar or lunar γ-ray emission could lead to an apparent deficit in the computed Crab flux. After checking the history of the Sun's position, we do not see a causality between the observed "dip" features and solar encounters or approaches. The lunar encounters or approaches should be comparatively less of an issue, because the γ-ray emission from the Moon is much less extended (its radius of γ-ray extension is only $\lesssim 0.5°$) and the Moon remains closer than seven degrees to the Crab Nebula for only <1 day (shorter than one-fifth of the bin size) in every sidereal period of 27.3 days. The periodogram of the nebular light curve reveals no distinct modulation at the lunar sidereal period or its harmonics.

Furthermore, the impact of the migration of photon energies on the nebular light curve leads to additional systematic effects. While disabling the energy dispersion correction leads to noticeable mis-measurements in the photon index, the integrated photon flux in a decade of energy range is expected to remain constant. The resulting estimated relative systematic uncertainty on the photon flux (~1% of the flux, as evaluated in Sect. 3.1) is not important when compared to the dominating statistical uncertainty in a five-day interval.

3.4. Transitions between low-flux and intermediate states

We identified seven episodes of continuous low-flux where the 60 MeV–600 MeV Syn+IC flux remains as low as 18.4% of the intermediate-state average for at least half a month. We applied the Bayesian block algorithm (Scargle et al. 2013) on the seven analysis windows covering these episodes (Fig. 5) to identify different flux states. In turn, we quantified the transitional timescales between them by fitting composite functions to individual five-day bins in segments of the light curve.

We report the time range covered by the lowest one or two successive blocks of each window as a low-flux episode. The fit range we chose for each window includes the low-flux episode as well as its preceding and following blocks. The function we fit starts and ends with two constant fluxes which are respectively equal to the local averages within the preceding and following blocks of a low-flux episode. The free parameters of the fit include the starting and stopping times of the low-flux episode where the flux varies as a sum of an exponential decay term and an exponential growth term. The predicted flux must be continuous in the whole fit range. There are in total four free parameters in the fit: in addition to the starting and stopping times, we estimate the halving time of the decay term as well as the doubling time of the growth term.

The best segmentations with a false positive rate of 0.07, as well as the functions fit to segments of the light curve, are overlaid in Fig. 5. The information about the seven episodes and the timescales of transitions are tabulated in Table 3. As a cross-check, we repeat the fits with two additional free parameters: the constant flux before decay and that after growth. We obtain

A&A 638, A147 (2020)

Table 2. PDF models fit to the histogram of the flux measurements.

Model	Component	N_0 [(a)] (%)	$F_{\rm maxPD}$ [(b)] (10^{-6} cm^{-2} s^{-1})	$\sigma_{\rm lnF}$ [(c)]	ΔTS [(d)]	Δdof [(e)]
Single log-normal	...	100	1.56 ± 0.06	0.94 ± 0.03	0	0
Double log-normal	A [(f)]	5.6 ± 1.0	0.066 (fixed)	0.51 (fixed)	180.4	1
	B	94.4 ± 1.0	1.82 ± 0.05	0.67 ± 0.02		
Triple log-normal	X [(f)]	3.3 ± 1.0	0.066 (fixed)	0.51 (fixed)	233.6	4
	Y	31.2 ± 13.0	1.14 ± 0.33	1.07 ± 0.18		
	Z	65.5 ± 13.9	2.10 ± 0.08	0.45 ± 0.06		

Notes. [(a)]The normalization for scaling a component. In each model, the sum of normalizations of all components must be 1. [(b)]The flux corresponding to the maximum probability density. It is mathematically equivalent to the exponential of the mean of the flux's natural logarithm. [(c)]The standard deviation of the flux's natural logarithm. [(d)]The natural logarithm of the square of the likelihood ratio of a model compared to the single log-normal. The likelihood function is for a Poisson distribution. [(e)]The number of additional parameters (the extra degrees of freedom) of a model compared to the single log-normal. [(f)]Components which model the shot-noise fluctuations of the extrapolated IC flux. All of their parameters except normalizations are fixed at values estimated from the photon statistics.

consistent results. The fit results constrain the shortest timescales of transitions between low-flux and intermediate states to be <1.9 days (95% c.l.).

3.5. Comparison of the observed light curve to simulated light curves

The nebular emission is characterized by a red-noise PSD, dominating above instrumental noise at all frequencies sampled. In the time-domain, we have identified episodes where the flux of the nebula drops well below the average and remains low for several weeks. In order to clarify to what extent these kind of episodes occur randomly, we simulate 10^6 light curves following the recipe of Emmanoulopoulos et al. (2013) which has been implemented in the "DELightcurveSimulation" package (Connolly 2015). The method extends on the original approach (Tam & Yang 2012), where a method to simulate light curves with Gaussian distributed flux states and a power-law PSD is introduced. In the method used here, an arbitrarily shaped probability density function (PDF) for the flux state can be used.

The bulk of observed flux states follows a log-normal distribution. However, a noticeable deviation at lower flux states is apparent (see Fig. 4). We simulated, therefore, a log-normal PDF (with the same mean and standard deviation as the component B in Table 2) in combination with the power-law PSD (Fig. 3). In absence of a low state, we can use the simulated light curves to estimate the probability of appearance of similar episodes of low-flux as observed in the data.

We applied the Bayesian block algorithm (Scargle et al. 2013) on our observed light curve and each simulated light curve, with a false positive rate of 0.07. Then, we search for the continuous "dip" feature, which is defined as a block or a set of successive blocks fulfilling two conditions (mimicking the phenomena shown in Fig. 5): (a) the total length is at least three bins (15 days), and (b) the local mean (error-weighted) of each included block is below 4.8×10^{-7} cm^{-2} s^{-1} (the blue line in Figs. 2 and 5). Such a dip feature appears in our observed light curve for a total of seven times.

Among the simulated light curves based on the log-normal PDF, only a fraction of 5.4×10^{-5} have at least seven dips. In other words, the expected number of dips in a simulated light curve is less than that in our observed light curve at a $>3.8\sigma$ level.

In order to verify that a PDF with a second, low-flux component is a closer match to the observed features in the light curve, we simulate again 10^6 light curves using a double log-normal distribution (Table 2) in combination with the same PSD. For this PDF, the average number of dips in a simulated light curve is 6.0 ± 1.9, which is consistent with our observations.

Repeating two chains of simulations with a more complex PSD (curved and with a constant additive term), we obtain very similar results, verifying that the exact shape of the model for the PSD is not of importance. While a double log-normal PDF is sufficient for a simulation to reproduce the seven continuous dip features we observe, we recall that the whole histogram of flux measurements suggests a more complicated distribution of flux states (see Fig. 4 and Table 2).

3.6. Spectra in different flux states

The result of the temporal analysis suggests the existence of a low-flux state (see Sects. 3.2 and 3.5). In order to investigate the spectral changes of the nebula during the defined "high" and "low" states respectively, we sort the 702 bins of the light curve according to the best-fit photon flux. The thresholds of these two flux states have been shown in Figs. 2 and 4. We group the top 23 bins above the red line into the high flux state data. For the low state, we select the lowest 68 bins below the blue line. Their accumulated TS is sufficient for us to create a binned spectrum with well-constrained uncertainties. We repeat the chain of spectral fittings described in Sect. 3.1 for the high and low states. The results are plotted in red and blue, respectively, in Fig. 6. The fit parameters are tabulated in Table 4.

In both states, the binned spectra indicate that the differential flux at any energy between 1.9 GeV and 10 GeV remains consistent with the ten-year average, within the tolerance of 1.5σ uncertainties. Therefore, we fix the parameters of the IC component at the values determined with the whole ten-year data set.

During the high state, the PL index of the synchrotron component is harder than that of the ten-year average spectrum by $\sim 24\sigma$, and PLEC is preferred over PL by $\sim 10.7\sigma$, confirming previous results on the flaring state of the Crab Nebula (Buehler et al. 2012; Mayer et al. 2013). The differential low-state spectrum (shown in Fig. 6 in blue) differs from the average spectrum too. During the low state, the energy spectrum of the synchrotron component cannot be well described by PL or PLEC with physically reasonable parameters, so we just report the synchrotron flux computed directly from the binned spectrum, which is (15 ± 5)% of the ten-year average.

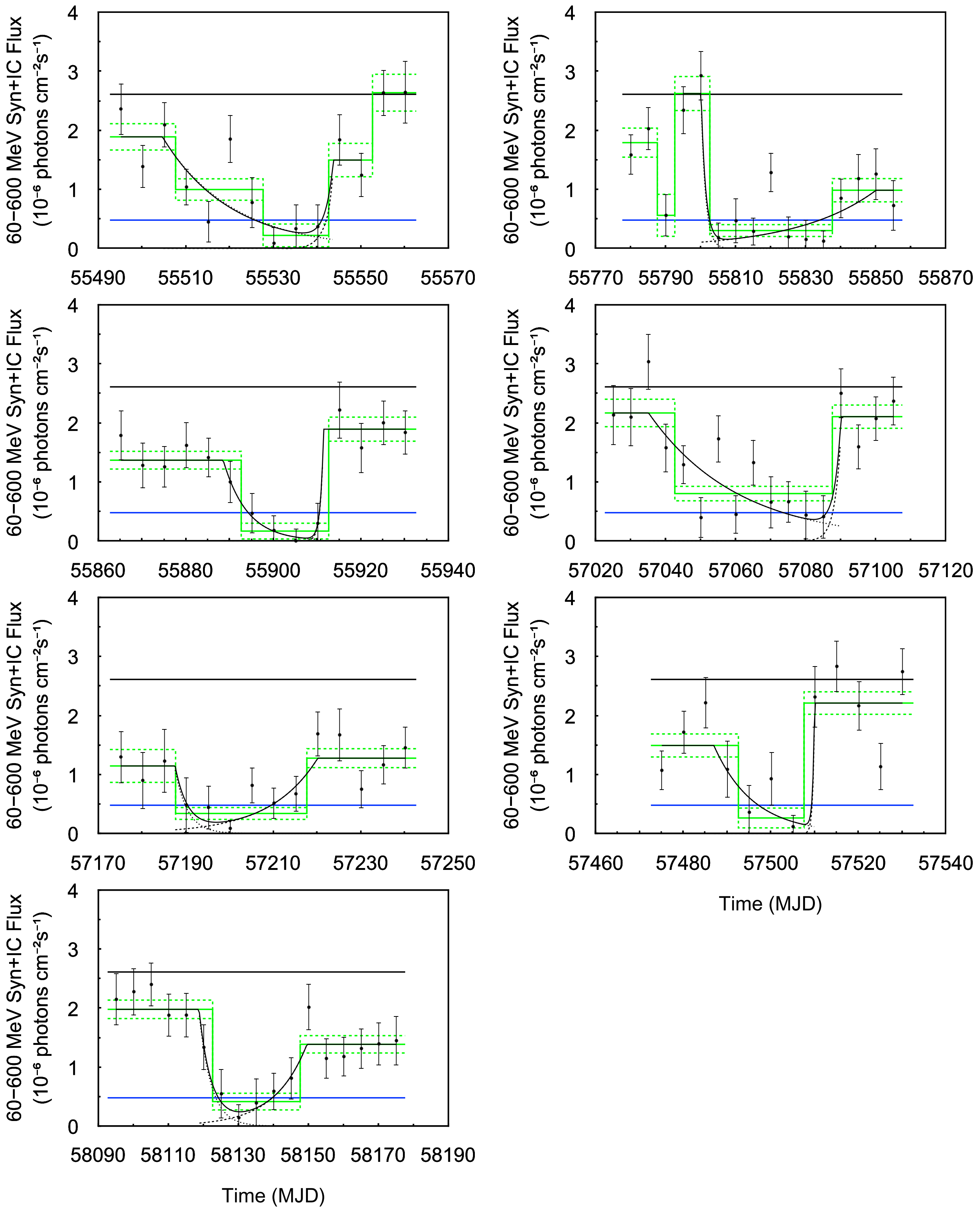

Fig. 5. Seven analysis windows covering continuous episodes of low-flux which are tabulated in Table 3. The uniform distribution fit to the bins of each Bayesian block (solid line) and its 1σ uncertainty (dashed line) are indicated in green. The function fit to each segment of the light curve, as well as its two exponential terms, is plotted as black curves (see the text for detail). The black and blue horizontal lines respectively indicate the intermediate-state average flux and the threshold of the "low" state we define.

Table 3. Information about seven episodes of continuous low-flux.

Start time (MJD)	Duration [(a)] (days)	$F_{\rm low}$ [(b)] ($10^{-6}\,{\rm cm}^{-2}\,{\rm s}^{-1}$)	$t_{1/2}$ [(c)] (days)	t_2 [(d)] (days)
55507.7	35	0.70 ± 0.14	$10.7^{+4.7}_{-2.8}$	<5.3
55802.7	35	0.38 ± 0.11	<2.2	$15.5^{+31.6}_{-6.1}$
55892.7	20	0.24 ± 0.15	$3.8^{+2.9}_{-1.9}$	<3.3
57042.7	45	0.82 ± 0.12	$17.7^{+4.5}_{-3.3}$	<4.0
57187.7	30	0.50 ± 0.13	<12.6	$7.5^{+2.2}_{-3.1}$
57492.7	15	0.47 ± 0.22	$6.2^{+2.6}_{-2.3}$	<1.9
58122.7	25	0.50 ± 0.16	$2.4^{+2.6}_{-1.1}$	$6.4^{+3.4}_{-2.9}$

Notes. [(a)]The start times and durations are determined from Bayesian block segmentations. [(b)]The local average fluxes in 60 MeV–600 MeV within the durations. In view of a broad variety of uncertainties, we adopt the unweighted means (instead of the error-weighted means plotted in Fig. 5) for unbiased calculations. [(c)]Halving times of the exponential decay term. The upper limits are at a 95% confidence level. [(d)]Doubling times of the exponential growth term. The upper limits are at a 95% confidence level.

On the other hand, the entire Syn+IC spectrum during the low state can be fit by a single PL component, despite a potential excess in the lowest energy bin ($\sim 2.5\sigma$). Such an outlying bin is measured with 60–129 MeV data, which is limited by particularly poor spatial and spectral resolutions of LAT as well as the severe inaccuracy on the part of diffuse models. This PL has a hard index (1.65 ± 0.05) and a low integral flux which are quite comparable to those of the ten-year average IC component. The γ-ray luminosity of the IC component is 77% of the low-state luminosity of the whole Crab Nebula computed from this model.

We note that 22 out of the 68 low-state bins have their preceding and following bins both ≥44% of the intermediate-state average. They can be considered "isolated" (i.e., not in pairs or clusters). On average, a mock light curve simulated with the log-normal PDF and the power-law PSD (reported in Sect. 3.5) has 16.2 ± 4.0 low-state bins where 2.0 ± 1.7 of them are isolated in the same way. We recall that the combined systematic and shot noise has a fractional RMS variability of ~14% (as evaluated in Sect. 3.3). Also, immediately before and after a low-flux bin, the Crab Nebula is probably in a similar physical state for a while. These entail a statement that some isolated low-state bins in the observed nebular light curve could be occasional chance events. Therefore, the numerous discontinuities in our selection of low-state bins could have introduced non-negligible systematic bias in measuring the low-state spectral properties.

With regards to this issue, we reconstructed an alternative low-state spectrum as a cross-check. In order to investigate the spectrum for clusters of low-flux bins, we grouped a total of 41 bins of the seven continuous low-flux episodes (Table 3) into this alternative low-state, and the obtained result is overlaid in Fig. 6 as well. It turns out that the two low-state spectra have very similar integrated fluxes and photon indices.

4. Summary and conclusion

4.1. Summary of main results

Variability and low-flux state of the synchrotron nebula The long-term light curve of the gamma-ray emission from the Crab Nebula in the energy range between 60 MeV and 600 MeV has been extracted from ten years of observation with the *Fermi* LAT instrument. On average, >92% of the integrated flux is accounted for by synchrotron radiation. The light curve shows pronounced variability, with a relative standard deviation equal to 76%. As demonstrated with a control light curve from a phase-gated part of the pulsar emission, we estimate that less than 2% of the measured variability could be related to instrumental or systematic effects. The periodogram follows a PL with an index of 0.73 ± 0.12, indicating the presence of flicker-noise in the entire frequency range covered by the observations. In the observed light curve, we identify at least seven episodes during which the source flux drops below 18.4% of the intermediate-state average. Using Bayesian blocks, we characterize these episodes to last between five and 35 days. We used simulated light curves to estimate the probability of chance appearance of these episodes for a variable source characterized by a single log-normal distribution of flux states and a PSD with the same spectral shape as found for the observed light curve. We infer a probability of $\sim 5.4 \times 10^{-5}$ of having the number of continuous (≥15 d) low-flux episodes detected in a simulation greater than or equal to that in our observed light curve. A superposition of two log-normal distributions is sufficient for a simulation to reproduce the seven continuous dip features we observe. On the other hand, a PDF model containing three log-normal components is statistically favored to describe the entire histogram of flux measurements.

Energy spectrum during different flux states. The energy spectra have been extracted in three flux intervals respectively. The binned spectra in the energy range from 2 GeV to 10 GeV implies that the state transitions do not lead to any noticeable change in the IC component up to 10 GeV. After all, the IC component is intrinsically steady during the lifetime of the Crab Nebula, because the responsible low-energy electrons fill a large volume with a cooling timescale exceeding the age of the nebula. We confirm the general trend of a hardening and curvature of the synchrotron spectrum in the high-flux state, which is discussed in Buehler et al. (2012) and Mayer et al. (2013). For the first time, we reconstruct the energy spectrum in the newly found low-flux state. The energy spectrum in the low-flux state and at energies below 2 GeV is roughly consistent with an extrapolation of the IC component of the nebula emission towards lower energies.

Notably, the fitting for the IC component is dominated by the >2 GeV data, leading to a large uncertainty in its extrapolated flux below 600 MeV. Also, we found an energy-dependent spatial extension of the IC nebula, where the size shrinks as the photon energy increases (Yeung & Horns 2019). The extrapolated extension size (the 68% containment radius) at 100 MeV is as large as 0.1°. However, we model the IC component as a point source in this work, which only accounts for a core part of the IC nebula. Therefore, the extrapolated IC flux could have been underestimated while the measured low-state spectrum provides an indication to the actual IC nebula emission.

We therefore conclude from the characterization of the variability and the spectral analysis that the synchrotron nebular emission between 60 MeV and 600 MeV drops well below the average flux on time-scales of several days and remains in a low state for several weeks. During these episodes of low-state emission, the predomination of the nebular energy spectrum by the IC emission demonstrates that the high-energy part of the synchrotron nebula is dramatically depressed on a short time-scale.

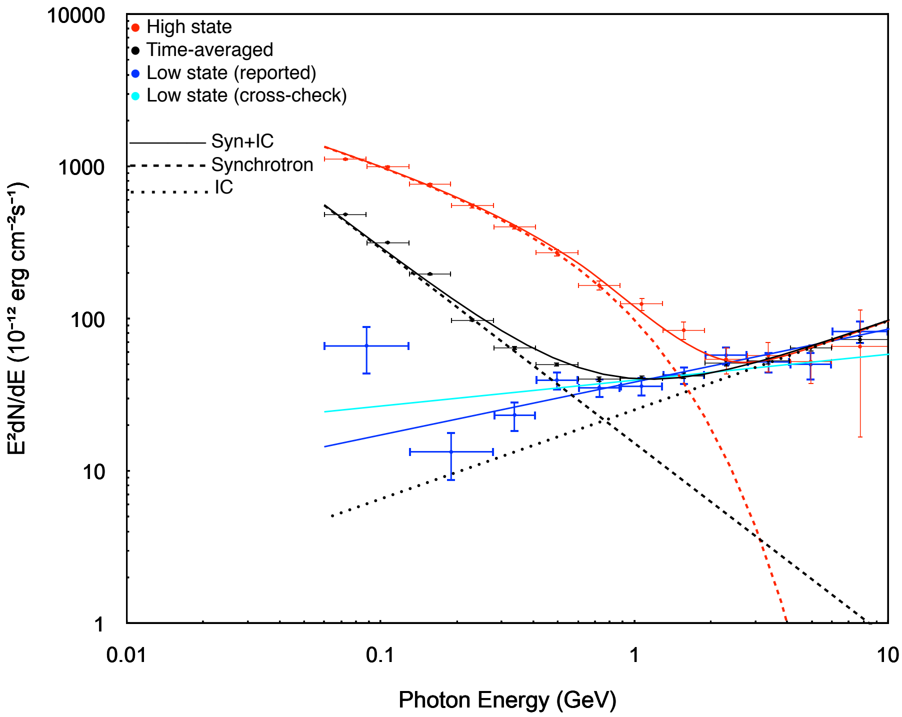

Fig. 6. Spectral energy distributions (SED) of the Crab Nebula for different flux states. The IC component (the dotted line) is determined with the time-averaged spectrum (in black). The spectra of the high and low states (in red and blue respectively) are defined based on the 60 MeV–600 MeV light curve of the Crab Nebula (Fig. 2). The solid lines and the binned spectra represent the total Syn+IC emission, while the dashed lines represent the synchrotron component. For the low state (solid blue line), the combined Syn+IC spectrum is plotted as a single PL component. The solid cyan line is an alternative low-state spectrum for cross-checking (see the text for detail).

Table 4. 60 MeV–10 GeV spectral properties of the Crab Nebula measured in different flux states.

Component	State [b]	PL Γ	PLEC Γ	PLEC E_c (GeV)	$TS_{\rm PLEC} - {\rm TS_{PL}}$ [c]	Integrated flux [d] (10^{-9} cm^{-2} s^{-1})
IC [a]	Average	1.415 ± 0.023	...	...	...	107 ± 5
	High	2.830 ± 0.015	2.497 ± 0.041	0.77 ± 0.10	114.1	8432 ± 92
Synchrotron	Average	3.278 ± 0.011	$3.250, \pm 0.026$	6.6 ± 5.7	1.7	2534 ± 15
	Low	...	...	...	...	370 ± 130
Syn+IC	Low	1.653 ± 0.048	...	...	...	221 ± 22

Notes. [a]The parameters of the IC component are determined from the complete ten-year data set, and are assumed to remain constant. [b]The high and low states are defined based on the 60 MeV–600 MeV light curve of the Crab Nebula (Fig. 2). [c]Γ is the photon index. E_c is the energy of the exponential cutoff. $TS_{\rm PLEC} - {\rm TS_{PL}}$ is the difference in test-statistic (TS) between PLEC and PL. [d]For the high state and the average, the integral fluxes of the synchrotron component are based on PLEC and PL models respectively. For the low state, it is the sum over the binned spectrum subtracting the IC component.

We consider in the following a possible interpretation of a compact emission region which satisfies the requirement that the emission region is causally connected within the variability time-scale found during the transition phase of less than two days. This compact region would be the origin of the bulk of the observed emission such that it would explain simultaneously the rapid dimming of the entire emission, as well as the low-state spectrum which is apparently dominated by the constant flux of the IC nebula. Possible alternative explanations based upon variability of the entire nebula need to circumvent the argument of causal connection. Here, we focus on the well-known inner knot observed near the pulsar's position (Hester et al. 1995) as a possible candidate.

4.2. *Interpretation as synchrotron emission from the inner knot*

With the shortest timescales of transitions between low-flux and intermediate states constrained to be less than two days (95% c.l.), we infer that at least 75% of the $>10^8$ eV emission of the so-called synchrotron nebula originate from a compact region with an extension limited by the light crossing time to be $ct_{\rm var} \approx 4.2\,{\rm mpc}\; t_{\rm var}/(5\,{\rm d})$ which corresponds to an angular diameter (at a distance of 2.2 kpc) of $\theta \approx 0\rlap{.}''4\; t_{\rm var}/(5\,{\rm d})$. The time-scale of variability and the inferred angular extension of $0\rlap{.}''4\; t_{\rm var}/(5\,{\rm d})$ is consistent with the finding of Rudy et al. (2015), where the tangential FWHM of the knot was observed to be 0.3″–0.35″. The result of our analysis of the variability therefore strengthens the interpretation that the high-energy part of the synchrotron emission is produced in the inner knot of the Crab Nebula as put forward by Komissarov & Lyutikov (2011).

The inner knot has also been found to show variability in the optical and X-ray band (Rudy et al. 2015) with correlations of the knot's morphology and position with its gamma-ray flux that are similar to the expectations of models of the termination shock (Lyutikov et al. 2016). Further multi-wavelength observations of the inner knot during a phase of the 60 MeV–600 MeV low-state would be essential to confirm the proposed scenario.

Acknowledgements. PKHY acknowledges the support of the DFG under the research grant HO 3305/4-1. We greatly appreciate M. Kerr for providing the ephemeris of the Crab pulsar for phased analysis. PKHY thanks H.-F. Yu for useful discussions. We thank the two anonymous referees for very useful comments which helped to improve the manuscript.

References

Abdo, A. A., Ackermann, M., Ajello, M., et al. 2011, Science, 331, 739
Ackermann, M., Ajello, M., Albert, A., et al. 2012, ApJS, 203, 4
Aharonian, F., Akhperjanian, A., Beilicke, M., et al. 2004, ApJ, 614, 897
Atoyan, A. M., & Aharonian, F. A. 1996, MNRAS, 278, 525
Buehler, R., Scargle, J. D., Blandford, R. D., et al. 2012, ApJ, 749, 26
Bühler, R., & Blandford, R. 2014, Rep. Prog. Phys., 77, 066901
Connolly, S. D. 2015, ArXiv e-prints [arXiv:1503.06676]
de Jager, O. C., & Harding, A. K. 1992, ApJ, 396, 161
Dubner, G., Castelletti, G., Kargaltsev, O., et al. 2017, ApJ, 840, 82
Emmanoulopoulos, D., McHardy, I. M., & Papadakis, I. E. 2013, MNRAS, 433, 907
Fraschetti, F., & Pohl, M. 2017, MNRAS, 471, 4856
Gunn, J. E., & Ostriker, J. P. 1971, ApJ, 165, 523
Hester, J. J. 2008, Ann. Rev. Astron. Astrophys., 46, 127
Hester, J. J., Scowen, P. A., Sankrit, R., et al. 1995, ApJ, 448, 240
Hillas, A. M., Akerlof, C. W., Biller, S. D., et al. 1998, ApJ, 503, 744
Komissarov, S. S., & Lyutikov, M. 2011, MNRAS, 414, 2017
Kuiper, L., Hermsen, W., Cusumano, G., et al. 2001, A&A, 378, 918
Ling, J. C., & Wheaton, W. A. 2003, ApJ, 598, 334
Lobanov, A. P., Horns, D., & Muxlow, T. W. B. 2011, A&A, 533, A10
Lyutikov, M., Komissarov, S., & Porth, O. 2016, MNRAS, 456, 286
Martín, J., Torres, D. F., & Rea, N. 2012, MNRAS, 427, 415
Meyer, M., Horns, D., & Zechlin, H.-S. 2010, A&A, 523, A2
Mayer, M., Buehler, R., Hays, E., et al. 2013, ApJ, 775, L37
Rees, M. 1971, J. Nat. Phys. Sci., 230, 55
Rudy, A., Horns, D., DeLuca, A., et al. 2015, ApJ, 811, 24
Scargle, J. D., Norris, J. P., Jackson, B., & Chiang, J. 2013, ApJ, 764, 167
Spitkovsky, A., & Arons, J. 2004, ApJ, 603, 669
Striani, E., Tavani, M., Vittorini, V., et al. 2013, ApJ, 765, 52
Tam, H., & Yang, Q. 2012, Phys. Lett. B, 716, 435
Tavani, M., Bulgarelli, A., Vittorini, V., et al. 2011, Science, 331, 736
The Fermi-LAT Collaboration 2019, ArXiv e-prints [arXiv:1902.10045]
Trimble, V. 1968, ApJ, 73, 535
Volpi, D., Del Zanna, L., Amato, E., & Bucciantini, N. 2008, A&A, 485, 337
Wilson-Hodge, C. A., Cherry, M. L., Case, G. L., et al. 2011, ApJ, 727, L40
Yeung, P. K. H., & Horns, D. 2019, ApJ, 875, 123

Chapter 5

Inferring the Origins of the Pulsed Gamma-ray Emission from the Crab Pulsar

In this chapter, we re-investigate the γ-ray phaseograms and phase-resolved SEDs of the Crab pulsar, with the 60 MeV–500 GeV LAT data accumulated from 2008 August 4 to 2018 August 20. Considering our LAT results and observations of IACT telescopes synthetically, we inferred the dominating γ-ray origins for different phase intervals individually. Contents of this sub-topic have been published in Yeung (2020), whose publisher version is presented below *(Credit: Paul K. H. Yeung, Astronomy & Astrophysics, 640, A43 (2020), reproduced with permission © European Southern Observatory)*. The nebular spectrum reconstructed in Figure 3 of this publication is also a part of our project proposal which is associated with our research grant HO 3305/4-1 from the DFG.

My contributions to this publication. I was encouraged by my supervisor Prof. Dr. Dieter Horns to publish this paper as a single author. I did all data analyses, fittings and calculations myself. Again, I used the *Fermi* Science Tools v11r5p3 package introduced in Chapter 2 to reduce and analyse Fermi LAT data. In phase-resolved analyses on Fermi LAT data in Sections 3.1, 3.3 and 3.4, I adopt the timing solution of the Crab pulsar provided by Dr. Matthew Kerr (documented in Appendix A). As suggested by my supervisor, I implemented the wavelet analyses in Section 3.2, with the "wavelets" package [1] developed by Aaron O'Leary based on the guide of Torrence and Compo (1998). My supervisor had some useful discussions with me about Section 3.4, Figure 9 and Table 4 (the relevant program code, which is initially written by my supervisor Prof. Dr. Dieter Horns and then finalised by me, and our respective contributions are

[1] Code in GitHub: `https://github.com/aaren/wavelets`

documented in Appendix B.2). My supervisor also proposed the ideas to have Table 1 and Figures 2 & 10, and gave me useful comments on formatting some figures and tables. The whole manuscript is written by myself, while my supervisor proofread the Section 1 (Introduction). The data points of the theoretical-phenomenological model lines overlaid in Figure 10 are all provided by Dr. David Carreto Fidalgo.

Supplementary information to Section 3.4 of this publication is presented in Appendix C.4. In addition to the contents of this publication, I conduct further investigations into the long-term temporal behaviour of the pulsed γ-rays from the Crab (see Appendix C.5).

A&A 640, A43 (2020)
https://doi.org/10.1051/0004-6361/202038166

Astronomy & Astrophysics

Inferring the origins of the pulsed γ-ray emission from the Crab pulsar with ten-year *Fermi*-LAT data*

Paul K. H. Yeung

Institute for Experimental Physics, Department of Physics, University of Hamburg, Luruper Chaussee 149, 22761 Hamburg, Germany
e-mail: kin.hang.yeung@desy.de

Received 14 April 2020 / Accepted 6 June 2020

ABSTRACT

Context. The Crab pulsar is a bright γ-ray source, which has been detected at photon energies up to ~1 TeV. Its phase-averaged and phase-resolved γ-ray spectra below 10 GeV exhibit exponential cutoffs, while those above 10 GeV apparently follow simple power laws.

Aims. We re-visit the γ-ray properties of the Crab pulsar with ten-year *Fermi* Large Area Telescope (LAT) data in the range of 60 MeV–500 GeV. With the phase-resolved spectra, we investigate the origins and mechanisms responsible for the emissions.

Methods. The phaseograms were reconstructed for different energy bands and further analysed using a wavelet decomposition. The phase-resolved energy spectra were combined with the observations of ground-based instruments, such as MAGIC and VERITAS, to achieve a larger energy converage. We fitted power-law models to the overlapping energy spectra from 10 GeV to ~1 TeV. In the fit, we included a relative cross-calibration of energy scales between air-shower-based gamma-ray telescopes with the orbital pair-production telescope from the *Fermi* mission.

Results. We confirm the energy-dependence of the γ-ray pulse shape and, equivalently, the phase-dependence of the spectral shape for the Crab pulsar. A relatively sharp cutoff at a relatively high energy of ~8 GeV is observed for the bridge-phase emission. The $E > 10$ GeV spectrum observed for the second pulse peak is harder than those for other phases.

Conclusions. In view of the diversity of phase-resolved spectral shapes of the Crab pulsar, we tentatively propose a multi-origin scenario where the polar-cap, outer-gap, and relativistic-wind regions are involved.

Key words. pulsars: individual: Crab pulsar – gamma rays: stars

1. Introduction

The Crab pulsar and its nebula are products of the supernova explosion SN1054 and act as powerful particle accelerators. The Crab pulsar is one of the 239 pulsars whose γ-ray pulsations have been significantly detected with the on-board *Fermi* Large Area Telescope (LAT; Fermi-LAT Collaboration 2020). Also, it is the only pulsar with pulsed emissions above 100 GeV, which have been robustly confirmed by the ground-based instruments MAGIC and VERITAS (e.g. VERITAS Collaboration 2011; Aleksić et al. 2012). Recently, pulsed emission has been detected even up to TeV energies from the Crab pulsar (Ansoldi et al. 2016).

The relevant emission mechanisms of γ-rays from pulsars are still under investigation. A number of particle acceleration sites have been proposed as origins of pulsed γ-ray emission. The first one proposed is the polar cap region, which is confined in the open magnetosphere at low altitudes (Sturrock 1971; Harding et al. 1978; Daugherty & Harding 1982). Due to rapid pair creations under a strong magnetic field, polar cap models predict a sharp super-exponential cutoff at several GeV, which is not consistent with the observed γ-ray spectra of pulsars (Abdo et al. 2013).

The second and third proposed regions are both located at high altitudes in the outer magnetosphere. They are respectively the slot gap along the last open magnetic field lines (Arons 1983; Dyks & Rudak 2003; Muslimov & Harding 2004), and outer gap extending to the edge of the light cylinder (Cheng et al. 1986, 2000; Romani & Yadigaroglu 1995; Takata et al. 2006). The *Fermi*-LAT pulse profiles and spectra of pulsars demonstrate that the responsible high-energy electron beams have a fan-like geometry scanning over a large fraction of the outer magnetosphere (Abdo et al. 2013). This favours the outer gap emission as a generally dominant component.

As observed with *Fermi*-LAT, MAGIC, and VERITAS, at most on-pulse phases, the Crab pulsar's spectrum above 10 GeV follows a rather hard power-law tail which extends beyond hundreds of GeV (Aleksić et al. 2014; Nguyen & VERITAS Collaboration 2015; Ansoldi et al. 2016). This certainly disfavours domination by the magnetospheric synchrotron-curvature mechanism, whose spectrum is theoretically expected to be well-characterised by an exponential cutoff at several GeV due to magnetic pair-creations and/or radiation losses (Cheng et al. 1986; Romani 1996; Muslimov & Harding 2004; Takata et al. 2006; Tang et al. 2008). On the other hand, it has been put forward by Harding & Kalapotharakos (2015) that magnetospheric synchrotron-self-Compton (SSC) emission from leptonic pairs, which are generated by cascades, can account for the GeV spectral properties observed for the Crab pulsar.

In addition, the fourth particle acceleration site, which is the relativistic wind located outside the light cylinder, is proposed as a responsible region as well (Bogovalov & Aharonian 2000; Aharonian & Bogovalov 2003; Aharonian et al. 2012). More recently, it has been suggested that the highest energy pulsed

* The data point values in Figs. 1, 3, 4, and 9 are only available at the CDS via anonymous ftp to cdsarc.u-strasbg.fr (130.79.128.5) or via http://cdsarc.u-strasbg.fr/viz-bin/cat/J/A+A/640/A43

emission could be produced in the region of the current sheet at a distance of 1–2 light cylinder radii (Harding et al. 2018) or that it even extends to tens of light cylinder radii (Arka & Dubus 2013; Mochol & Petri 2015), where the kinetic-energy dominated wind is assumed to be launched.

It is noteworthy that the Crab pulsar has an energy-dependent γ-ray pulse shape, and equivalently, a phase-dependent spectral shape (e.g. Fierro et al. 1998; Abdo et al. 2010; DeCesar 2013). This may suggest that emissions at different pulse phases are dominated by different emission regions.

In this work, we re-visit the γ-ray phaseograms and phase-resolved spectral energy distributions (SEDs) of the Crab pulsar, with the >60 MeV LAT data accumulated over $\sim$10 years. Considering our LAT results in context with observations of ground-based instruments, we discuss the γ-ray origins for different phases individually.

2. Data reduction and analysis

We perform a series of binned maximum-likelihood analyses (with an angular bin size of 0.1°) for a region of interest (ROI) of 30° × 30° centred at RA = $05^{h}34^{m}31^{s}.94$, Dec=+22°00′52.″2 (J2000), which is approximately the radio centre of the Crab Nebula (Lobanov et al. 2011). We use the data of 60 MeV–500 GeV photon energies, registered with the LAT between 2008 August 4 and 2018 August 20. The data are reduced and analysed with the aid of the *Fermi* Science Tools v11r5p3 package.

Considering that the Crab Nebula is quite close to the Galactic plane (with a Galactic latitude of −5.7844°), we adopt the events classified as Pass8 “clean” class for the analysis so as to better suppress the background. The corresponding instrument response function (IRF) “P8R2_CLEAN_V6” is used throughout the investigation. We further filter the data by accepting only the good time intervals where the ROI was observed at a zenith angle less than 90° so as to reduce the contamination from the albedo of Earth. In phase-resolved analyses, we adopt the timing solution of the Crab pulsar provided by M. Kerr.

In order to account for the contribution of diffuse background emission, we include the Galactic background (gll_iem_v06.fits), the isotropic background (iso_P8R2_CLEAN_V6_v06.txt) as well as all other point sources catalogued in the LAT eight-year point source catalogue (4FGL; Fermi-LAT Collaboration 2020) within 32° from the ROI centre in the source model. We set free the spectral parameters of the sources within 10° from the ROI centre (including the prefactor and index of the Galactic diffuse background as well as the normalisation of the isotropic background) in the analysis. For the sources at angular separation beyond 10° from the ROI centre, their spectral parameters are fixed to the catalogue values.

The three point sources located within the nebula are catalogued as 4FGL J0534.5+2200, 4FGL J0534.5+2201i, and 4FGL J0534.5+2201s, which model the Crab pulsar, the IC, and synchrotron components of the Crab Nebula, respectively. In some cases, we fix the parameters of one or two components or even remove them from the source model, so as to avoid degeneracies in the fitting procedure.

3. Results

3.1. LAT phaseograms at different energies

First of all, we look into the LAT pulse profiles of the Crab pulsar in four energy bands: 60–600 MeV, 0.6–6 GeV, 6–60 GeV, and 20–500 GeV. We divide the full-phase into 50 bins (i.e. each bin covers a phase interval of 0.02). In the maximum-likelihood analysis for each bin, we remove 4FGL J0534.5+2201i and 4FGL J0534.5+2201s from the source model, and assign a single power-law (PL) to 4FGL J0534.5+2200 (i.e. the total emission of the Crab pulsar and its nebula is modelled as one component here). We adopt the same convention of phase as in Buehler et al. (2012).

The preliminary phaseograms show the first peak within the phase range of 0.98–0.02 and the second peak within phase 0.37–0.41. In order to localise the two peaks, we sub-divide phase 0.98–0.02 and 0.37–0.41 into bins of 0.01 phase interval, and then further sub-divide phase 0.99–0.01 and 0.38–0.40 into even smaller bins of 0.005 phase interval. Phase 0.58–0.88 is taken as the off-pulse region (thereafter OFF) where we determine the un-pulsed nebular fluxes. In each phaseogram, we combine those bins within OFF into 1 bin and then subtract the determined nebular flux from all bins, such that the flux within OFF is set at 0. The finalised phaseograms are plotted in Fig. 1, together with the >85 GeV phaseogram observed by VERITAS (Nguyen & VERITAS Collaboration 2015). The phase-averaged flux in each energy band we investigate is also overlaid in the phaseogram.

Comparing all LAT phaseograms presented here, we have no evidence for any phase shift of the two peaks (<1σ; see Table 1). According to the pulse shapes, we divide the on-pulse region into 7 phase ranges for detailed analyses: Phase 0.88–0.96 (the leading wing of the first pulse; LW1), 0.96–0.02 (the peak region of the first pulse; P1), 0.02–0.12 (the trailing wing of the first pulse; TW1), 0.12–0.20 (the bridge between two pulses; BD), 0.20–0.36 (LW2), 0.36–0.42 (P2) and 0.42–0.58 (TW2).

In 60–600 MeV and 0.6–6 GeV, the ratios of maximum fluxes of P1 to P2 are 2.60 ± 0.05 and 2.85 ± 0.08, respectively. This ratio greatly decreases to 1.54 ± 0.23 in 6–60 GeV and to 1.14 ± 0.59 in 20–500 GeV. It further drops to an even smaller value of 0.57 ± 0.09 in the >85 GeV band.

From 60–600 MeV to 0.6–6 GeV, the fractional flux of BD increases from (1.82 ± 0.09)% to (3.15 ± 0.07)%. This fraction further rises to (8.38 ± 0.73)%, (4.7 ± 4.4)% and (11.1 ± 4.2)% in 6–60 GeV, 20–500 GeV and >85 GeV respectively.

3.2. Wavelet analyses on LAT phaseograms

At any photon energy, the flux of the Crab pulsar changes exponentially during the wing phases. In order to investigate the instantaneous rates of flux change at different phases and energies, we apply continuous wavelet transforms to the preliminary LAT phaseograms which have a uniform bin size of a 0.02 phase interval. The Ricker wavelet is adopted. The photon statistics above 20 GeV are not sufficient for the wavelet transform. The results are shown in Fig. 2.

The wavelet scale represents the timescale of flux change. Overall, at higher energies, the wavelet components at LW1 and TW2 extend to lower wavelet scales and become closer to vertical, while the components at TW1, LW2 and BD have greater power indices and become more tightly connected with each other.

Considering the pulse profiles and wavelet transformations synthetically, we derive a number of general trends: As the photon energy increases,

(a) the rate of flux increase in LW1 becomes faster, leading to a narrower wing;

(b) the rate of flux decrease in TW1 becomes slower, leading to a broader wing;

(c) the rate of flux increase in LW2 becomes slower, leading to a broader wing;

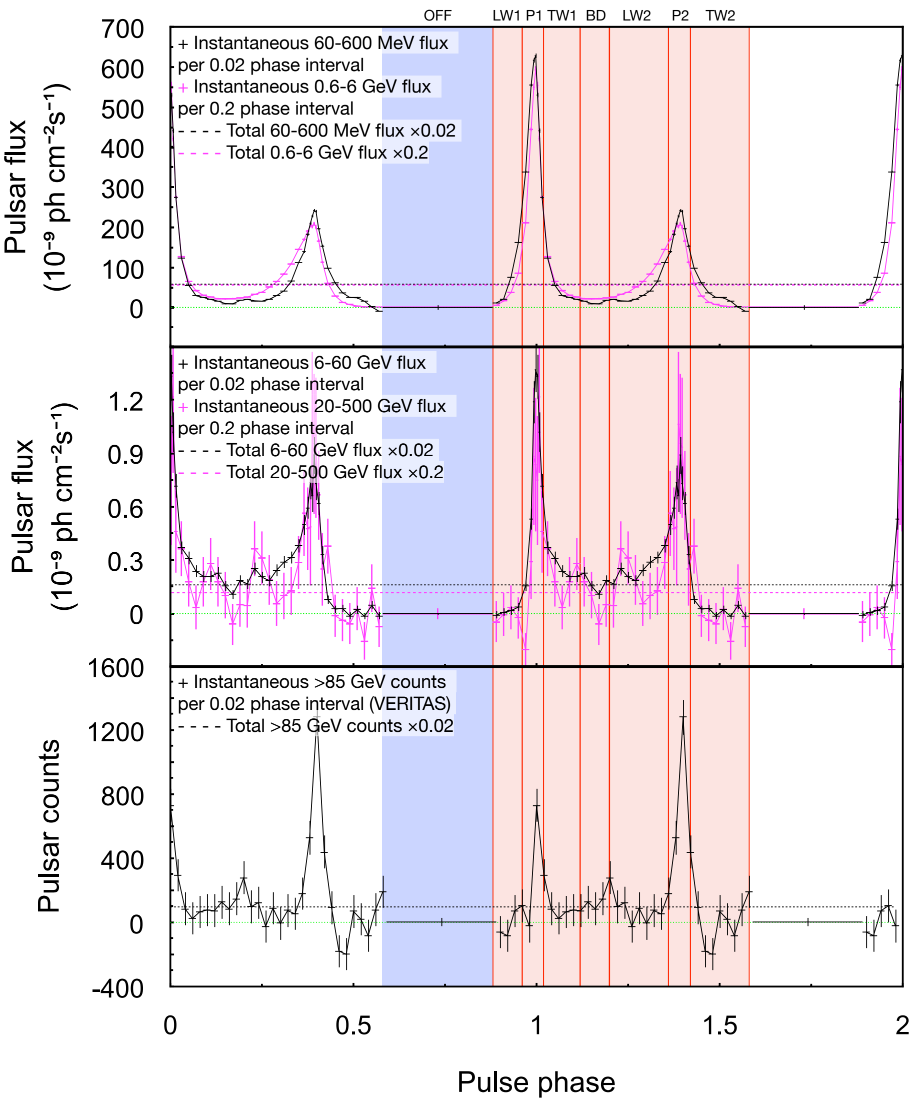

Fig. 1. Phaseograms of the Crab pulsar in different energy bands. The >85 GeV phaseogram observed by VERITAS (*bottom panel*) is taken from Nguyen & VERITAS Collaboration (2015).

(d) the rate of flux decrease in TW2 becomes faster, leading to a narrower wing;

(e) the flux ratio of P1 to P2 drops;

(f) the fractional flux of BD rises.

The trends (a), (d) and (e) confirm what was reported in Abdo et al. (2010). In the following sub-sections, we further examine the trends (a)–(f) with spectral analyses.

3.3. LAT SEDs for different pulse phases

3.3.1. Scheme of spectral analyses

In broadband spectral analyses, we enable the energy dispersion correction which operates on the count spectra of most sources including the entire Crab pulsar/nebula complex, following the recommendations of the *Fermi* Science Support Center. The energy spectrum of the un-pulsed nebular emission in the 60 MeV–100 GeV band is reconstructed by fitting a two-component (additive) model to the data collected during OFF. The flux normalisation of the pulsar component is fixed at 0. Similar to previous studies (Buehler et al. 2012; Yeung & Horns 2020), we assign the synchrotron component a PL with a photon index constrained within 3–5, and assign the IC component a log-parabola (LP):

$$\frac{\mathrm{d}N}{\mathrm{d}E} = N_0\left(\frac{E}{10\,\mathrm{GeV}}\right)^{-(\alpha+\beta\ln(E/10\,\mathrm{GeV}))},$$

where α is constrained within 0–2. It turns out that the synchrotron component has a PL index of 3.427 ± 0.019 and an

Table 1. Pulse peak phases determined from LAT phaseograms.

Energy band (GeV)	Peak 1 [(a)]	Peak 2 [(b)]
0.06–0.6	0.997 ± 0.004	0.393 ± 0.004
0.6–6	0.998 ± 0.004	0.389 ± 0.005
6–60	0.998 ± 0.004	0.391 ± 0.005
20–500	0.003 ± 0.006	0.392 ± 0.004

Notes. [(a)]It is calculated as the arithmetic mean of phases in 0.98–0.02 weighted by relative fluxes. [(b)]It is calculated as the arithmetic mean of phases in 0.36–0.42 weighted by relative fluxes.

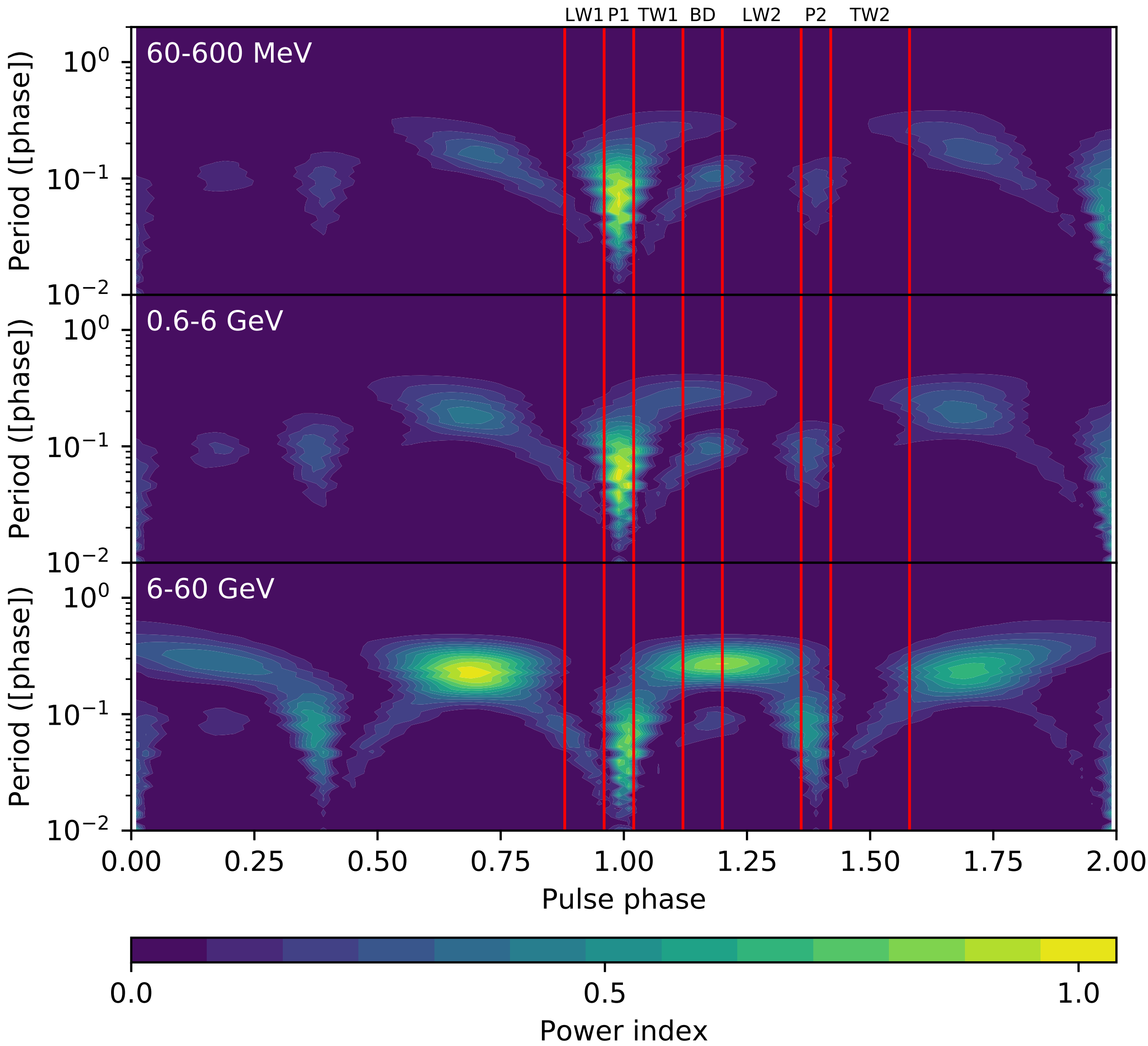

Fig. 2. Wavelet maps of the preliminary LAT phaseograms in three exclusive energy bands. A continuous Fourier transform is applied in the period domain for each phaseogram. The Ricker wavelet is adopted. The power index (the colour scale) is defined as the variance per unit period per unit phase divided by the maximum. Each red vertical line is a border between two phase ranges we define.

integrated flux of $(2.500 \pm 0.018) \times 10^{-6}$ ph cm^{-2} s^{-1} in the full phase, while the LP parameters of the IC component are determined to be $\alpha = 1.759 \pm 0.023$, $\beta = 0.106 \pm 0.014$ and $N_0 = (5.12 \pm 0.14) \times 10^{-13}$ cm^{-2} s^{-1} MeV^{-1} (scaled to the full phase).

Then, we apply this nebular model to reconstruct the pulsar spectra at different phases in the same energy band. We examine how well the pulsar spectrum at each phase is described by, respectively, a power law with a super- or sub-exponential cutoff (PLSEC):

$$\frac{\mathrm{d}N}{\mathrm{d}E} = N_0 \left(\frac{E}{E_0}\right)^{-\Gamma} \exp\left[-\left(\frac{E}{E_c}\right)^{\lambda}\right],$$

and a power law with an exponential cutoff (PLEC) where λ in PLSEC is fixed at 1. The pulsar parameters are left free while the nebular parameters are fixed at the determined values (with proper scalings to flux normalisations according to phase intervals). The obtained spectral models for the pulsar are tabulated in Table 2. The phase-averaged pulsar spectrum is plotted with the nebular spectrum in Fig. 3, and the phase-resolved pulsar spectra are plotted in Fig. 4. Each presented flux has been scaled by the inverse of the phase interval (i.e. it refers to as the flux per unit phase). The spectral parameters for individual phase bins of 0.04 are plotted in Figs. 5 and 6.

We repeat this chain of exercise for the 10–500 GeV band. For the nebular emission, the synchrotron component is negligible, so we remove it from the source model. The nebular IC component is still modelled as a LP, while the pulsar component is modelled as a PL. The best-fit parameters for the nebula are $\alpha = 1.86 \pm 0.14$, $\beta = 0.023 \pm 0.047$ and $N_0 = (5.10 \pm 0.42) \times 10^{-13}$ cm^{-2} s^{-1} MeV^{-1} (scaled to the full phase). The results are tabulated in Table 3 and are overlaid in Figs. 3 and 4. We also examine how significant the improvement is when we assign a curved model to the pulsar spectrum. Since the photon index at BD appears to be higher, we adjust the phase width of BD and

Table 2. 60 MeV–100 GeV spectral properties of the Crab pulsar at different phases.

Phase	PLEC Γ	PLEC E_c (MeV)	PLSEC Γ	PLSEC E_c (MeV)	PLSEC λ	PLSEC F(60 MeV–100 GeV) [(a)] (10^{-6} cm^{-2} s^{-1})	ΔTS [(b)]
Full-phase	1.851 ± 0.004	4259 ± 80	1.328 ± 0.006	38.1 ± 1.5	0.308 ± 0.002	3.10 ± 0.01	512
LW1	1.757 ± 0.021	1137 ± 55	0.888 ± 0.026	9.53 ± 0.76	0.351 ± 0.005	3.11 ± 0.03	32.1
P1	1.827 ± 0.005	2750 ± 51	0.870 ± 0.007	0.51 ± 0.01	0.238 ± 0.001	22.93 ± 0.07	609
TW1	1.831 ± 0.010	9181 ± 626	1.790 ± 0.033	7349 ± 1594	0.791 ± 0.122	2.64 ± 0.03	3.2
BD	1.507 ± 0.032	7792 ± 922	1.501 ± 0.078	7607 ± 2522	0.979 ± 0.244	0.56 ± 0.03	0.01
LW2	1.634 ± 0.010	4646 ± 175	1.500 ± 0.040	2244 ± 564	0.658 ± 0.062	2.38 ± 0.02	27.7
P2	1.911 ± 0.006	6129 ± 259	1.660 ± 0.074	708 ± 612	0.415 ± 0.068	10.03 ± 0.06	93
TW2	1.954 ± 0.026	1870 ± 164	1.029 ± 0.036	0.97 ± 0.09	0.256 ± 0.003	1.36 ± 0.02	17.7

Notes. [(a)]The integrated flux per unit phase. [(b)]The difference in test-statistic (TS) between PLSEC and PLEC. Its square root is the significance at which PLSEC is preferred over PLEC.

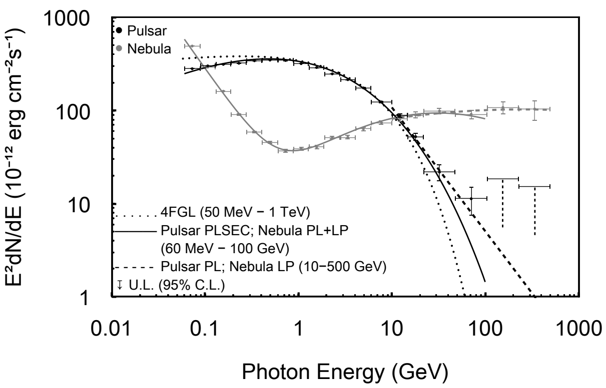

Fig. 3. Phase-averaged LAT SEDs of the Crab pulsar and the Crab Nebula. The 4FGL model for the Crab pulsar, reconstructed with fixing λ at 2/3, is overlaid for comparison. All upper limits presented are at a 95% confidence level. We overlay the 60 MeV–100 GeV spectrum predicted by PLSEC and the 10–500 GeV spectrum predicted by PL.

study the evolution of the photon index (Fig. 7). The narrowest phase width of BD we investigate is 0.05 for which the Crab pulsar is detected at a $\sim 4\sigma$ significance.

We proceed to generate binned spectra for the nebula and pulsar. We divide the 60 MeV–6 GeV band into 12 discrete energy bins (six bins per decade). 6–10 GeV is the 13th bin. The 10–500 GeV band is divided into five discrete bins, the first of which is further split into two. The procedures of broadband fittings are also applied to the spectral fittings of each bin. The nebular emission in each bin is modelled as a PL with an index fixed at a value derived from the broadband fitting. The results are overlaid in Figs. 3 and 4 as well.

Based on the binned spectra, we compute the pulsed fraction of the entire Crab pulsar/nebula complex, as well as the pulsar flux ratios between different pairs of phases at energies from 60 MeV to 100 GeV (plotted in Fig. 8). The pulsed fraction is defined as $(F_{\rm max} - F_{\rm min})/(F_{\rm max} + F_{\rm min})$, where $F_{\rm min}$ is the nebular flux, and $F_{\rm max}$ is the pulsar flux in either P1 or P2 (the higher one) added to the nebular flux.

3.3.2. Summary of spectral properties

The pulsed fraction of the entire Crab pulsar/nebula complex is strongly dependent on the photon energy (see Fig. 8). It is $\gtrsim 90\%$ (and $\gtrsim 80\%$) in 0.2–4 GeV (and 0.1–8 GeV). It drops to 25–50% in 20–100 GeV.

For the phase-averaged pulsar spectrum in 60 MeV–100 GeV, a PLSEC with $\lambda \approx 0.31$ fits the data better than PLEC, indicating that a sub-exponential cutoff is strongly favoured. It is comforting to see that, in 0.2–14 GeV, this PLSEC model agrees within 15% with the 4FGL model reconstructed with fixing λ at 2/3. The λ values are widely varying with the pulse phase (see Fig. 6 and Table 2). Noticeably, during the phase 0.04–0.28, λ is consistent with 1 within the tolerance of statistical uncertainties and PLSEC is not significantly preferred over PLEC ($\lesssim 1\sigma$). In a PLSEC model, there is a strong correlation of λ with any other parameter, making it nonsensical to compare their values among different phases. Instead, we compare the Γ and E_c values of PLEC models among different phases.

The PLEC model for the full-phase spectrum has a photon index $\Gamma \approx 1.85$ and a cutoff energy $E_c = 4.3 \pm 0.1$ GeV. During the phase 0.08–0.36 (and 0.16–0.28), PLEC fittings yield harder Γ of $\lesssim 1.7$ (and ~ 1.45). During the phase 0.04–0.16 and 0.16–0.24, E_c of PLEC is as high as ~ 10.5 GeV and ~ 6 GeV, respectively (see Fig. 5). These indicate that the total fractional flux of TW1, BD and LW2 generally increases with the photon energy. As follows, we summarise the <10 GeV spectral properties of the Crab pulsar based on PLEC and binned spectra (see Figs. 3, 4 and 8 as well as Table 2), and relate them to the trends (a)–(f) derived in Sect. 3.2.

(i) The Γ value at LW1 is lower than that at P1 by 0.07 ± 0.02. On the other hand, the E_c value at LW1 is about 40% of that at P1. The flux ratio of LW1 to P1 is strongly decreasing in 0.5–10 GeV, confirming the trend (a).

(ii) Γ at TW1 and that at P1 are consistent with each other within the tolerance of statistical uncertainties, and E_c at TW1 is three times higher than that at P1. The flux ratio of TW1 to P1 is strongly increasing in 0.5–10 GeV, confirming the trend (b).

(iii) Γ at LW2 is significantly lower than that at P2 by 0.28 ± 0.01. On the other hand, E_c at LW2 is about three-fourth of that at P2. At ~ 250 MeV, the flux ratio of LW2 to P2 starts rising with the photon energy significantly. This increment might come to an end at >4 GeV. Hence, we have strong evidence for the validity of the trend (c) in 0.25–4 GeV.

(iv) Γ at TW2 is consistent with that at P2 (the difference is only at a $\sim 1.6\sigma$ significance), and E_c at TW2 is approximately 30% of that at P2. At ~ 350 MeV, the flux ratio of TW2 to P2 starts dropping with the photon energy significantly. This

A&A 640, A43 (2020)

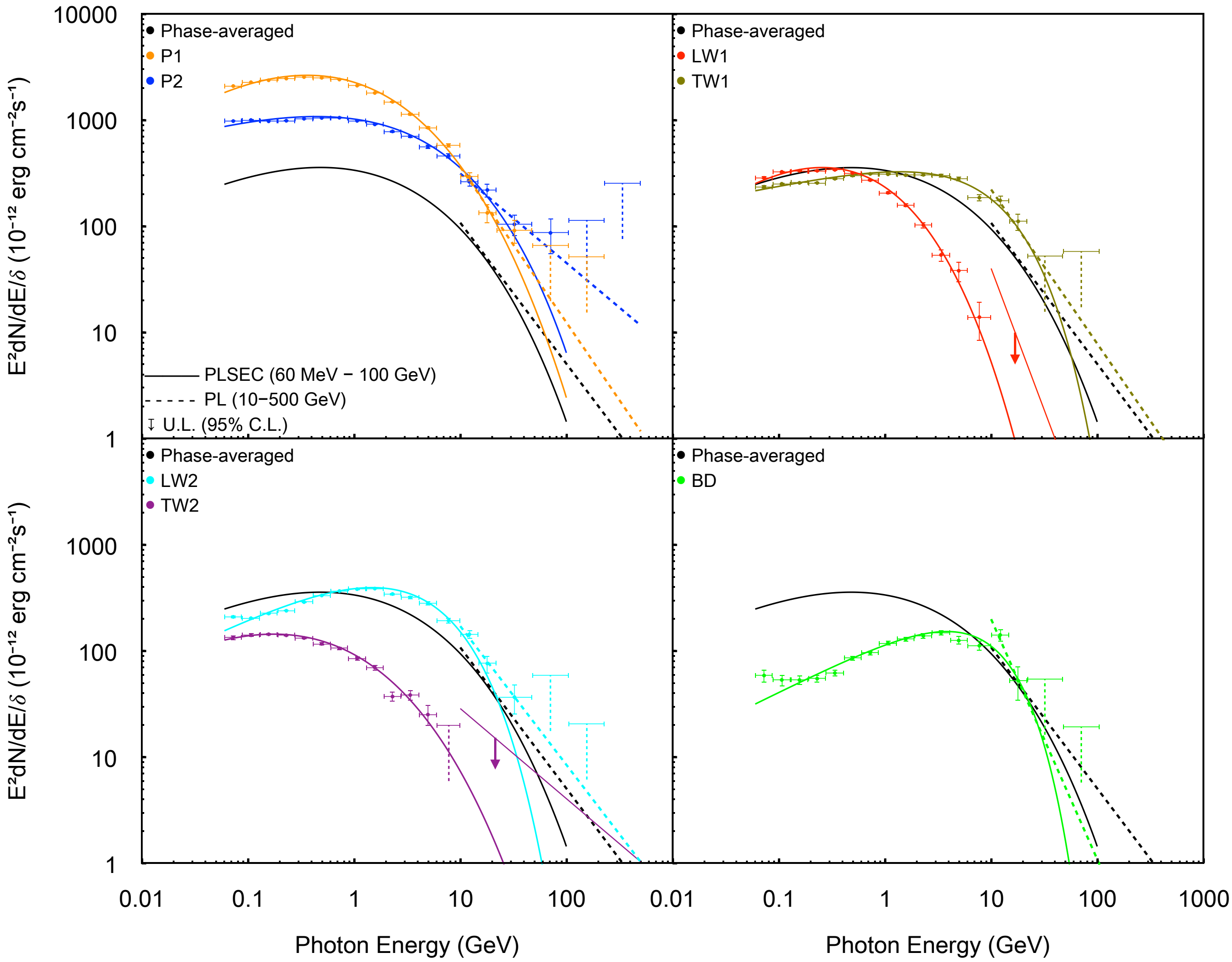

Fig. 4. Phase-resolved LAT SEDs of the Crab pulsar. The vertical axis of each panel shows the differential flux per unit phase (δ). All upper limits presented are at a 95% confidence level. For each phase we investigate, we overlay the 60 MeV–100 GeV spectrum predicted by PLSEC and the 10–500 GeV spectrum predicted by PL. The model lines fit to the phase-averaged pulsar spectrum (Fig. 3) are also overlaid on each panel for comparison. Since the Crab pulsar is not significantly detected ($<2\sigma$) above 10 GeV at LW1 and TW2, the upper limits on differential fluxes at these energies and phases are represented by "ad hoc" PL models (the red and purple straight lines appended with arrows), each of which is determined through iterating the prefactor while fixing the index at the maximum-likelihood value.

decrement might come to an end at >2 GeV. Hence, we have strong evidence for the validity of the trend (d) in 0.35–2 GeV.

(v) Both the Γ values at P1 and P2 closely match the one for the full phase (the differences are $\lesssim$0.06). E_c at P1 is about two-third of that for the full phase, which is about two-third of that at P2. In 60 MeV–1.5 GeV, the fractional flux of P1 is essentially uniform (the percent variance between any two bins is $\lesssim$20%). Above 1.5 GeV, the fractional flux of P1 starts dropping with the photon energy. On the other hand, the fractional flux of P2 remains uniform at energies between 60 MeV and 10 GeV. Hence, the trend (e) is manifested in 1.5–10 GeV.

(vi) BD has the lowest Γ value among all phases we investigate. It is much lower than Γ for the full phase by 0.34 ± 0.03. Also, E_c at BD is higher than that for the full phase by a factor of ~1.8. The fractional flux of BD is robustly increasing in 0.35–10 GeV, confirming the trend (f).

In 10–500 GeV, a PL is sufficient to describe the pulsar spectrum at each phase, and likelihood ratio tests indicate that any curved models are not statistically required ($\lesssim 1\sigma$). Therefore, the energy-dependence of a flux ratio between two phases above 10 GeV can be directly inferred from their difference in the photon index (see Table 3). Exceptionally, the detection significance of the Crab pulsar at LW1 and TW2 is too low ($<2\sigma$) so that the "ad hoc" PL models for these two phases cannot precisely predict the pulsar's differential flux. The photon indices of the Crab pulsar for P1 and TW1 are consistent with each other within the tolerance of statistical uncertainties. The indices for LW2 and P2 are consistent with each other within the tolerance of 1.5σ uncertainties. Therefore, we have no robust evidence for the validities of the trends (a)–(d) at energies above 10 GeV.

Interestingly, while the <3 GeV spectrum of the Crab pulsar is hardest at BD, its >10 GeV spectrum is apparently softest at BD. This is consistent with the relatively sharp cutoff of the BD spectrum reported in Table 2. During the phase 0.135–0.185 (a central interval of BD), the fractional flux drops as $E^{-2.6\pm1.2}$ at a $\sim 3\sigma$ significance (see Fig. 7), indicating a potential reverse of the trend (f) above 10 GeV. The validity of the trend (e) above 10 GeV is examined in the next sub-section with

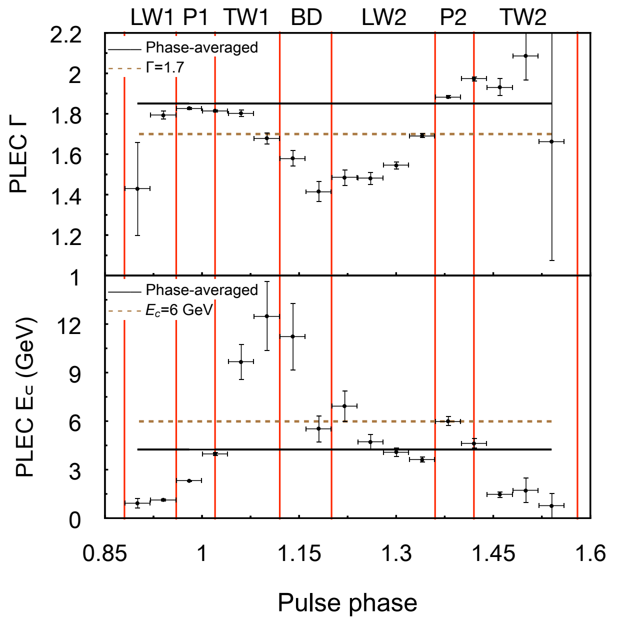

Fig. 5. Photon indices Γ and cutoff energies E_c yielded by PLEC for individual phase bins of 0.04.

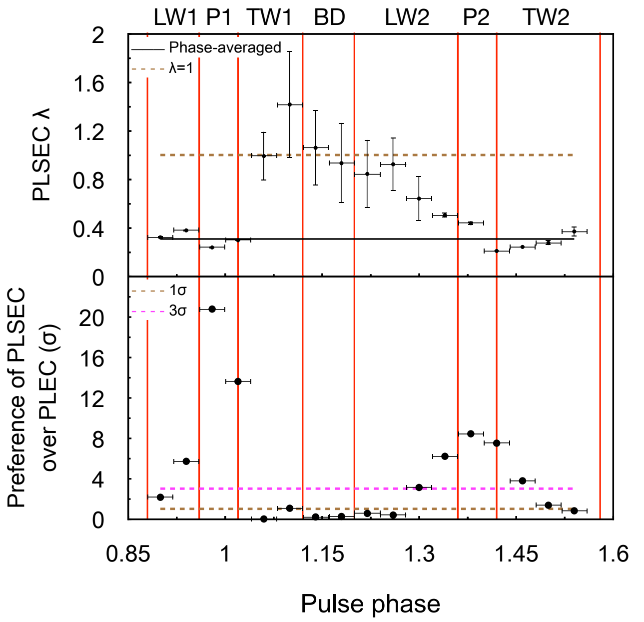

Fig. 6. λ values yielded by PLSEC and preference of PLSEC over PLEC for individual phase bins of 0.04. The latter is computed as the square root of the TS difference between those two models.

joint fits of the LAT and ground-based instruments' spectral points.

3.4. Comparing LAT spectra to observations of ground-based instruments

It is interesting to join the spectral data of LAT and ground-based instruments together for comparisons. Before that, we adjust the phase ranges of the two peaks to be the same as those defined in Ansoldi et al. (2016) (Phase 0.983–0.026

Table 3. 10–500 GeV spectral properties of the Crab pulsar at different phases.

Phase	PL Γ	F(10–500 GeV) [(a)] (10^{-9} cm^{-2} s^{-1})	TS
Full-phase	3.33 ± 0.15	2.90 ± 0.14	698.9
LW1	4.66 ± 0.63	<0.69	0.4
P1	3.47 ± 0.26	9.18 ± 0.79	319.7
TW1	3.45 ± 0.29	5.68 ± 0.53	235.7
BD	4.26 ± 0.59	3.82 ± 0.53	114.5
LW2	3.31 ± 0.25	4.64 ± 0.40	256.8
P2	2.84 ± 0.18	10.64 ± 0.84	354.4
TW2	2.85 ± 1.06	<0.97	4.0

Notes. [(a)] The integrated flux per unit phase.

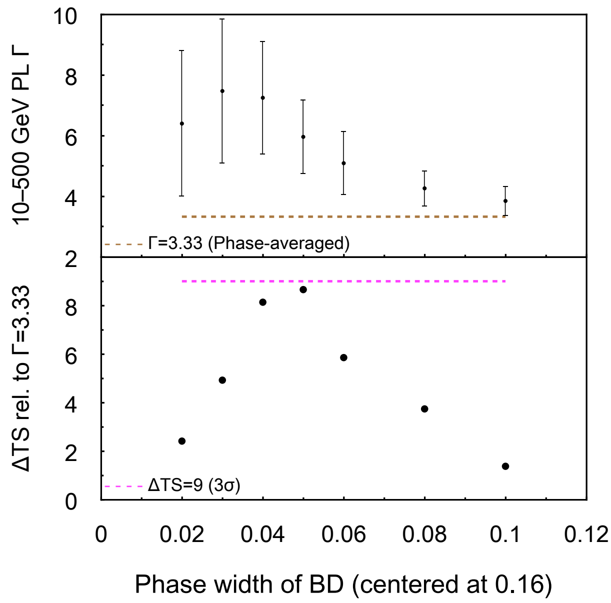

Fig. 7. *Top*: evolution of the 10–500 GeV PL index Γ with adjustments to the phase width of BD. *Bottom*: corresponding TS differences between fixing Γ at the phase-averaged value of 3.33 and leaving it free. Each of their square roots is the significance at which the local spectrum for an adjusted phase interval of BD is softer than the phase-averaged spectrum.

and 0.377–0.422; thereafter P1$_M$ and P2$_M$ respectively). For these two phase ranges, we follow the same scheme to re-compute the LAT fluxes of the Crab pulsar in different energy bins starting from 10 GeV, which are plotted with the MAGIC fluxes in Fig. 9. For the full-phase, the LAT and VERITAS fluxes of the Crab pulsar at >10 GeV (the latter is taken from Nguyen & VERITAS Collaboration 2015) are overlaid in Fig. 9 as well.

It is clearly demonstrated that the phase-averaged VERITAS fluxes at energies above 80 GeV are higher than the extrapolated fluxes of the PLSEC fit to the broadband LAT spectrum. Also, for each phase interval we investigate here, a PL is sufficient to describe the spectrum between 10 GeV and ~1 TeV, and a spectral curvature or break is not statistically required (<1σ).

In order to take into account the differences in energy scale among LAT, MAGIC and VERITAS, we fitted the data set of each phase to a power law with a scaling factor on photon

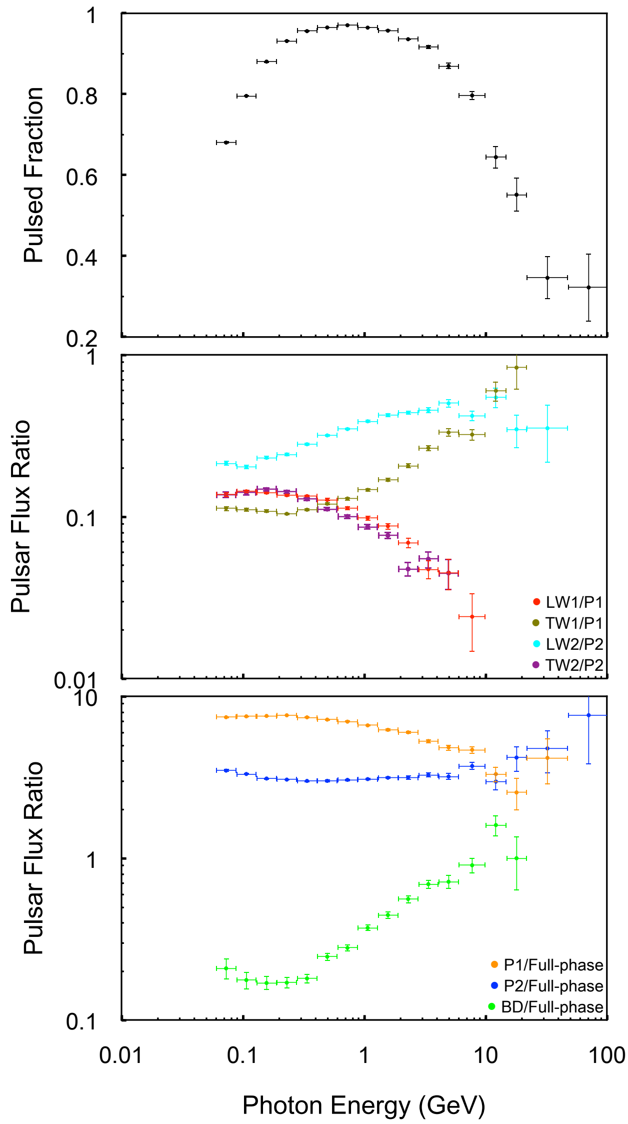

Fig. 8. *Top*: pulsed fraction of the entire Crab pulsar/nebula complex. *Middle and bottom*: flux ratios of the Crab pulsar between different pairs of phases in different energy bins. We recall that each flux has been scaled by the inverse of the phase interval.

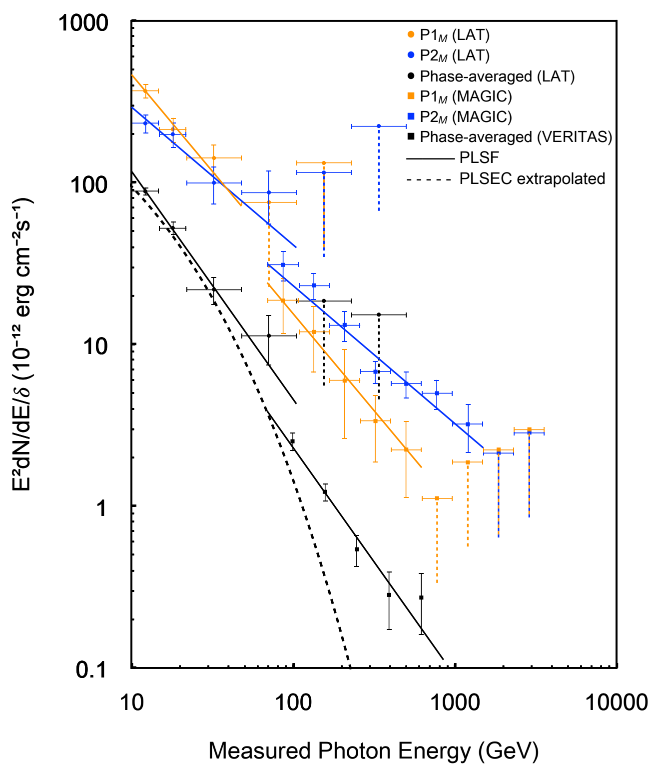

Fig. 9. >10 GeV SEDs of the Crab pulsar at different pulse phases observed with LAT and ground-based instruments. The vertical axis shows the differential flux per unit phase (δ). The horizontal axis shows the measured photon energy (unscaled). Be noted that the orange/blue LAT bins presented here are different from those presented in Fig. 4 because the phase ranges are adjusted for comparison purpose. For each phase we investigate, we overlay the spectrum predicted by the joint-instrument fit of PLSF. The PLSEC fit to the broadband LAT spectrum in the full phase (Fig. 3) and its extrapolation are also overlaid for comparison.

energies measured by ground-based instruments (PLSF):

$$\frac{\mathrm{d}N}{\mathrm{d}E} = \begin{cases} N_0\left(\frac{E}{50\,\mathrm{GeV}}\right)^{-\Gamma} & \text{for LAT data} \\ N_0\left(\frac{\epsilon E}{50\,\mathrm{GeV}}\right)^{-\Gamma} & \text{for data of ground-based instruments} \end{cases}.$$

Since the data for $P1_M$ and $P2_M$ is collected by the same ground-based instrument, their data sets are fit together such that their solutions share the same scaling factor ϵ. The results of fittings are presented in Table 4 and the best-fit model lines are overlaid in Fig. 9.

It is worth mentioning that the ϵ values obtained for MAGIC and VERITAS are both ~1.22. Taking the statistical uncertainties into consideration, they are not significantly larger than 1 ($\leq 1.8\sigma$). It is also comforting to note that the best-fit $\epsilon - 1$ values are only half of a fractional bin width of the ground-based instruments' data. Therefore, we have obtained physically reasonable fits.

It turns out that the photon index Γ for $P1_M$ is lower than that for the full phase by only $\sim 1.2\sigma$, while Γ for $P2_M$ is lower than those for $P1_M$ and the full phase by $\sim 2.1\sigma$ and $\sim 3.6\sigma$ respectively. In other words, as the photon energy increases from 10 GeV to ~1 TeV, the fractional flux of P1 remains constant or even slightly rises back, and that of P2 is significantly rising. The validity of the trend (e) is still suggested at energies >10 GeV. Since the fluxes of LW1 and TW2 account for a negligibly small fraction of $\leq 6\%$ (at a 95% confidence level) above 10 GeV, the rise in total fractional flux of P1 and P2 implies a decline in total fractional flux of TW1, BD and LW2. This strengthens the interpretation that the trend (f) is reversed.

4. Discussion and conclusion

Our pulse profiles, wavelet transformations and spectral analyses for the Crab pulsar both demonstrate the strong dependence of the pulse shape on the photon energy, confirming previous studies. Equivalently, the LAT spectral shape of the Crab pulsar widely varies from phase to phase, indicating multiple origins of γ-ray emissions. According to the change in flux proportion among different phases with energy, the trends (a)–(f) derived in Sect. 3.2 are generally valid below 10 GeV.

At any on-pulse phase we investigate, the broadband LAT spectrum of the Crab pulsar exhibits a (sub-)exponential cutoff

Table 4. Joint fits of the LAT and ground-based instruments' spectral points for the Crab pulsar at different phases.

Phase	Instruments	N_0 $^{(a)}$ (10^{-12} cm^{-2} s^{-1} GeV^{-1})	Γ	ϵ	χ^2/d.o.f.
Full-phase	LAT and VERITAS	3.0 ± 0.5	3.41 ± 0.12	1.22 ± 0.12	3.1/6
P1$_M$	LAT and MAGIC	16.9 ± 2.9	3.20 ± 0.13	1.23 ± 0.14	8.6/14
P2$_M$		18.5 ± 2.6	2.85 ± 0.10		

Notes. The PLSF model is assumed. $^{(a)}$ It has been scaled by the inverse of the phase interval.

at $E_c \lesssim 10$ GeV. We observe a higher PLEC cutoff energy at P2 than at P1 for the Crab pulsar. Interestingly, such a trend is predicted to occur for about 75% of cases in the scenario of a dissipative magnetosphere model, where a relatively larger and azimuthally dependent electric field operates outside the light cylinder (Brambilla et al. 2015).

In the framework of Lyutikov (2012) and Lyutikov et al. (2012) for IC emission within the outer gap, the γ-ray spectrum of a pulsar could also manifest itself as a broken power law whose spectral break would correspond to a break in the electron distribution. This prediction is also consistent with a property observed by LAT and ground-based instruments: The Crab pulsar's spectrum from 10 GeV to ~1 TeV follows a PL tail.

For the spectrum during the phase 0.04–0.24 (covering the whole BD), λ yielded by PLSEC is $\gtrsim$1 and E_c yielded by PLEC is ~(6–10.5) GeV, consistent with an inherent feature (a super-exponential cutoff) predicted in polar cap models (e.g. de Jager 2002; Dyks & Rudak 2004). Such a relatively sharp cutoff is explainable in terms of strong magnetic absorption of low-altitude γ-ray photons above 10 GeV. However, the bridge emission of the Crab pulsar is significantly detected by MAGIC at energies up to 200 GeV (Aleksić et al. 2014). The PL indices of its >10 GeV LAT spectrum (in this work) and >50 GeV MAGIC spectrum (Aleksić et al. 2014) are both ~4. This is not expected in polar cap models.

During LW1, P1, P2, and TW2, a sub-exponential cutoff with $\lambda \leq 0.6$ is strongly favoured to describe the observed spectrum. This rules out the polar cap origin and suggests high-altitude emission zones for these phases. While a traditional outer gap model naturally explains the sub-exponential cutoff detected for the Geminga pulsar (Ahnen et al. 2016), it can only account for the emissions of the Crab pulsar at energies no higher than 10 GeV. The Crab pulsar's spectrum at each pulse peak exhibits a >10 GeV PL tail (in this work) which is much harder than that of the Geminga pulsar (Ahnen et al. 2016), and the tail for P2 even extends to 1.5 TeV without a spectral break (Ansoldi et al. 2016). Therefore, a more complicated scenario is required to explain the spectral properties of the Crab pulsar at P1 and P2.

The IC γ-rays (including SSC emission) from magnetospheric acceleration gaps, with "ad hoc" modifications to the models, can roughly match the P1 and P2 fluxes of the Crab pulsar at energies up to 400 GeV (e.g. Aleksić et al. 2011, 2012; Harding & Kalapotharakos 2015; Osmanov & Rieger 2017). Impressively, Harding & Kalapotharakos (2015) took into account the primarily accelerated electrons as well as the leptonic pairs generated by cascades, and Osmanov & Rieger (2017) considered magnetocentrifugal particle acceleration which is efficient close to the light cylinder. Proposed feasible alternatives include wind models, where pulsed γ-rays are due to synchrotron and/or IC radiation from relativistic electrons

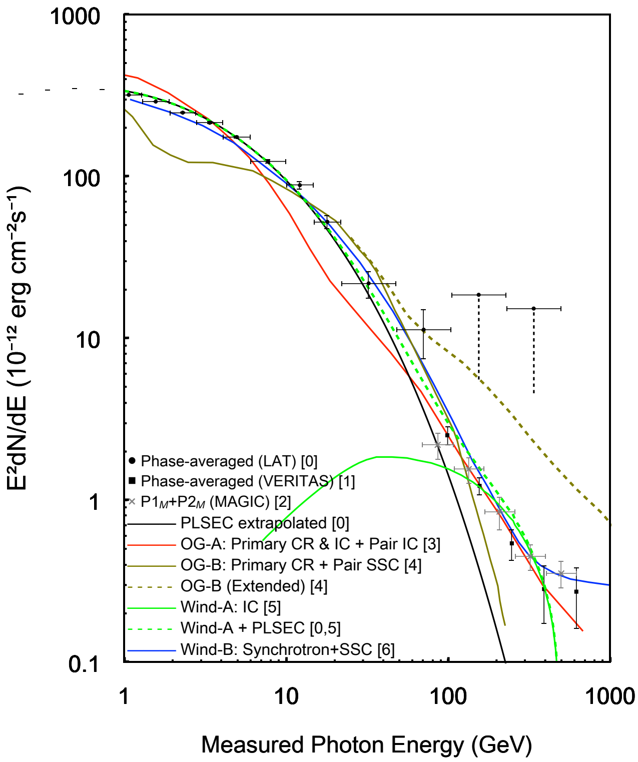

Fig. 10. Comparison of the observed full-phase spectrum with four theoretical models, namely OG-A, OG-B, Wind-A and Wind-B. Descriptions of points and lines are at the bottom-left corner. OG stands for "outer gap". CR stands for "curvature radiation". "Primary" means emission from primarily accelerated electrons. "Pair" means emission from leptonic pairs generated by cascades. "OG-B (Extended)" is the nominal OG-B model modified with a power-law extension to the cascade pair spectrum. References: [0] this work, [1] Nguyen & VERITAS Collaboration (2015), [2] Ansoldi et al. (2016), [3] Aleksić et al. (2012), [4] Harding & Kalapotharakos (2015), [5] Aharonian et al. (2012), [6] Mochol & Petri (2015).

outside the light cylinder. Aharonian et al. (2012) modelled the pulsed γ-ray emission of the instantaneously accelerated wind, while Arka & Dubus (2013) and Mochol & Petri (2015) modelled that of the wind current sheet.

The trends (a) and (d) of the Crab pulsar entail a decrease in pulse width with increasing energy, which is also detected for the Vela pulsar (DeCesar 2013; H. E. S. S. Collaboration 2018). Such a phenomenon is naturally explained by wind models as well. Besides, a harder spectrum at P2 compared to P1 (i.e. the trend (e)) is observed for both Crab and Vela pulsars (this work; DeCesar 2013; H. E. S. S. Collaboration 2018). This could be attributed to an anisotropy of the wind (Aharonian et al. 2012). Furthermore, wind models predict the bridge emission above 50 GeV as well, but a more complicated density profile of the wind is required to reproduce the observed flux proportion among the bridge and two peaks (Aharonian et al. 2012; Khangulyan et al. 2012).

For the phase-averaged spectrum in GeV–TeV, a schematic comparison of observational results with different theoretical predictions is shown in Fig. 10. Both of the two outer gap models, established by Aleksić et al. (2012) and Harding & Kalapotharakos (2015) respectively, fail to describe the spectral shape observed in 1–10 GeV. The sum of the freshly-accelerated wind's IC emission modelled by Aharonian et al. (2012) and the extrapolation of our PLSEC model can account for the γ-ray spectrum up to ~400 GeV. This implies that our PLSEC can be interpreted as a nominal component (i.e. synchro-curvature radiation from the outer gap and/or wind). On the other hand, Mochol & Petri (2015) established a model for a current sheet of striped wind which can, in absence of an outer-gap component, satisfactorily reproduce the observed flux and spectral shape from 1 GeV to 1 TeV. In this model, the transition from the synchrotron-dominated spectrum to the SSC-dominated spectrum occurs at ~300 GeV.

All in all, we propose a hybrid scenario where different acceleration sites account for pulsed γ-rays of the Crab pulsar at different phases and energies. Roughly speaking, the polar cap is responsible for the emission at and around the bridge below 10 GeV, the outer gap is responsible for <10 GeV emissions at other phases, and the wind is responsible for emissions above 10 GeV at any phase. In a more detailed modelling approach, one should carefully deal with the transition phases and transition energies among different emission components.

Acknowledgements. PKHY acknowledges the support of the DFG under the research grant HO 3305/4-1. PKHY gives sincere gratitude to D. Horns for useful discussions and for his encouragement regarding my submission as a single author. We greatly appreciate M. Kerr for providing the ephemeris of the Crab pulsar for phased analysis. We thank D. Carreto Fidalgo for his help in reconstructing Fig. 10. We thank the anonymous referee for very useful comments which helped to improve the manuscript.

References

Abdo, A. A., Ackermann, M., Ajello, M., et al. 2010, ApJ, 708, 1254
Abdo, A. A., Ajello, M., Allafort, A., et al. 2013, ApJS, 208, 17
Aharonian, F. A., & Bogovalov, S. V. 2003, New Astron., 8, 85
Aharonian, F. A., Bogovalov, S. V., & Khangulyan, D. 2012, Nature, 482, 507
Ahnen, M. L., Ansoldi, S., Antonelli, L. A., et al. 2016, A&A, 591, A138
Aleksić, J., Alvarez, E. A., Antonelli, L. A., et al. 2011, ApJ, 742, 43
Aleksić, J., Alvarez, E. A., Antonelli, L. A., et al. 2012, A&A, 540, A69
Aleksić, J., Ansoldi, S., Antonelli, L. A., et al. 2014, A&A, 565, L12
Ansoldi, S., Antonelli, L. A., Antoranz, P., et al. 2016, A&A, 585, A133
Arka, I., & Dubus, G. 2013, A&A, 550, A101
Arons, J. 1983, ApJ, 266, 215
Bogovalov, S. V., & Aharonian, F. A. 2000, MNRAS, 313, 504
Brambilla, G., Kalapotharakos, C., Harding, A. K., & Kazanas, D. 2015, ApJ, 804, 84
Buehler, R., Scargle, J. D., Blandford, R. D., et al. 2012, ApJ, 749, 26
Cheng, K. S., Ho, C., & Ruderman, M. 1986, ApJ, 300, 500
Cheng, K. S., Ruderman, M., & Zhang, L. 2000, ApJ, 537, 964
Daugherty, J. K., & Harding, A. K. 1982, ApJ, 252, 337
DeCesar, M. E. 2013, PhD thesis, University of Maryland, College Park, USA
de Jager, O. C. 2002, Bull. Astron. Soc. India, 30, 85
Dyks, J., & Rudak, B. 2003, ApJ, 598, 1201
Dyks, J., & Rudak, B. 2004, Adv. Space Res., 33, 581
Fermi-LAT Collaboration 2020, ApJS, 247, 33
Fierro, J. M., Michelson, P. F., Nolan, P. L., & Thompson, D. J. 1998, ApJ, 494, 734
Harding, A. K., & Kalapotharakos, C. 2015, ApJ, 811, 63
Harding, A. K., Tademaru, E., & Esposito, L. W. 1978, ApJ, 225, 226
Harding, A. K., Kalapotharakos, C., Barnard, M., & Venter, C. 2018, ApJ, 869, L18
H. E. S. S. Collaboration (Abdalla, H., et al.) 2018, A&A, 620, A66
Khangulyan, D., Aharonian, F. A., & Bogovalov, S. V. 2012, in AIP Conf. Ser., eds. F. A. Aharonian, W. Hofmann, & F. M. Rieger, 1505, 29
Lobanov, A. P., Horns, D., & Muxlow, T. W. B. 2011, A&A, 533, A10
Lyutikov, M. 2012, ApJ, 757, 88
Lyutikov, M., Otte, N., & McCann, A. 2012, ApJ, 754, 33
Mochol, I., & Petri, J. 2015, MNRAS, 449, L51
Muslimov, A. G., & Harding, A. K. 2004, ApJ, 606, 1143
Nguyen, T., & VERITAS Collaboration 2015, Int. Cosmic Ray Conf., 34, 828
Osmanov, Z., & Rieger, F. M. 2017, MNRAS, 464, 1347
Romani, R. W. 1996, ApJ, 470, 469
Romani, R. W., & Yadigaroglu, I. A. 1995, ApJ, 438, 314
Sturrock, P. A. 1971, ApJ, 164, 529
Takata, J., Shibata, S., Hirotani, K., & Chang, H. K. 2006, MNRAS, 366, 1310
Tang, A. P. S., Takata, J., Jia, J. J., & Cheng, K. S. 2008, ApJ, 676, 562
VERITAS Collaboration (Aliu, E., et al.) 2011, Science, 334, 69
Yeung, P. K. H., & Horns, D. 2020, A&A, 638, A147

Chapter 6

Summary

This summary is based on our refereed publications (Yeung and Horns, 2019, 2020; Yeung, 2020) and all appendices of this thesis. Our analyses on $\geq$9-year *Fermi*-LAT data and comparisons of our results with IACT observations provide insights into the high-energy properties of the Crab pulsar and its surrounding nebula. Despite the limitation of the angular resolution of gamma-ray telescopes, we can still distinguish the emission components originated from the Crab pulsar, synchrotron nebula and IC nebula, with phased analyses and spectral analyses.

The IC spectrum of the Crab Nebula is well characterised by a LP, or alternatively, a BKPL with a break at $\sim$10 GeV (Yeung and Horns, 2019; Yeung, 2020). The time-averaged synchrotron spectrum of the Crab Nebula, is well characterised by a simple PL (Yeung and Horns, 2020; Yeung, 2020). The phase-averaged γ-ray spectrum of the Crab pulsar below 10 GeV is well characterised by a PLSEC, while that above 10 GeV is well characterised by a simple PL (Yeung, 2020). All these general spectral properties we found are confirming previous studies (e.g., Buehler et al., 2012; Ansoldi et al., 2016).

The IC emission from the Crab Nebula is not shown to significantly vary with time (Yeung and Horns, 2019), while the nebular synchrotron emission is strongly variable (Yeung and Horns, 2020). For the first time, we found a low-flux state for the synchrotron nebula (Yeung and Horns, 2020). The apparent long-term variability of the Crab pulsar emission is also found to exceed the photon shot-noise fluctuation (see Appendix C.5), but the interpretation on this is beyond the scope of this thesis.

Different emission components of the Crab pulsar/nebula complex differ in a wide range of γ-ray dimensions. While the radius of the IC nebula is observed to be in a scale of 1 pc (Yeung and Horns, 2019), we infer the radius of the synchrotron nebula to be in a much smaller scale of 1 mpc (Yeung and Horns, 2020). In addition, we found an energy-dependent shrinking for the extension of the IC nebula (Yeung and Horns, 2019). We conservatively constrain the maximum radius of the pulsar emission region (i.e., the radius of the wind current sheet) to be within 100 light cylinder radii, corresponding to $\leq 5 \times 10^{-9}$ pc (Yeung, 2020).

We recommend a number of follow-up works which may help address some unsolved issues:

- In a theoretical modelling for the energy-dependent gamma-ray morphology of the IC nebula, one should take into account the spatial distribution of additional seed photon fields, which include the CMB and thermal dust emission, as well as the spatial variation of magnetic field (as suggested by my supervisor Prof. Dr. Dieter Horns in Yeung and Horns, 2019).
- In order to confirm the proposed scenario that the strongly variable synchrotron gamma-ray emission above 100 MeV mostly originates from the inner-knot feature, one should investigate the multi-wavelength emissions of the inner knot during the episodes of 60 MeV–600 MeV low-state we discovered (as suggested by my supervisor in Yeung and Horns, 2020).
- In a cosmic-ray phenomenological modelling of the Crab pulsar with the proposed multi-origin scenario, one should discreetly handle the transition phases and transition energies among different emission components (as suggested by me in Yeung, 2020).

Appendix A

10-year ephemeris of the Crab pulsar

As demonstrated in Figure A.1 (where data are taken from Jodrell Bank Crab Pulsar Timing Results – Monthly Ephemeris [1] (Lyne et al., 1993)), the Crab pulsar experienced two significant glitches over the first 10 years of *Fermi* LAT observations.

The ephemeris file of the Crab pulsar, which is provided entirely by Dr. Matthew Kerr and applied in Chapters 4 & 5 (including the published journal articles therein and all relevant supplementary information in Appendix C), is documented in the following. The two significant glitches mentioned above are handled in the 17th–33th lines. The recovery of the significant glitch occurring at around MJD 55875.7 is represented by an exponential decay function. For the significant glitch occurring at around MJD 58064.6, a sum of two exponential decay terms is used to characterise its recovery.

LISTING A.1: Ten-year ephemeris file of the Crab pulsar (Credit: Matthew Kerr).

```
1  PSRJ           J0534+2200
2  RAJ            05:34:31.94                    0.0040000000000000000
3  DECJ           +22:00:52.1                    0.0600000000000000000
4  F0             29.717146513347482695      1   0.00001483796566387845
5  F1             -3.7105154957188381331e-10     4.6591493867993752407e-17
6  F2             1.1740025595783781642e-20     1.1931513864842016248e-24
7  F3             -2.7156344475265872402e-30     9.2842295751118411255e-32
8  F4             2.5378552153445080892e-37     3.0897707060036237165e-39
9  F5             -2.9021465539003436322e-45     3.7281055998733954944e-47
10 PEPOCH         55555
11 POSEPOCH       50739
12 DMEPOCH        55107.807158553281624
13 DM             56.785579397589822356
```

[1] http://www.jb.man.ac.uk/~pulsar/crab.html

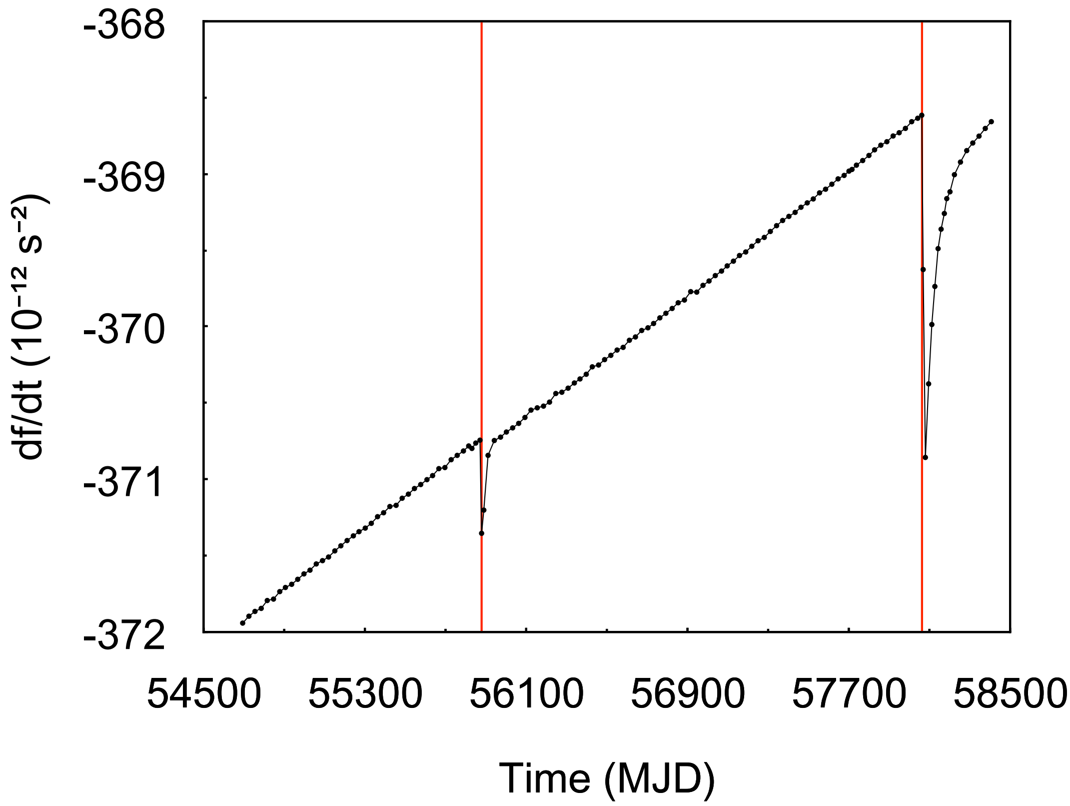

FIGURE A.1: Evolution of the first derivative of the pulse frequency with time. Data are taken from Jodrell Bank Crab Pulsar Timing Results – Monthly Ephemeris [1] (Lyne et al., 1993). Each red vertical line indicate the start time of a significant glitch.

```
DM1            0.031279168349770640344
PMRA           -11.8                          1.00000000000000000000
PMDEC          4.4000000000000000001          1.00000000000000000000
GLEP_1         55875.675439999999998
GLEP_2         58064.555000000000291
GLEP_3         58064.555000000000291
GLPH_1         -0.00079692415834803657272 1   0.03366318546658197963
GLPH_2         -0.033372379660628312941   1   0.01737810038938920887
GLF0_1         3.4548388483255881023e-07  1   0.00000001283467783323
GLF0_2         7.0410494039205605491e-06  1   0.00000001349126737436
GLF1_1         -6.3337507348244893567e-14 1   3.03586132123174760 27e-14
GLF1_2         -6.8578121376905331028e-13 1   2.5565136413857736 68e-14
GLF2_1         -3.8828274554217840431e-20 1   4.0206835143113523498e-21
GLF2_2         4.9506267321754335819e-21  1   6.519247699934179464e-21
GLF0D_1        1.1882349333150874004e-06
GLF0D_2        8.6594745977836545119e-06
GLF0D_3        -1.0887075492729632404e-06
GLTD_1         13.076679121972379 53          1.03691035284770594060
GLTD_2         41.587495306051431604
GLTD_3         3.7442242048016905632     1
START          54682.651407614282373     1
FINISH         58350.654628317407376     1
TRACK          -2
TZRMJD         56515.655265837475547
TZRFRQ         0
```

```
TZRSITE         coe
TRES            217.195
EPHVER          5
NE_SW           4
CLK             TT(TAI)
MODE 1
UNITS           TCB
TIMEEPH         IF99
DILATEFREQ      Y
PLANET_SHAPIRO  Y
T2CMETHOD       IAU2000B
NE_SW           4.000
CORRECT_TROPOSPHERE  N
EPHEM           DE405
NITS            1
NTOA            1670
CHI2R           6.7751 1600
WAVEEPOCH 55555
WAVE_OM 0.001512271442051 0
WAVE1 -560.38089977028 330.4498427849
WAVE2 -7.3609351376039 -156.72445678852
WAVE3 69.861081918028 6.9356127034083
WAVE4 -8.256247114493 36.566096045788
WAVE5 -21.619967876959 -7.8292976857678
WAVE6 6.5740233992801 -13.665507268783
WAVE7 8.8180768593695 5.4069428113674
WAVE8 -4.4631212609694 5.8067962738262
WAVE9 -3.8629127135184 -3.6058799199918
WAVE10 2.883685912102 -2.5356143764671
WAVE11 1.644494330769 2.3012996345358
WAVE12 -1.8057273826147 1.0462633547043
WAVE13 -0.63273788513268 -1.3978955815033
WAVE14 1.0716219416348 -0.35967265909919
WAVE15 0.18449814113365 0.80485430403135
WAVE16 -0.59264321243682 0.072675474122144
WAVE17 -0.0081165993335231 -0.42886136664969
WAVE18 0.30303881096321 0.024553062112197
WAVE19 -0.039343271678091 0.20733363084467
WAVE20 -0.13862976684371 -0.041675487843198
WAVE21 0.036948648476687 -0.089486661739812
WAVE22 0.055115073527742 0.030108738447348
WAVE23 -0.023044134836057 0.032787198168938
WAVE24 -0.018877161309826 -0.015687453738657
WAVE25 0.010035974778038 -0.0096988371601258
WAVE26 0.0048997247717184 0.0061532265520858
WAVE27 -0.0028510059031685 0.0024228276992088
WAVE28 -0.00089739697909656 -0.0015527890255167
WAVE29 0.00071801535011038 -0.0004385967007837
WAVE30 0.00016584189091433 0.00011930975713873
```

With the aid of the tempo2 Fermi plugin, we confirm the validity of this timing solution from 2008 August 4 to 2018 August 20 (see Figure A.2).

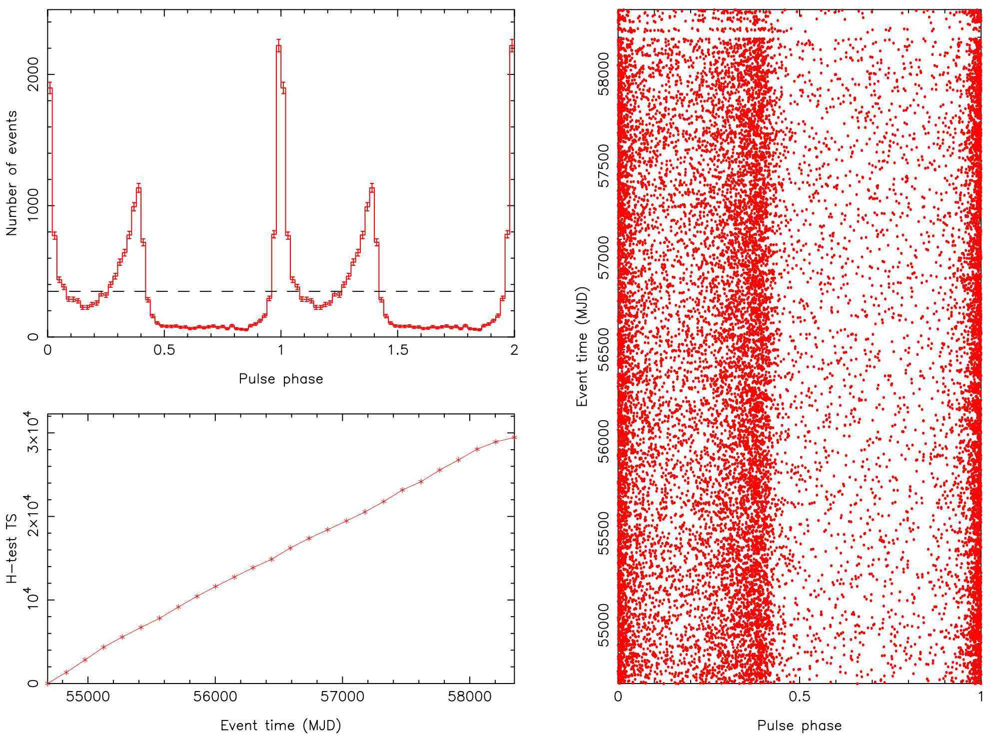

Figure A.2: Validation test of the ephemeris file with the tempo2 Fermi plugin. The 2–4 GeV data within 1° from the Crab pulsar is adopted for the folding analysis. (Top-left) Folded pulse profile. (Bottom-left) Evolution of H-test TS with time. (Right) Scatter plot of γ-ray events in time and pulse phase.

Appendix B

Program codes

B.1 Quantifying transitional timescales between low-flux and intermediate states

The following Python code, mainly developed by my supervisor Prof. Dr. Dieter Horns and then further modified by me, is used to quantify timescales of transitions between low-flux and intermediate states, which are reported in Section 3.4 of Yeung and Horns (2020).

My contributions to this code. After my supervisor established the overall algorithmic framework, I made my main contribution by adding four lines (the 40th–43th lines, which are followed by a comment in the 44th–45th lines) which scale the normalisations of two exponential terms, such that the fitted function is continuous throughout the whole fit range.

LISTING B.1: Python code used to quantify transitional timescales between low-flux and intermediate states of the Crab Nebula (composed initially and mainly by Dieter Horns; modified by Paul K. H. Yeung).

```
1  from pprint import pprint
2  import numpy as np
3  from iminuit import Minuit
4  import matplotlib.pyplot as plt
5  fermi=np.loadtxt("Low-d.txt")  # Load the segment of light-curve,
6  # which contains the dip at around MJD 58135, as an example
7  time= fermi[:,0]
8  flux  = fermi[:,1]
9  error = fermi[:,2]
10 constX=1.97727277430143  # Take the average of the preceding block
11 constY=1.38483395366142  # Take the average of the proceeding block
```

```

fp2 = dict(
    k_ingr = 0.3,  error_k_ingr = .2,
    k_egr  = 0.1,  error_k_egr  = .2,
    t_ingr   = 24,  error_t_ingr = .2,
    t_egr    = 55,  error_t_egr  = .2,
    low_flux = 0.0,  error_low_flux= .2,  fix_low_flux= True,
    X = constX,  error_X=0.2,  fix_X = True,
    Y = constY,  error_Y=0.2,  fix_Y = True,
    errordef=1
    )

# Fitted function: Sum of two exponentials, continuously joint with two constants

# Parameters in dictionary fp2:
# t_ingr: Ingress time [d]
# t_egr: Egress time [d]
# k_ingr: Exponential decay rate [d^-1]
# k_egr: Exponential rise rate [d^-1]
# low_flux: Constant flux during the dip; fixed at 0
# X: Constant flux before ingress; fixed at preceding-block average
# Y: Constant flux after egress; fixed at proceeding-block average

def fitfun(x,fitpar):
    y=np.copy(flux)
    ingres = np.where( (x>fitpar["t_ingr"]) & (x<fitpar["t_egr"]) )
    y=np.where(x<=fitpar["t_ingr"],fitpar["X"],-1.)
    y=np.where(x>=fitpar["t_egr"],fitpar["Y"],y)
    factorD=np.exp((fitpar["t_ingr"]-fitpar["t_egr"])*fitpar["k_egr"])
    factorH=np.exp((fitpar["t_ingr"]-fitpar["t_egr"])*fitpar["k_ingr"])
    peakA=(fitpar["X"]-fitpar["Y"]*factorD)/(1-factorH*factorD)
    peakB=(fitpar["X"]*factorH-fitpar["Y"])/(factorH*factorD-1)
# Last four lines scale the normalisations of two exponential terms,
# such that the fitted function is continuous throughout the whole fit range.
    A = peakA *np.exp(  (fitpar["t_ingr"]-x[ingres])*fitpar["k_ingr"])
    B = peakB *np.exp( -(fitpar["t_egr"] -x[ingres])*fitpar["k_egr"])
    C = fitpar["low_flux"]
    y[ingres] = A+B+C
    return (ingres,A,B,y)

def lsq(k_ingr,k_egr,t_ingr,t_egr,low_flux,X,Y):
    fitpar=fp2
    fitpar["X"]=X
    fitpar["Y"]=Y
    fitpar["low_flux"]=low_flux
    fitpar["k_ingr"]=k_ingr
    fitpar["k_egr"]=k_egr
    fitpar["t_ingr"]=t_ingr
    fitpar["t_egr"]=t_egr
    chisq = (flux - fitfun(time-time[0],fitpar)[-1])**2/error**2
    return np.sum(chisq)

m = Minuit(lsq, **fp2,print_level=2)
m.migrad()

```

```
print(m.minos())
print(m.fval)
print(m.values)
print(m.errors)

# Halving time is calculated as ln(2)/k_ingr
# Doubling time is calculated as ln(2)/k_egr
```

B.2 Cross-calibration fit to the joint spectra of *Fermi* LAT & MAGIC

The following Python code, where the algorithm is initially written by my supervisor Prof. Dr. Dieter Horns and then finalised by me, is used to fit the PLSF model to the joint spectra of *Fermi* LAT & MAGIC for the pulse phases $\mathrm{P1}_M$ & $\mathrm{P2}_M$. The results are reported in Section 3.4 of Yeung (2020).

My contributions to this code. My supervisor established the initial algorithmic framework which, in each operation, can only perform a spectral fitting to spectral data for one phase interval. Then, I modified his version so that the finalised version in the following can perform a simultaneous fitting for two phase intervals such that their solutions share the same scaling factor "*escale*".

Listing B.2: Python code used to fit the PLSF model to the joint spectra of *Fermi* LAT & MAGIC for the pulse phases $\mathrm{P1}_M$ & $\mathrm{P2}_M$ of the Crab pulsar (composed initially and mainly by Dieter Horns; modified by Paul K. H. Yeung).

```
from pprint import pprint
import numpy as np
from iminuit import Minuit
import matplotlib.pyplot as plt

def f(x,n0,g):
    return n0 * (x/50.)**(-g)

fermiY=np.loadtxt("P2_fermi.dat")
magicY=np.loadtxt("P2_magic.dat")
efermiY= fermiY[:,0]
dndefermiY  = fermiY[:,1]
dndeufermiY = fermiY[:,2]
emagicY = magicY[:,0]
dndemagicY = magicY[:,1]
dndeumagicY = magicY[:,2]

fermiX=np.loadtxt("P1_fermi.dat")
magicX=np.loadtxt("P1_magic.dat")
efermiX= fermiX[:,0]
```

```
dndefermiX  = fermiX[:,1]
dndeufermiX = fermiX[:,2]
emagicX = magicX[:,0]
dndemagicX = magicX[:,1]
dndeumagicX = magicX[:,2]

def lsq(n0,g,escale,N0,G):
    chi2_fermiY = sum( (dndefermiY - f(efermiY,n0,g))**2./dndeufermiY**2)
    chi2_magicY = sum( (dndemagicY - f(emagicY*escale,n0,g))**2./dndeumagicY**2)
    chi2_fermiX = sum( (dndefermiX - f(efermiX,N0,G))**2./dndeufermiX**2)
    chi2_magicX = sum( (dndemagicX - f(emagicX*escale,N0,G))**2./dndeumagicX**2)
    return chi2_fermiY+chi2_magicY+chi2_fermiX+chi2_magicX
# The sum of Chi-Squares for two instruments and two phases
# is going to be minimised.

m = Minuit(lsq,errordef=1,n0=4.837E-03,g=3.41,escale=1.22,N0=4.837E-03,G=3.41,
error_n0=1e-4,error_g=0.01,error_escale=0.01,error_N0=1e-4,error_G=0.01)
m.migrad()

print(m.minos())
print(m.fval)  # Total Chi-Square
print(len(efermiX)+len(emagicX)+len(efermiY)+len(emagicY)-5)  # No. of d.o.f.
print(m.values)
print(m.errors)
```

Appendix C

Supplementary information

This appendix provides supplementary information which is based on our refereed publications (Yeung and Horns, 2019, 2020; Yeung, 2020). These are my own ideas to implement the further calculations, analyses and cross-checks presented below (except the moving-average analysis in Appendix C.2 where the initial idea was introduced by my supervisor Prof. Dr. Dieter Horns). The new results in this appendix have not yet been published somewhere else.

C.1 Apparent variability of the nebular IC flux due to shot-noise

In addition to Section 3.2 of Yeung and Horns (2019), I found that the total Crab emission (i.e., the sum of pulsar and nebula components) in 5–500 GeV has an average number of photons of ≈36 in a 15-day interval. Based on this statistic, the fractional root-mean-square (RMS) variability of the total Crab flux for shot-noise only is expected to be 16.7%. On the other hand, the fractional RMS variability of the total Crab flux computed from the observed light-curve (Figure 4 of Yeung and Horns, 2019) is only 17.2%. Hence, a large portion of the apparent variability presented in the light-curve could be attributed to the photon shot-noise fluctuation. In turn, it is further justified that no time-based screening of data is required for measurements of the IC nebula's extensions.

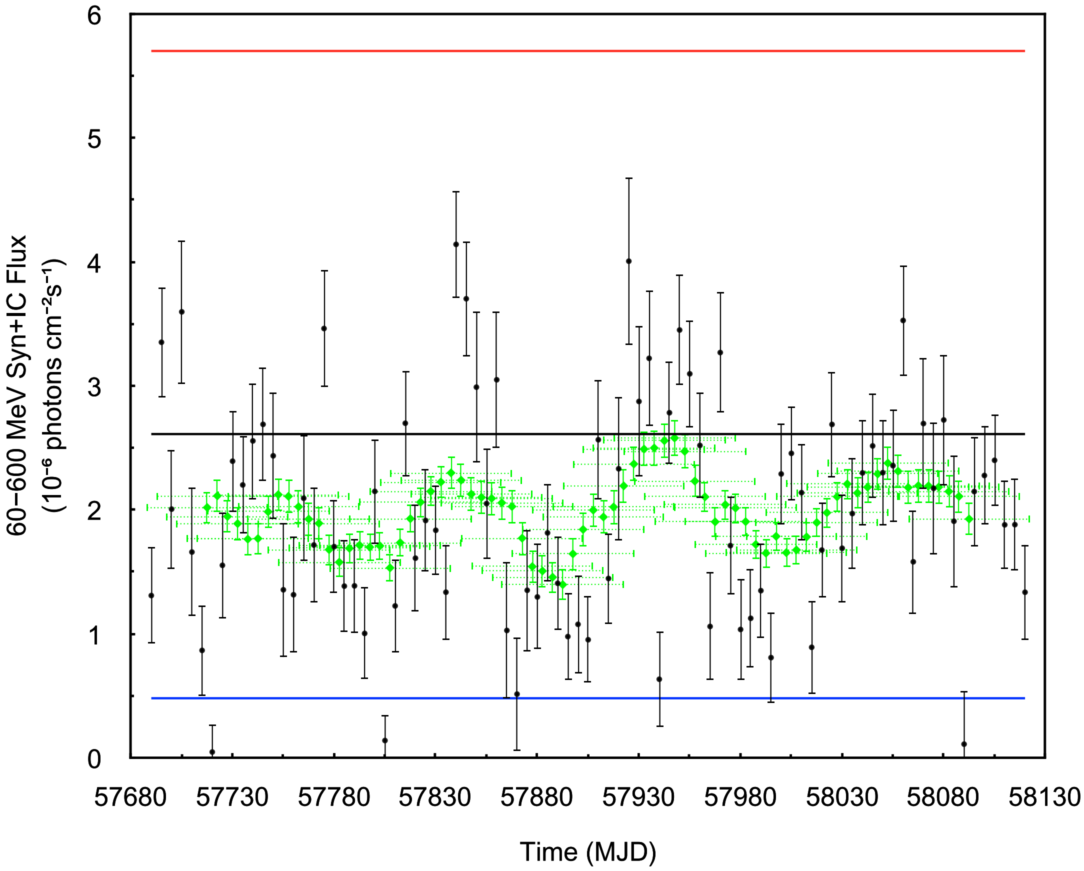

FIGURE C.1: Segment of the Crab Nebula's Fermi-LAT light-curve for the moving-average analysis. The 5-day bins (taken from Figure 2 of Yeung and Horns, 2020) are plotted as black circles, and the 60-day moving averages are plotted as green diamonds. The black horizontal line indicates the intermediate-state average flux, while the red and blue lines respectively indicate the thresholds of the "high" and "low" states we define in our Yeung and Horns (2020).

C.2 Moving-average analysis on a segment of the light-curve for the Synchrotron Nebula

It is interesting to investigate the temporal behaviour of the Crab Nebula's 60–600 MeV Fermi-LAT flux at a longer timescale as well as the variability within the intermediate state defined in our Yeung and Horns (2020). Therefore, we select a segment of the light-curve (Figure 2 of our Yeung and Horns (2020)) for a moving-average analysis (Figure C.1). This segment only covers the time range from 2016 October 26 to 2018 January 4, where all bins are well within the high-state threshold and 3 out of 87 bins fall below the low-state threshold. We smooth out the flux data of 5-day bins by creating a constantly updated average flux, which is taken as an unweighted mean over 60 days (12 bins). Whenever we compute a successive average flux, the oldest bin drops out of the calculation and a new bin is included.

As shown in Figure C.1, the 60-day average flux also varies from time to time. The maximum-minimum ratio of the moving average is 1.85. This ratio is significantly exceeding 1 even when the systematic uncertainties stemming from energy dispersion and the Galactic diffuse model are taken into account (more specifically, the maximum is larger than the minimum by 3.4 times the quadratic sum of their statistical and systematic uncertainties). This investigation indicates that the longer-term (2-month) flux of the synchrotron nebula in 60–600 MeV is significantly varying as well as the shorter-term (5-day) flux, and the so-called intermediate state cannot be treated as a steady baseline state. It is therefore important to stress the idea that the γ-ray temporal behaviour is a continuum of variability instead of abrupt switchings among different flux states.

C.3 Further cross-check for the low-state spectrum of the Crab Nebula

In Section 3.6 of Yeung and Horns (2020), we had cross-checked the low-state spectrum of the Crab Nebula by two different methods of grouping the so-called low-state bins. What is more, I did a further cross-check by excluding the poor-resolution 60–130 MeV data for more robust results. The obtained PL model is overlaid in Figure C.2 of this thesis, which is modified from Figure 6 of Yeung and Horns (2020). This further supports the resemblance between the Crab spectrum during the low-flux state and the extrapolation of the IC spectrum.

C.4 Supplementary information to cross-calibration fits for Crab pulsar spectra

In Section 3.4 of Yeung (2020), I determined from the PLSF-fitting result that Γ for $P2_M$ is lower than that for $P1_M$ by $\sim 2.1\sigma$. However, the calculation of this significance omitted the covariance of the Γ values for $P1_M$ and $P2_M$ (I recall that the spectral data for $P1_M$ and $P2_M$ are fit together such that their solutions share the same scaling factor ϵ). After taking into account this covariance which is determined to be 0.010, I found that Γ for $P2_M$ is actually lower than that for $P1_M$ by 0.35 ± 0.08, which corresponds to $\sim 4.2\sigma$. This strengthens the argument that the flux ratio of P1 to P2 still decreases with photon energy even above 10 GeV.

Furthermore, taking the statistical uncertainties into consideration, the ϵ values obtained for MAGIC and VERITAS (both $\sim$1.22) are essentially consistent with the estimated systematic uncertainties of around 15% on energy scales of IACT telescopes under the

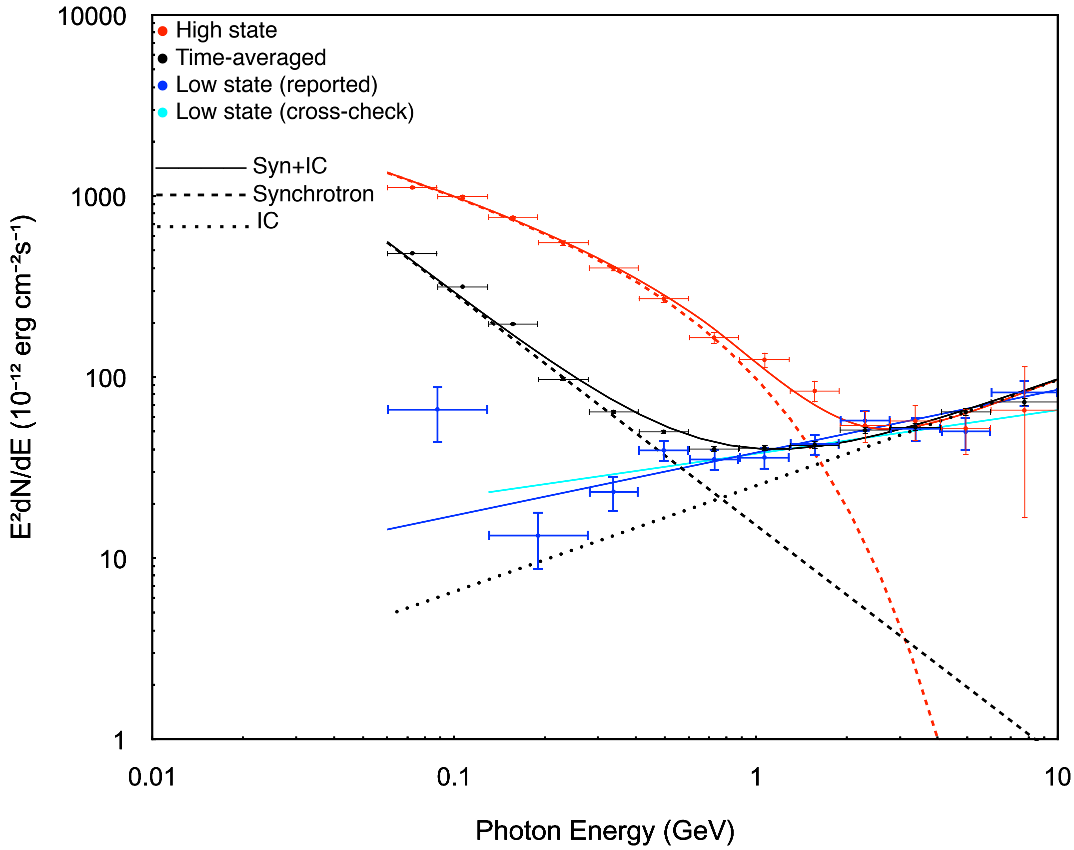

FIGURE C.2: Spectral energy distributions (SED) of the Crab Nebula for different flux states (modified from Figure 6 of Yeung and Horns, 2020). We determine the IC component (the dotted line) with the time-averaged spectrum (in black). We define the spectra of the high and low states (in red and blue respectively) based on the 60 MeV-600 MeV light-curve of the Crab Nebula (Figure 2 of Yeung and Horns (2020)). The total Syn+IC emission is represented by the solid lines and the binned spectra, while the synchrotron component is represented by the dashed lines. The combined Syn+IC spectrum during the low state is plotted as a single PL component (solid blue line). An alternative low-state spectrum for cross-checking is overlaid as the solid cyan line. The only difference between this figure and the original one is in the minimum energy cut applied to the fitting of the alternative low-state spectrum (solid cyan line).

perfect atmospheric conditions (e.g., Aharonian et al., 2006; Aleksić et al., 2016). This further confirms the physical reasonableness of my fitting results.

C.5 Long-term temporal behaviour of the pulsed γ-ray emission

In Section 3.3 of Yeung and Horns (2020), we mentioned that the 60–600 MeV flux of the Crab pulsar alone at the first pulse peak was observed to vary with time, and the apparent variability exceeds the expected shot-noise fluctuation by a factor of ~ 3. Here,

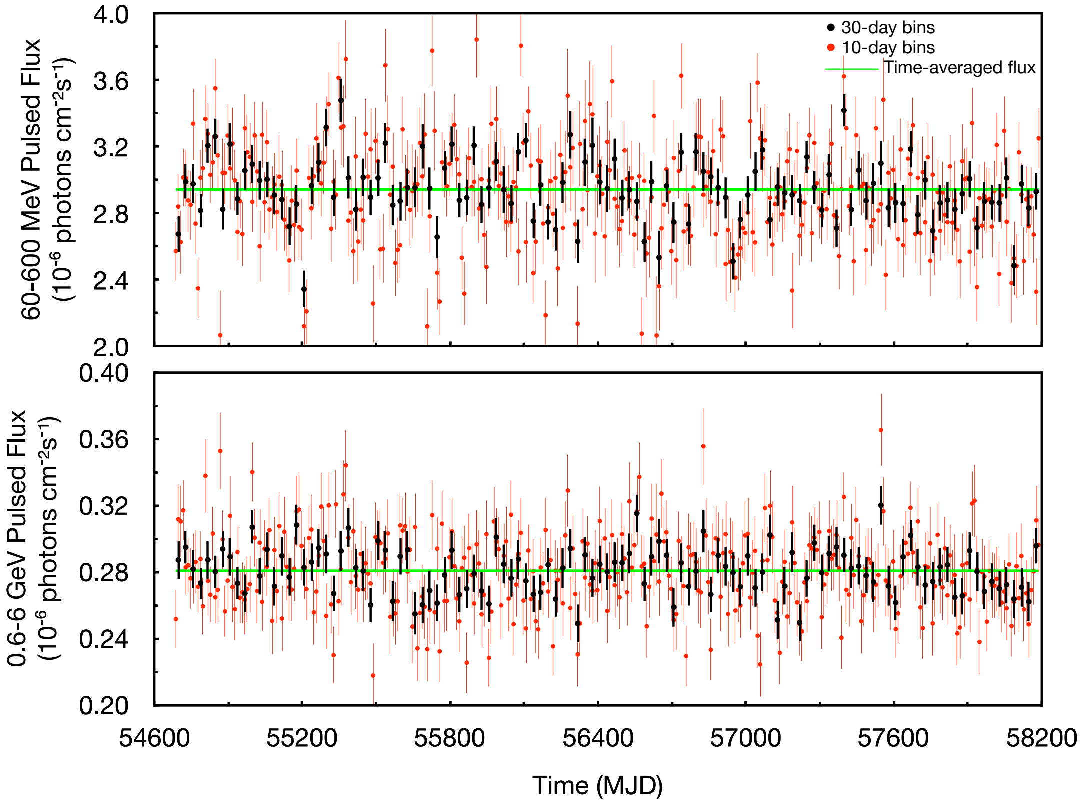

FIGURE C.3: LAT long-term light-curves of pulsed γ-rays from the Crab pulsar, in 60–600 MeV (top) and 0.6–6 GeV (bottom) respectively. On each panel, the light-curves with bin sizes of 30 days and 10 days are plotted in black and red respectively, and the green horizontal line indicates the time-averaged flux. The relevant statistics are presented in Table C.1.

we conduct further investigations into the long-term temporal behaviour of the pulsed γ-rays from the Crab, by taking the full-phase data into account.

We investigate the variabilities of fluxes in 60–600 MeV and 0.6–6 GeV respectively. For each energy band, we adopt bin sizes of 30 days and 10 days respectively. For each bin, we determine the full-phase flux F_{full} and OFF flux F_{OFF} of the entire Crab pulsar/nebula complex, where the OFF phase interval is defined in the same way as in Yeung (2020). Then, the pulsed flux of the Crab pulsar alone is computed as $F_{full} - F_{OFF}/0.3$. The four observed light-curves of the Crab pulsar are plotted in Figure C.3, and the relevant statistics are presented in Table C.1.

The observed apparent variability of each light-curve is a combined effect of the photon shot-noise fluctuations, the systematic errors, and the intrinsic variability of the Crab pulsar. Therefore, the variability unexplained by the shot-noise (i.e., the quadratic subtraction of the fractional RMS variability of the expected shot-noise from that of the observed light-curve) can be regarded as an upper limit on the actual variability amplitude of the pulsar flux.

TABLE C.1: Statistics for long-term light-curves of the Crab pulsar's pulsed γ-ray emission.

Energy Band	60–600 MeV		0.6–6 GeV	
Bin Size (days)	30	10	30	10
Photons/Bins [a]	9704	3235	924	308
$(\chi^2/dof)_{const}$ [b]	298/116	801/350	175/116	517/350
α_{LC} [c]	6.4%	10.7%	4.9%	8.5%
α_{SN} [d]	1.0%	1.8%	3.3%	5.7%
$\sqrt{\alpha_{LC}^2 - \alpha_{SN}^2}$ [e]	6.3%	10.5%	3.7%	6.3%

[a] The average number of photons detected from the Crab pulsar per bin.
[b] $\chi^2/d.o.f.$ yielded by fitting a constant-value function to the observed light-curve.
[c] The fractional RMS variability amplitude of the observed light-curve.
[d] The fractional RMS variability amplitude of the expected shot-noise.
[e] The observed fractional RMS variability which is unexplained by the shot-noise.

Appendix D

Acronyms

LAT	Large Area Telescope
PSF	Point spread function
H.E.S.S.	High Energy Stereoscopic System
SED	Spectral energy distribution
VHE	Very high energy
SSC	Synchrotron-self-Compton
IC	Inverse Compton
Syn+IC	Synchrotron plus inverse-Compton
VERITAS	Very Energetic Radiation Imaging Telescope Array System
PWN	Pulsar wind nebula
SNR	Supernova remnant
MAGIC	Major Atmospheric Gamma Imaging Cherenkov Telescopes
CMB	Cosmic microwave background
TS	Test-statistic
FWHM	Full width at half maximum
IACT	Imaging Atmospheric Cherenkov Technique
EAS	Extensive Air Shower
PSD	Power-spectral density
PDF	Probability density function
DFT	Discrete Fourier-transformation
PL	Power-law
PLEC	Power-law with exponential cutoff
PLSEC	Power-law with super-/sub-exponential cutoff

PLSF Power-law with a scaling factor
on photon energies measured by IACT instruments

BKPL Broken-power-law

LP Log-parabola

RMS Root-mean-square

ROI Region of interest

IRF Instrument response function

ACD Anti-Coincidence Detector

List of Figures

1.1 Mosaic image of the Crab Nebula taken by the Hubble Space Telescope . 2
1.2 Formation process of a PWN 3
1.3 Schematic illustration of a pair-conversion gamma-ray telescope 4
1.4 The three-dimensional structure of *Fermi* LAT 5
1.5 Schematic illustration of gamma-ray air showers 6
1.6 Previous SED of the Crab Nebula from soft γ-ray to VHE γ-ray 8
1.7 The gamma-ray extension sizes of the Crab IC nebula measured by H.E.S.S. under various observation conditions and analysis chains, in comparison with the upper limits on extension sizes measured for two active galactic nuclei 9
1.8 Time-evolution of the photon flux from the Crab integrated above 100 MeV during the 2011 April Crab flare 10
1.9 The structure of a pulsar magnetosphere within a light cylinder 11
1.10 Previous *Fermi* LAT phaseograms of the Crab pulsar 13

2.1 Spatial and spectral resolutions of LAT 16
2.2 Flow of operation of *Fermi* Science Tools 18
2.3 All-sky map (top), legend (middle) and distribution of 4FGL sources projected on the Galactic plane (bottom) 20
2.4 Detector Response Matrix internally translated by Fermitools from the energy dispersion response functions of the IRFs 21

A.1 Evolution of the first derivative of the pulse frequency with time 62
A.2 Validation test of the ephemeris file with the tempo2 Fermi plugin 64

C.1 Segment of the Crab Nebula's Fermi-LAT light-curve for the moving-average analysis 70
C.2 SED of the Crab Nebula for different flux states 72
C.3 LAT long-term light-curves of pulsed γ-rays from the Crab pulsar 73

List of Tables

C.1 Statistics for long-term light-curves of the Crab pulsar's pulsed γ-ray emission. 74

Bibliography

A. A. Abdo, M. Ackermann, M. Ajello, W. B. Atwood, M. Axelsson, L. Baldini, J. Ballet, G. Barbiellini, M. G. Baring, D. Bastieri, K. Bechtol, R. Bellazzini, B. Berenji, R. D. Bland ford, E. D. Bloom, E. Bonamente, A. W. Borgland , J. Bregeon, A. Brez, M. Brigida, P. Bruel, T. H. Burnett, G. A. Caliandro, R. A. Cameron, F. Camilo, P. A. Caraveo, J. M. Casand jian, C. Cecchi, Ö. Çelik, A. Chekhtman, C. C. Cheung, J. Chiang, S. Ciprini, R. Claus, I. Cognard, J. Cohen-Tanugi, L. R. Cominsky, J. Conrad, C. D. Dermer, A. de Angelis, A. de Luca, F. de Palma, S. W. Digel, E. do Couto e. Silva, P. S. Drell, R. Dubois, D. Dumora, C. Espinoza, C. Farnier, C. Favuzzi, S. J. Fegan, E. C. Ferrara, W. B. Focke, M. Frailis, P. C. C. Freire, Y. Fukazawa, S. Funk, P. Fusco, F. Gargano, D. Gasparrini, N. Gehrels, S. Germani, G. Giavitto, B. Giebels, N. Giglietto, F. Giordano, T. Glanzman, G. Godfrey, I. A. Grenier, M. H. Grondin, J. E. Grove, L. Guillemot, S. Guiriec, Y. Hanabata, A. K. Harding, M. Hayashida, E. Hays, R. E. Hughes, G. Jóhannesson, A. S. Johnson, R. P. Johnson, T. J. Johnson, W. N. Johnson, S. Johnston, T. Kamae, H. Katagiri, J. Kataoka, N. Kawai, M. Kerr, J. Knödlseder, M. L. Kocian, M. Kramer, F. Kuehn, M. Kuss, J. Land e, L. Latronico, S. H. Lee, M. Lemoine-Goumard, F. Longo, F. Loparco, B. Lott, M. N. Lovellette, P. Lubrano, A. G. Lyne, A. Makeev, M. Marelli, M. N. Mazziotta, J. E. McEnery, C. Meurer, P. F. Michelson, W. Mitthumsiri, T. Mizuno, A. A. Moiseev, C. Monte, M. E. Monzani, E. Moretti, A. Morselli, I. V. Moskalenko, S. Murgia, T. Nakamori, P. L. Nolan, J. P. Norris, A. Noutsos, E. Nuss, T. Ohsugi, N. Omodei, E. Orland o, J. F. Ormes, M. Ozaki, D. Paneque, J. H. Panetta, D. Parent, V. Pelassa, M. Pepe, M. Pesce-Rollins, M. Pierbattista, F. Piron, T. A. Porter, S. Rainò, R. Rando, P. S. Ray, M. Razzano, A. Reimer, O. Reimer, T. Reposeur, S. Ritz, L. S. Rochester, A. Y. Rodriguez, R. W. Romani, M. Roth, F. Ryde, H. F. W. Sadrozinski, D. Sanchez, A. Sander, P. M. Saz Parkinson, J. D. Scargle, C. Sgrò, E. J. Siskind, D. A. Smith, P. D. Smith, G. Spand re, P. Spinelli, B. W. Stappers, M. S. Strickman, D. J. Suson, H. Tajima, H. Takahashi, T. Tanaka, J. B. Thayer, J. G. Thayer, G. Theureau, D. J. Thompson, S. E. Thorsett, L. Tibaldo, D. F. Torres,

G. Tosti, A. Tramacere, Y. Uchiyama, T. L. Usher, A. Van Etten, V. Vasileiou, N. Vilchez, V. Vitale, A. P. Waite, E. Wallace, P. Wang, K. Watters, P. Weltevrede, B. L. Winer, K. S. Wood, T. Ylinen, and M. Ziegler. Fermi Large Area Telescope Observations of the Crab Pulsar And Nebula. *Astrophys. J.*, 708(2):1254–1267, January 2010. doi: 10.1088/0004-637X/708/2/1254.

A. A. Abdo, M. Ackermann, M. Ajello, A. Allafort, L. Baldini, J. Ballet, G. Barbiellini, D. Bastieri, K. Bechtol, R. Bellazzini, B. Berenji, R. D. Blandford, E. D. Bloom, E. Bonamente, A. W. Borgland, A. Bouvier, T. J. Brandt, J. Bregeon, A. Brez, M. Brigida, P. Bruel, R. Buehler, S. Buson, G. A. Caliandro, R. A. Cameron, A. Cannon, P. A. Caraveo, J. M. Casandjian, Ö. Çelik, E. Charles, A. Chekhtman, C. C. Cheung, J. Chiang, S. Ciprini, R. Claus, J. Cohen-Tanugi, L. Costamante, S. Cutini, F. D'Ammando, C. D. Dermer, A. de Angelis, A. de Luca, F. de Palma, S. W. Digel, E. do Couto e Silva, P. S. Drell, A. Drlica-Wagner, R. Dubois, D. Dumora, C. Favuzzi, S. J. Fegan, E. C. Ferrara, W. B. Focke, P. Fortin, M. Frailis, Y. Fukazawa, S. Funk, P. Fusco, F. Gargano, D. Gasparrini, N. Gehrels, S. Germani, N. Giglietto, F. Giordano, M. Giroletti, T. Glanzman, G. Godfrey, I. A. Grenier, M.-H. Grondin, J. E. Grove, S. Guiriec, D. Hadasch, Y. Hanabata, A. K. Harding, K. Hayashi, M. Hayashida, E. Hays, D. Horan, R. Itoh, G. Jóhannesson, A. S. Johnson, T. J. Johnson, D. Khangulyan, T. Kamae, H. Katagiri, J. Kataoka, M. Kerr, J. Knödlseder, M. Kuss, J. Lande, L. Latronico, S.-H. Lee, M. Lemoine-Goumard, F. Longo, F. Loparco, P. Lubrano, G. M. Madejski, A. Makeev, M. Marelli, M. N. Mazziotta, J. E. McEnery, P. F. Michelson, W. Mitthumsiri, T. Mizuno, A. A. Moiseev, C. Monte, M. E. Monzani, A. Morselli, I. V. Moskalenko, S. Murgia, T. Nakamori, M. Naumann-Godo, P. L. Nolan, J. P. Norris, E. Nuss, T. Ohsugi, A. Okumura, N. Omodei, J. F. Ormes, M. Ozaki, D. Paneque, D. Parent, V. Pelassa, M. Pepe, M. Pesce-Rollins, M. Pierbattista, F. Piron, T. A. Porter, S. Rainò, R. Rando, P. S. Ray, M. Razzano, A. Reimer, O. Reimer, T. Reposeur, S. Ritz, R. W. Romani, H. F.-W. Sadrozinski, D. Sanchez, P. M. S. Parkinson, J. D. Scargle, T. L. Schalk, C. Sgrò, E. J. Siskind, P. D. Smith, G. Spandre, P. Spinelli, M. S. Strickman, D. J. Suson, H. Takahashi, T. Takahashi, T. Tanaka, J. B. Thayer, D. J. Thompson, L. Tibaldo, D. F. Torres, G. Tosti, A. Tramacere, E. Troja, Y. Uchiyama, J. Vandenbroucke, V. Vasileiou, G. Vianello, V. Vitale, P. Wang, K. S. Wood, Z. Yang, and M. Ziegler. Gamma-Ray Flares from the Crab Nebula. *Science*, 331:739, February 2011. doi: 10.1126/science.1199705.

A. A. Abdo, M. Ajello, A. Allafort, L. Baldini, J. Ballet, G. Barbiellini, M. G. Baring, D. Bastieri, A. Belfiore, R. Bellazzini, B. Bhattacharyya, E. Bissaldi, E. D. Bloom, E. Bonamente, E. Bottacini, T. J. Brandt, J. Bregeon, M. Brigida, P. Bruel, R. Buehler, M. Burgay, T. H. Burnett, G. Busetto, S. Buson, G. A. Caliandro,

R. A. Cameron, F. Camilo, P. A. Caraveo, J. M. Casandjian, C. Cecchi, . elik, E. Charles, S. Chaty, R. C. G. Chaves, A. Chekhtman, A. W. Chen, J. Chiang, G. Chiaro, S. Ciprini, R. Claus, I. Cognard, J. Cohen-Tanugi, L. R. Cominsky, J. Conrad, S. Cutini, F. D'Ammando, A. de Angelis, M. E. DeCesar, A. De Luca, P. R. den Hartog, F. de Palma, C. D. Dermer, G. Desvignes, S. W. Digel, L. Di Venere, P. S. Drell, A. Drlica-Wagner, R. Dubois, D. Dumora, C. M. Espinoza, L. Falletti, C. Favuzzi, E. C. Ferrara, W. B. Focke, A. Franckowiak, P. C. C. Freire, S. Funk, P. Fusco, F. Gargano, D. Gasparrini, S. Germani, N. Giglietto, P. Giommi, F. Giordano, M. Giroletti, T. Glanzman, G. Godfrey, E. V. Gotthelf, I. A. Grenier, M.-H. Grondin, J. E. Grove, L. Guillemot, S. Guiriec, D. Hadasch, Y. Hanabata, A. K. Harding, M. Hayashida, E. Hays, J. Hessels, J. Hewitt, A. B. Hill, D. Horan, X. Hou, R. E. Hughes, M. S. Jackson, G. H. Janssen, T. Jogler, G. Jhannesson, R. P. Johnson, A. S. Johnson, T. J. Johnson, W. N. Johnson, S. Johnston, T. Kamae, J. Kataoka, M. Keith, M. Kerr, J. Kndlseder, M. Kramer, M. Kuss, J. Lande, S. Larsson, L. Latronico, M. Lemoine-Goumard, F. Longo, F. Loparco, M. N. Lovellette, P. Lubrano, A. G. Lyne, R. N. Manchester, M. Marelli, F. Massaro, M. Mayer, M. N. Mazziotta, J. E. McEnery, M. A. McLaughlin, J. Mehault, P. F. Michelson, R. P. Mignani, W. Mitthumsiri, T. Mizuno, A. A. Moiseev, M. E. Monzani, A. Morselli, I. V. Moskalenko, S. Murgia, T. Nakamori, R. Nemmen, E. Nuss, M. Ohno, T. Ohsugi, M. Orienti, E. Orlando, J. F. Ormes, D. Paneque, J. H. Panetta, D. Parent, J. S. Perkins, M. Pesce-Rollins, M. Pierbattista, F. Piron, G. Pivato, H. J. Pletsch, T. A. Porter, A. Possenti, S. Rain, R. Rando, S. M. Ransom, P. S. Ray, M. Razzano, N. Rea, A. Reimer, O. Reimer, N. Renault, T. Reposeur, S. Ritz, R. W. Romani, M. Roth, R. Rousseau, J. Roy, J. Ruan, A. Sartori, P. M. Saz Parkinson, J. D. Scargle, A. Schulz, C. Sgr, R. Shannon, E. J. Siskind, D. A. Smith, G. Spandre, P. Spinelli, B. W. Stappers, A. W. Strong, D. J. Suson, H. Takahashi, J. G. Thayer, J. B. Thayer, G. Theureau, D. J. Thompson, S. E. Thorsett, L. Tibaldo, O. Tibolla, M. Tinivella, D. F. Torres, G. Tosti, E. Troja, Y. Uchiyama, T. L. Usher, J. Vandenbroucke, V. Vasileiou, C. Venter, G. Vianello, V. Vitale, N. Wang, P. Weltevrede, B. L. Winer, M. T. Wolff, D. L. Wood, K. S. Wood, M. Wood, and Z. Yang. The Second Fermi Large Area Telescope Catalog of Gamma-Ray Pulsars. *The Astrophysical Journal Supplement Series*, 208:17, October 2013. ISSN 0067-0049. doi: 10.1088/0067-0049/208/2/17. URL http://adsabs.harvard.edu/abs/2013ApJS..208...17A.

M. Ackermann, M. Ajello, A. Albert, A. Allafort, W. B. Atwood, M. Axelsson, L. Baldini, J. Ballet, G. Barbiellini, D. Bastieri, K. Bechtol, R. Bellazzini, E. Bissaldi, R. D. Blandford, E. D. Bloom, J. R. Bogart, E. Bonamente, A. W. Borgland, E. Bottacini, A. Bouvier, T. J. Brandt, J. Bregeon, M. Brigida, P. Bruel, R. Buehler, T. H. Burnett, S. Buson, G. A. Caliandro, R. A. Cameron, P. A. Caraveo, J. M. Casandjian,

E. Cavazzuti, C. Cecchi, . elik, E. Charles, R. C. G. Chaves, A. Chekhtman, C. C. Cheung, J. Chiang, S. Ciprini, R. Claus, J. Cohen-Tanugi, J. Conrad, R. Corbet, S. Cutini, F. D'Ammando, D. S. Davis, A. de Angelis, M. DeKlotz, F. de Palma, C. D. Dermer, S. W. Digel, E. do Couto e. Silva, P. S. Drell, A. Drlica-Wagner, R. Dubois, C. Favuzzi, S. J. Fegan, E. C. Ferrara, W. B. Focke, P. Fortin, Y. Fukazawa, S. Funk, P. Fusco, F. Gargano, D. Gasparrini, N. Gehrels, B. Giebels, N. Giglietto, F. Giordano, M. Giroletti, T. Glanzman, G. Godfrey, I. A. Grenier, J. E. Grove, S. Guiriec, D. Hadasch, M. Hayashida, E. Hays, D. Horan, X. Hou, R. E. Hughes, M. S. Jackson, T. Jogler, G. Jhannesson, R. P. Johnson, T. J. Johnson, W. N. Johnson, T. Kamae, H. Katagiri, J. Kataoka, M. Kerr, J. Kndlseder, M. Kuss, J. Lande, S. Larsson, L. Latronico, C. Lavalley, M. Lemoine-Goumard, F. Longo, F. Loparco, B. Lott, M. N. Lovellette, P. Lubrano, M. N. Mazziotta, W. McConville, J. E. McEnery, J. Mehault, P. F. Michelson, W. Mitthumsiri, T. Mizuno, A. A. Moiseev, C. Monte, M. E. Monzani, A. Morselli, I. V. Moskalenko, S. Murgia, M. Naumann-Godo, R. Nemmen, S. Nishino, J. P. Norris, E. Nuss, M. Ohno, T. Ohsugi, A. Okumura, N. Omodei, M. Orienti, E. Orlando, J. F. Ormes, D. Paneque, J. H. Panetta, J. S. Perkins, M. Pesce-Rollins, M. Pierbattista, F. Piron, G. Pivato, T. A. Porter, J. L. Racusin, S. Rain, R. Rando, M. Razzano, S. Razzaque, A. Reimer, O. Reimer, T. Reposeur, L. C. Reyes, S. Ritz, L. S. Rochester, C. Romoli, M. Roth, H. F.-W. Sadrozinski, D. A. Sanchez, P. M. Saz Parkinson, C. Sbarra, J. D. Scargle, C. Sgr, J. Siegal-Gaskins, E. J. Siskind, G. Spandre, P. Spinelli, T. E. Stephens, D. J. Suson, H. Tajima, H. Takahashi, T. Tanaka, J. G. Thayer, J. B. Thayer, D. J. Thompson, L. Tibaldo, M. Tinivella, G. Tosti, E. Troja, T. L. Usher, J. Vandenbroucke, B. Van Klaveren, V. Vasileiou, G. Vianello, V. Vitale, A. P. Waite, E. Wallace, B. L. Winer, D. L. Wood, K. S. Wood, M. Wood, Z. Yang, and S. Zimmer. The Fermi Large Area Telescope on Orbit: Event Classification, Instrument Response Functions, and Calibration. *The Astrophysical Journal Supplement Series*, 203:4, November 2012a. ISSN 0067-0049. doi: 10.1088/0067-0049/203/1/4. URL http://adsabs.harvard.edu/abs/2012ApJS..203....4A.

M. Ackermann, M. Ajello, A. Allafort, W. B. Atwood, M. Axelsson, L. Baldini, G. Barbiellini, D. Bastieri, K. Bechtol, R. Bellazzini, B. Berenji, E. D. Bloom, E. Bonamente, A. W. Borgland , A. Bouvier, J. Bregeon, A. Brez, M. Brigida, P. Bruel, R. Buehler, S. Buson, G. A. Caliandro, R. A. Cameron, P. A. Caraveo, J. M. Casand jian, C. Cecchi, E. Charles, A. Chekhtman, J. Chiang, S. Ciprini, R. Claus, J. Cohen-Tanugi, S. Cutini, F. de Palma, C. D. Dermer, S. W. Digel, E. Do Couto E Silva, P. S. Drell, A. Drlica-Wagner, R. Dubois, T. Enoto, L. Falletti, C. Favuzzi, S. J. Fegan, W. B. Focke, P. Fortin, Y. Fukazawa, S. Funk, P. Fusco, F. Gargano, N. Gehrels, S. Germani, N. Giglietto, F. Giordano, M. Giroletti, T. Glanzman, G. Godfrey, I. A.

Grenier, J. E. Grove, S. Guiriec, D. Hadasch, M. Hayashida, E. Hays, R. E. Hughes, G. Jóhannesson, A. S. Johnson, T. J. Johnson, T. Kamae, H. Katagiri, J. Kataoka, J. Knödlseder, M. Kuss, J. Lande, L. Latronico, S. H. Lee, F. Longo, F. Loparco, M. N. Lovellette, P. Lubrano, G. M. Madejski, M. N. Mazziotta, J. E. McEnery, P. F. Michelson, T. Mizuno, A. A. Moiseev, C. Monte, M. E. Monzani, A. Morselli, I. V. Moskalenko, S. Murgia, T. Nakamori, M. Naumann-Godo, P. L. Nolan, J. P. Norris, E. Nuss, T. Ohsugi, A. Okumura, N. Omodei, E. Orlando, J. F. Ormes, M. Ozaki, D. Paneque, J. H. Panetta, D. Parent, M. Pesce-Rollins, M. Pierbattista, F. Piron, S. Rainò, R. Rando, M. Razzano, A. Reimer, O. Reimer, T. Reposeur, S. Ritz, L. S. Rochester, C. Sgrò, E. J. Siskind, P. D. Smith, G. Spand re, P. Spinelli, D. J. Suson, H. Takahashi, T. Tanaka, J. G. Thayer, J. B. Thayer, D. J. Thompson, L. Tibaldo, G. Tosti, E. Troja, T. L. Usher, J. Vandenbroucke, V. Vasileiou, G. Vianello, N. Vilchez, V. Vitale, A. P. Waite, P. Wang, B. L. Winer, K. S. Wood, Z. Yang, and S. Zimmer. In-flight measurement of the absolute energy scale of the Fermi Large Area Telescope. *Astroparticle Physics*, 35(6):346–353, January 2012b. doi: 10.1016/j.astropartphys.2011.10.007.

F. Aharonian, A. G. Akhperjanian, A. R. Bazer-Bachi, M. Beilicke, W. Benbow, D. Berge, K. Bernlöhr, C. Boisson, O. Bolz, V. Borrel, I. Braun, F. Breitling, A. M. Brown, R. Bühler, I. Büsching, S. Carrigan, P. M. Chadwick, L. M. Chounet, R. Cornils, L. Costamante, B. Degrange, H. J. Dickinson, A. Djannati-Ataï, L. O'C. Drury, G. Dubus, K. Egberts, D. Emmanoulopoulos, P. Espigat, F. Feinstein, E. Ferrero, A. Fiasson, G. Fontaine, Seb. Funk, S. Funk, Y. A. Gallant, B. Giebels, J. F. Glicenstein, P. Goret, C. Hadjichristidis, D. Hauser, M. Hauser, G. Heinzelmann, G. Henri, G. Hermann, J. A. Hinton, W. Hofmann, M. Holleran, D. Horns, A. Jacholkowska, O. C. de Jager, B. Khélifi, Nu. Komin, A. Konopelko, K. Kosack, I. J. Latham, R. Le Gallou, A. Lemière, M. Lemoine-Goumard, T. Lohse, J. M. Martin, O. Martineau-Huynh, A. Marcowith, C. Masterson, T. J. L. McComb, M. de Naurois, D. Nedbal, S. J. Nolan, A. Noutsos, K. J. Orford, J. L. Osborne, M. Ouchrif, M. Panter, G. Pelletier, S. Pita, G. Pühlhofer, M. Punch, B. C. Raubenheimer, M. Raue, S. M. Rayner, A. Reimer, O. Reimer, J. Ripken, L. Rob, L. Rolland , G. Rowell, V. Sahakian, L. Saugé, S. Schlenker, R. Schlickeiser, U. Schwanke, H. Sol, D. Spangler, F. Spanier, R. Steenkamp, C. Stegmann, G. Superina, J. P. Tavernet, R. Terrier, C. G. Théoret, M. Tluczykont, C. van Eldik, G. Vasileiadis, C. Venter, P. Vincent, H. J. Völk, S. J. Wagner, and M. Ward. Observations of the Crab nebula with HESS. *Astr. Astrophys.*, 457(3):899–915, October 2006. doi: 10.1051/0004-6361:20065351.

F. A. Aharonian and S. V. Bogovalov. Exploring physics of rotation powered pulsars with sub-10 GeV imaging atmospheric Cherenkov telescopes. *New Astronomy* , 8(2): 85–103, February 2003. doi: 10.1016/S1384-1076(02)00200-2.

F. A. Aharonian, S. V. Bogovalov, and D. Khangulyan. Abrupt acceleration of a 'cold' ultrarelativistic wind from the Crab pulsar. *Nature*, 482(7386):507–509, February 2012. doi: 10.1038/nature10793.

Aharonian et al. The Crab Nebula and Pulsar between 500 GeV and 80 TeV: Observations with the HEGRA stereoscopic air Cherenkov telescopes. *The Astrophysical Journal*, 614(2):897–913, October 2004. ISSN 0004-637X, 1538-4357. doi: 10.1086/423931. URL http://arxiv.org/abs/astro-ph/0407118. arXiv: astro-ph/0407118.

J. Aleksić, E. A. Alvarez, L. A. Antonelli, P. Antoranz, M. Asensio, M. Backes, J. A. Barrio, D. Bastieri, J. Becerra González, W. Bednarek, A. Berdyugin, K. Berger, E. Bernardini, A. Biland, O. Blanch, R. K. Bock, A. Boller, G. Bonnoli, D. Borla Tridon, I. Braun, T. Bretz, A. Cañellas, E. Carmona, A. Carosi, P. Colin, E. Colombo, J. L. Contreras, J. Cortina, L. Cossio, S. Covino, F. Dazzi, A. de Angelis, G. de Caneva, E. de Cea Del Pozo, B. de Lotto, C. Delgado Mendez, A. Diago Ortega, M. Doert, A. Domínguez, D. Dominis Prester, D. Dorner, M. Doro, D. Eisenacher, D. Elsaesser, D. Ferenc, M. V. Fonseca, L. Font, C. Fruck, R. J. García López, M. Garczarczyk, D. Garrido, G. Giavitto, N. Godinović, D. Hadasch, D. Häfner, A. Herrero, D. Hildebrand, D. Höhne-Mönch, J. Hose, D. Hrupec, T. Jogler, H. Kellermann, S. Klepser, T. Krähenbühl, J. Krause, J. Kushida, A. La Barbera, D. Lelas, E. Leonardo, N. Lewand owska, E. Lindfors, S. Lombardi, M. López, A. López-Oramas, E. Lorenz, M. Makariev, G. Maneva, N. Mankuzhiyil, K. Mannheim, L. Maraschi, M. Mariotti, M. Martínez, D. Mazin, M. Meucci, J. M. Miranda, R. Mirzoyan, J. Moldón, A. Moralejo, P. Munar-Adrover, A. Niedzwiecki, D. Nieto, K. Nilsson, N. Nowak, R. Orito, D. Paneque, R. Paoletti, S. Pardo, J. M. Paredes, S. Partini, M. A. Perez-Torres, M. Persic, L. Peruzzo, M. Pilia, J. Pochon, F. Prada, P. G. Prada Moroni, E. Prandini, I. Puerto Gimenez, I. Puljak, I. Reichardt, R. Reinthal, W. Rhode, M. Ribó, J. Rico, S. Rügamer, A. Saggion, K. Saito, T. Y. Saito, M. Salvati, K. Satalecka, V. Scalzotto, V. Scapin, C. Schultz, T. Schweizer, M. Shayduk, S. N. Shore, A. Sillanpää, J. Sitarek, I. Šnidarić, D. Sobczynska, F. Spanier, S. Spiro, V. Stamatescu, A. Stamerra, B. Steinke, J. Storz, N. Strah, T. Surić, L. Takalo, H. Takami, F. Tavecchio, P. Temnikov, T. Terzić, D. Tescaro, M. Teshima, O. Tibolla, D. F. Torres, A. Treves, M. Uellenbeck, H. Vankov, P. Vogler, R. M. Wagner, Q. Weitzel, V. Zabalza, F. Zandanel, R. Zanin, and K. Hirotani. Phase-resolved energy spectra of the Crab pulsar in the range of 50-400 GeV measured with the MAGIC telescopes. *Astr. Astrophys.*, 540:A69, April 2012. doi: 10.1051/0004-6361/201118166.

J. Aleksić, S. Ansoldi, L. A. Antonelli, P. Antoranz, A. Babic, P. Bangale, U. Barres de Almeida, J. A. Barrio, J. Becerra González, W. Bednarek, E. Bernardini, B. Biasuzzi, A. Biland, O. Blanch, S. Bonnefoy, G. Bonnoli, F. Borracci, T. Bretz,

E. Carmona, A. Carosi, P. Colin, E. Colombo, J. L. Contreras, J. Cortina, S. Covino, P. Da Vela, F. Dazzi, A. De Angelis, G. De Caneva, B. De Lotto, C. Delgado Mendez, M. Doert, D. Dominis Prester, D. Dorner, M. Doro, S. Einecke, D. Eisenacher, D. Elsaesser, E. Farina, D. Ferenc, D. Fidalgo, M. V. Fonseca, L. Font, K. Frantzen, C. Fruck, R. J. García López, M. Garczarczyk, D. Garrido Terrats, M. Gaug, N. Godinović, A. González Muñoz, S. R. Gozzini, D. Hadasch, M. Hayashida, J. Herrera, A. Herrero, D. Hildebrand , K. Hirotani, J. Hose, D. Hrupec, W. Idec, V. Kadenius, H. Kellermann, K. Kodani, Y. Konno, J. Krause, H. Kubo, J. Kushida, A. La Barbera, D. Lelas, N. Lewandowska, E. Lindfors, S. Lombardi, M. López, R. López-Coto, A. López-Oramas, E. Lorenz, I. Lozano, M. Makariev, K. Mallot, G. Maneva, N. Mankuzhiyil, K. Mannheim, L. Maraschi, B. Marcote, M. Mariotti, M. Martínez, D. Mazin, U. Menzel, J. M. Mirand a, R. Mirzoyan, A. Moralejo, P. Munar-Adrover, D. Nakajima, A. Niedzwiecki, K. Nilsson, K. Nishijima, K. Noda, N. Nowak, R. Orito, A. Overkemping, S. Paiano, M. Palatiello, D. Paneque, R. Paoletti, J. M. Paredes, X. Paredes-Fortuny, S. Partini, M. Persic, P. G. Prada Moroni, E. Prandini, S. Preziuso, I. Puljak, R. Reinthal, W. Rhode, M. Ribó, J. Rico, J. Rodriguez Garcia, S. Rügamer, A. Saggion, T. Y. Saito, K. Saito, K. Satalecka, V. Scalzotto, V. Scapin, C. Schultz, T. Schweizer, S. N. Shore, A. Sillanpää, J. Sitarek, I. Snidaric, D. Sobczynska, F. Spanier, V. Stamatescu, A. Stamerra, T. Steinbring, J. Storz, M. Strzys, S. Sun, T. Surić, L. Takalo, H. Takami, F. Tavecchio, P. Temnikov, T. Terzić, D. Tescaro, M. Teshima, J. Thaele, O. Tibolla, D. F. Torres, T. Toyama, A. Treves, M. Uellenbeck, P. Vogler, R. M. Wagner, and R. Zanin. Detection of bridge emission above 50 GeV from the Crab pulsar with the MAGIC telescopes. *Astr. Astrophys.*, 565:L12, May 2014. doi: 10.1051/0004-6361/201423664.

J. Aleksić, S. Ansoldi, L. A. Antonelli, P. Antoranz, A. Babic, P. Bangale, M. Barceló, J. A. Barrio, J. Becerra González, W. Bednarek, E. Bernardini, B. Biasuzzi, A. Biland, M. Bitossi, O. Blanch, S. Bonnefoy, G. Bonnoli, F. Borracci, T. Bretz, E. Carmona, A. Carosi, R. Cecchi, P. Colin, E. Colombo, J. L. Contreras, D. Corti, J. Cortina, S. Covino, P. Da Vela, F. Dazzi, A. De Angelis, G. De Caneva, B. De Lotto, E. de Oña Wilhelmi, C. Delgado Mendez, A. Dettlaff, D. Dominis Prester, D. Dorner, M. Doro, S. Einecke, D. Eisenacher, D. Elsaesser, D. Fidalgo, D. Fink, M. V. Fonseca, L. Font, K. Frantzen, C. Fruck, D. Galindo, R. J. García López, M. Garczarczyk, D. Garrido Terrats, M. Gaug, G. Giavitto, N. Godinović, A. González Muñoz, S. R. Gozzini, W. Haberer, D. Hadasch, Y. Hanabata, M. Hayashida, J. Herrera, D. Hildebrand , J. Hose, D. Hrupec, W. Idec, J. M. Illa, V. Kadenius, H. Kellermann, M. L. Knoetig, K. Kodani, Y. Konno, J. Krause, H. Kubo, J. Kushida, A. La Barbera, D. Lelas, J. L. Lemus, N. Lewandowska, E. Lindfors, S. Lombardi, F. Longo, M. López, R. López-Coto, A. López-Oramas, A. Lorca, E. Lorenz, I. Lozano, M. Makariev, K. Mallot,

G. Maneva, N. Mankuzhiyil, K. Mannheim, L. Maraschi, B. Marcote, M. Mariotti, M. Martínez, D. Mazin, U. Menzel, J. M. Miranda, R. Mirzoyan, A. Moralejo, P. Munar-Adrover, D. Nakajima, M. Negrello, V. Neustroev, A. Niedzwiecki, K. Nilsson, K. Nishijima, K. Noda, R. Orito, A. Overkemping, S. Paiano, M. Palatiello, D. Paneque, R. Paoletti, J. M. Paredes, X. Paredes-Fortuny, M. Persic, J. Poutanen, P. G. Prada Moroni, E. Prandini, I. Puljak, R. Reinthal, W. Rhode, M. Ribó, J. Rico, J. Rodriguez Garcia, S. Rügamer, T. Saito, K. Saito, K. Satalecka, V. Scalzotto, V. Scapin, C. Schultz, J. Schlammer, S. Schmidl, T. Schweizer, S. N. Shore, A. Sillanpää, J. Sitarek, I. Snidaric, D. Sobczynska, F. Spanier, A. Stamerra, T. Steinbring, J. Storz, M. Strzys, L. Takalo, H. Takami, F. Tavecchio, L. A. Tejedor, P. Temnikov, T. Terzić, D. Tescaro, M. Teshima, J. Thaele, O. Tibolla, D. F. Torres, T. Toyama, A. Treves, P. Vogler, H. Wetteskind, M. Will, and R. Zanin. The major upgrade of the MAGIC telescopes, Part II: A performance study using observations of the Crab Nebula. *Astroparticle Physics*, 72:76–94, January 2016. doi: 10.1016/j.astropartphys.2015.02.005.

S. Ansoldi, L. A. Antonelli, P. Antoranz, A. Babic, P. Bangale, U. Barres de Almeida, J. A. Barrio, J. Becerra Gonzlez, W. Bednarek, E. Bernardini, B. Biasuzzi, A. Biland, O. Blanch, S. Bonnefoy, G. Bonnoli, F. Borracci, T. Bretz, E. Carmona, A. Carosi, P. Colin, E. Colombo, J. L. Contreras, J. Cortina, S. Covino, P. Da Vela, F. Dazzi, A. De Angelis, G. De Caneva, B. De Lotto, E. de Oa Wilhelmi, C. Delgado Mendez, F. Di Pierro, D. Dominis Prester, D. Dorner, M. Doro, S. Einecke, D. Eisenacher Glawion, D. Elsaesser, A. Fernndez-Barral, D. Fidalgo, M. V. Fonseca, L. Font, K. Frantzen, C. Fruck, D. Galindo, R. J. Garca Lpez, M. Garczarczyk, D. Garrido Terrats, M. Gaug, N. Godinovi, A. Gonzlez Muoz, S. R. Gozzini, Y. Hanabata, M. Hayashida, J. Herrera, K. Hirotani, J. Hose, D. Hrupec, G. Hughes, W. Idec, H. Kellermann, M. L. Knoetig, K. Kodani, Y. Konno, J. Krause, H. Kubo, J. Kushida, A. La Barbera, D. Lelas, N. Lewandowska, E. Lindfors, S. Lombardi, F. Longo, M. Lpez, R. Lpez-Coto, A. Lpez-Oramas, E. Lorenz, M. Makariev, K. Mallot, G. Maneva, K. Mannheim, L. Maraschi, B. Marcote, M. Mariotti, M. Martnez, D. Mazin, U. Menzel, J. M. Miranda, R. Mirzoyan, A. Moralejo, P. Munar-Adrover, D. Nakajima, V. Neustroev, A. Niedzwiecki, M. Nevas Rosillo, K. Nilsson, K. Nishijima, K. Noda, R. Orito, A. Overkemping, S. Paiano, M. Palatiello, D. Paneque, R. Paoletti, J. M. Paredes, X. Paredes-Fortuny, M. Persic, J. Poutanen, P. G. Prada Moroni, E. Prandini, I. Puljak, R. Reinthal, W. Rhode, M. Rib, J. Rico, J. Rodriguez Garcia, T. Saito, K. Saito, K. Satalecka, V. Scalzotto, V. Scapin, C. Schultz, T. Schweizer, S. N. Shore, A. Sillanp, J. Sitarek, I. Snidaric, D. Sobczynska, A. Stamerra, T. Steinbring, M. Strzys, L. Takalo, H. Takami, F. Tavecchio, P. Temnikov, T. Terzi, D. Tescaro, M. Teshima, J. Thaele, D. F. Torres, T. Toyama,

A. Treves, J. Ward, M. Will, and R. Zanin. Teraelectronvolt pulsed emission from the Crab Pulsar detected by MAGIC. *Astronomy and Astrophysics*, 585: A133, January 2016. ISSN 0004-6361. doi: 10.1051/0004-6361/201526853. URL http://adsabs.harvard.edu/abs/2016A%26A...585A.133A.

I. Arka and G. Dubus. Pulsed high-energy γ-rays from thermal populations in the current sheets of pulsar winds. *Astr. Astrophys.*, 550:A101, February 2013. doi: 10.1051/0004-6361/201220110.

A. M. Atoyan and F. A. Aharonian. On the mechanisms of gamma radiation in the Crab Nebula. *Monthly Notices of the Royal Astronomical Society*, 278:525–541, January 1996. ISSN 0035-8711. doi: 10.1093/mnras/278.2.525. URL http://adsabs.harvard.edu/abs/1996MNRAS.278..525A.

W. Atwood, A. Albert, L. Baldini, M. Tinivella, J. Bregeon, M. Pesce-Rollins, C. Sgrò, P. Bruel, E. Charles, A. Drlica-Wagner, A. Franckowiak, T. Jogler, L. Rochester, T. Usher, M. Wood, J. Cohen-Tanugi, and S. Zimmer. Pass 8: Toward the Full Realization of the Fermi-LAT Scientific Potential. *arXiv e-prints*, art. arXiv:1303.3514, March 2013.

Konrad Bernlöhr. Impact of atmospheric parameters on the atmospheric Cherenkov technique*. *Astroparticle Physics*, 12(4):255–268, January 2000. doi: 10.1016/S0927-6505(99)00093-6.

M. F. Bietenholz and R. L. Nugent. New expansion rate measurements of the Crab nebula in radio and optical. *Monthly Notices of the Royal Astronomical Society*, 454: 2416–2422, December 2015. ISSN 0035-8711. doi: 10.1093/mnras/stv2112. URL http://adsabs.harvard.edu/abs/2015MNRAS.454.2416B.

S. V. Bogovalov and F. A. Aharonian. Very-high-energy gamma radiation associated with the unshocked wind of the Crab pulsar. *Month. Not. Roy. Astr. Soc.*, 313(3): 504–514, April 2000. doi: 10.1046/j.1365-8711.2000.03250.x.

R. Buehler, J. D. Scargle, R. D. Blandford, L. Baldini, M. G. Baring, A. Belfiore, E. Charles, J. Chiang, F. D'Ammando, C. D. Dermer, S. Funk, J. E. Grove, A. K. Harding, E. Hays, M. Kerr, F. Massaro, M. N. Mazziotta, R. W. Romani, P. M. Saz Parkinson, A. F. Tennant, and M. C. Weisskopf. Gamma-Ray Activity in the Crab Nebula: The Exceptional Flare of 2011 April. *The Astrophysical Journal*, 749: 26, April 2012. ISSN 0004-637X. doi: 10.1088/0004-637X/749/1/26. URL http://adsabs.harvard.edu/abs/2012ApJ...749...26B.

R. Bühler and R. Blandford. The surprising Crab pulsar and its nebula: a review. *Reports on Progress in Physics*, 77(6):066901, 2014. ISSN 0034-4885. doi: 10.1088/0034-4885/77/6/066901. URL http://stacks.iop.org/0034-4885/77/i=6/a=066901.

K. S. Cheng, C. Ho, and M. Ruderman. Energetic Radiation from Rapidly Spinning Pulsars. I. Outer Magnetosphere Gaps. *Astrophys. J.*, 300:500, January 1986. doi: 10.1086/163829.

S D Connolly. A Python Code for the Emmanoulopoulos et al. [arXiv:1305.0304] Light Curve Simulation Algorithm. *arXiv e-prints*, art. arXiv:1503.06676, Mar 2015.

O. C. de Jager and A. K. Harding. The expected high-energy to ultra-high-energy gamma-ray spectrum of the Crab Nebula. *The Astrophysical Journal*, 396:161–172, September 1992. ISSN 0004-637X. doi: 10.1086/171706. URL http://adsabs.harvard.edu/abs/1992ApJ...396..161D.

Megan Elizabeth DeCesar. *Using Fermi Large Area Telescope Observations to Constrain the Emission and Field Geometries of Young Gamma-ray Pulsars and to Guide Millisecond Pulsar Searches*. PhD thesis, University of Maryland, College Park, January 2013.

G. Dubner, G. Castelletti, O. Kargaltsev, G. G. Pavlov, M. Bietenholz, and A. Talavera. Morphological Properties of the Crab Nebula: A Detailed Multiwavelength Study Based on New VLA, HST, Chandra, and XMM-Newton Images. *The Astrophysical Journal*, 840:82, May 2017. ISSN 0004-637X. doi: 10.3847/1538-4357/aa6983. URL http://adsabs.harvard.edu/abs/2017ApJ...840...82D.

D. Emmanoulopoulos, I. M. McHardy, and I. E. Papadakis. Generating artificial light curves: revisited and updated. *Month. Not. Roy. Astr. Soc.*, 433:907–927, August 2013. doi: 10.1093/mnras/stt764.

Fermi-LAT Collaboration and Jonathan Biteau. Search for Spatial Extension in High-Latitude Sources Detected by the Fermi Large Area Telescope. *ArXiv e-prints*, 1804:arXiv:1804.08035, April 2018. URL http://adsabs.harvard.edu/abs/2018arXiv180408035F.

J. M. Fierro, P. F. Michelson, P. L. Nolan, and D. J. Thompson. Phase-resolved Studies of the High-Energy Gamma-Ray Emission from the Crab, Geminga, and VELA Pulsars. *Astrophys. J.*, 494(2):734–746, February 1998. doi: 10.1086/305219.

F. Fraschetti and M. Pohl. Particle acceleration model for the broad-band baseline spectrum of the Crab nebula. *Monthly Notices of the Royal Astronomical Society*, 471:4856–4864, November 2017. ISSN 0035-8711. doi: 10.1093/mnras/stx1833. URL http://adsabs.harvard.edu/abs/2017MNRAS.471.4856F.

Bryan M. Gaensler and Patrick O. Slane. The Evolution and Structure of Pulsar Wind Nebulae. *Annu. Rev. Astron. Astrophys.*, 44(1):17–47, September 2006. doi: 10.1146/annurev.astro.44.051905.092528.

James E. Gunn and Jeremiah P. Ostriker. On the Motion and Radiation of Charged Particles in Strong Electromagnetic Waves. I. Motion in Plane and Spherical Waves. *The Astrophysical Journal*, 165:523, May 1971. ISSN 0004-637X. doi: 10.1086/150919. URL http://adsabs.harvard.edu/abs/1971ApJ...165..523G.

H. E. S. S. Collaboration. Resolving the Crab pulsar wind nebula at teraelectronvolt energies. *Nature Astronomy*, 4:167–173, February 2020. doi: 10.1038/s41550-019-0910-0.

Alice K. Harding and Constantinos Kalapotharakos. Synchrotron Self-Compton Emission from the Crab and Other Pulsars. *Astrophys. J.*, 811(1):63, September 2015. doi: 10.1088/0004-637X/811/1/63.

Alice K. Harding, Constantinos Kalapotharakos, Monica Barnard, and Christo Venter. Multi-TeV Emission from the Vela Pulsar. *Astrophys. J. Letters*, 869(1):L18, December 2018. doi: 10.3847/2041-8213/aaf3b2.

J. Jeff Hester. The Crab Nebula: An Astrophysical Chimera. *Annual Review of Astronomy and Astrophysics*, 46:127–155, September 2008. ISSN 0066-4146. doi: 10.1146/annurev.astro.45.051806.110608. URL http://adsabs.harvard.edu/abs/2008ARA%26A..46..127H.

A. M. Hillas, C. W. Akerlof, S. D. Biller, J. H. Buckley, D. A. Carter-Lewis, M. Catanese, M. F. Cawley, D. J. Fegan, J. P. Finley, J. A. Gaidos, F. Krennrich, R. C. Lamb, M. J. Lang, G. Mohanty, M. Punch, P. T. Reynolds, A. J. Rodgers, H. J. Rose, A. C. Rovero, M. S. Schubnell, G. H. Sembroski, G. Vacanti, T. C. Weekes, M. West, and J. Zweerink. The Spectrum of Teravolt Gamma Rays from the Crab Nebula. *The Astrophysical Journal*, 503:744–759, August 1998. ISSN 0004-637X. doi: 10.1086/306005. URL http://adsabs.harvard.edu/abs/1998ApJ...503..744H.

M. Holler, D. Berge, J. Hahn, D. Khangulyan, R. D. Parsons, and for the H. E. S. S. collaboration. Advanced search for the extension of unresolved TeV sources with H.E.S.S.: First measurement of the extension of the Crab nebula at TeV energies. *ArXiv e-prints*, 1707:arXiv:1707.04196, July 2017. URL http://adsabs.harvard.edu/abs/2017arXiv170704196H.

C. F. Kennel and F. V. Coroniti. Magnetohydrodynamic model of Crab nebula radiation. *The Astrophysical Journal*, 283:710–730, August 1984. ISSN 0004-637X. doi: 10.1086/162357. URL http://adsabs.harvard.edu/abs/1984ApJ...283..710K.

D. A. Kniffen, R. C. Hartman, D. J. Thompson, G. F. Bignami, and C. E. Fichtel. Gamma radiation from the Crab Nebula above 35 MeV. *Nature*, 251:397–399, October 1974. ISSN 0028-0836. doi: 10.1038/251397a0. URL http://adsabs.harvard.edu/abs/1974Natur.251..397K.

Frank Krennrich. Gamma ray astronomy with atmospheric Cherenkov telescopes: the future. *New Journal of Physics*, 11(11):115008, November 2009. doi: 10.1088/1367-2630/11/11/115008.

L. Kuiper, W. Hermsen, G. Cusumano, R. Diehl, V. Schönfelder, A. Strong, K. Bennett, and M. L. McConnell. The Crab pulsar in the 0.75-30 MeV range as seen by CGRO COMPTEL. A coherent high-energy picture from soft X-rays up to high-energy gamma-rays. *Astr. Astrophys.*, 378:918–935, November 2001. doi: 10.1051/0004-6361:20011256.

J. C. Ling and Wm. A. Wheaton. Gamma-Ray Spectra and Variability of the Crab Nebula Emission Observed by BATSE. *Astrophys. J.*, 598(1):334–348, Nov 2003. doi: 10.1086/378700.

A. P. Lobanov, D. Horns, and T. W. B. Muxlow. VLBI imaging of a flare in the Crab nebula: more than just a spot. *Astronomy and Astrophysics*, 533:A10, September 2011. ISSN 0004-6361. doi: 10.1051/0004-6361/201117082. URL http://adsabs.harvard.edu/abs/2011A%26A...533A..10L.

A. G. Lyne, R. S. Pritchard, and F. Graham Smith. 23 years of Crab pulsar rotational history. *Month. Not. Roy. Astr. Soc.*, 265:1003–1012, December 1993. doi: 10.1093/mnras/265.4.1003.

Jonatan Martn, Diego F. Torres, and Nanda Rea. Time-dependent modelling of pulsar wind nebulae: study on the impact of the diffusion-loss approximations. *Monthly Notices of the Royal Astronomical Society*, 427:415–427, November 2012. ISSN 0035-8711. doi: 10.1111/j.1365-2966.2012.22014.x. URL http://adsabs.harvard.edu/abs/2012MNRAS.427..415M.

M. Mayer, R. Buehler, E. Hays, C. C. Cheung, M. S. Dutka, J. E. Grove, M. Kerr, and R. Ojha. Rapid Gamma-Ray Flux Variability during the 2013 March Crab Nebula Flare. *Astrophys. J.*, 775(2):L37, Oct 2013. doi: 10.1088/2041-8205/775/2/L37.

M. Meyer, D. Horns, and H.-S. Zechlin. The Crab Nebula as a standard candle in very high-energy astrophysics. *Astronomy and Astrophysics*, 523:A2, November 2010. ISSN 0004-6361. doi: 10.1051/0004-6361/201014108. URL http://adsabs.harvard.edu/abs/2010A%26A...523A...2M.

I. Mochol and J. Petri. Very high energy emission as a probe of relativistic magnetic reconnection in pulsar winds. *Month. Not. Roy. Astr. Soc.*, 449:L51–L55, April 2015. doi: 10.1093/mnrasl/slv018.

Alex G. Muslimov and Alice K. Harding. High-Altitude Particle Acceleration and Radiation in Pulsar Slot Gaps. *Astrophys. J.*, 606(2):1143–1153, May 2004. doi: 10.1086/383079.

T. Nguyen and VERITAS Collaboration. Updated results from VERITAS on the Crab pulsar. In *34th International Cosmic Ray Conference (ICRC2015)*, volume 34 of *International Cosmic Ray Conference*, page 828, Jul 2015.

Jérôme Pétri. Theory of pulsar magnetosphere and wind. *Journal of Plasma Physics*, 82(5):635820502, October 2016. doi: 10.1017/S0022377816000763.

M. J. Rees. Implications of the "Wave Field" Theory of the Continuum from the Crab Nebula. *Nature Physical Science*, 230:55–57, March 1971. ISSN 0300-8746. doi: 10.1038/physci230055a0. URL http://adsabs.harvard.edu/abs/1971NPhS..230...55R.

Roger W. Romani. Gamma-Ray Pulsars: Radiation Processes in the Outer Magnetosphere. *Astrophys. J.*, 470:469, October 1996. doi: 10.1086/177878.

J. D. Scargle, J. P. Norris, B. Jackson, and J. Chiang. Studies in Astronomical Time Series Analysis. VI. Bayesian Block Representations. *Astrophys. J.*, 764:167, February 2013. doi: 10.1088/0004-637X/764/2/167.

Anatoly Spitkovsky and Jonathan Arons. Time Dependence in Relativistic Collisionless Shocks: Theory of the Variable "Wisps" in the Crab Nebula. *The Astrophysical Journal*, 603:669–681, March 2004. ISSN 0004-637X. doi: 10.1086/381568. URL http://adsabs.harvard.edu/abs/2004ApJ...603..669S.

E. Striani, M. Tavani, V. Vittorini, I. Donnarumma, A. Giuliani, G. Pucella, A. Argan, A. Bulgarelli, S. Colafrancesco, M. Cardillo, E. Costa, E. Del Monte, A. Ferrari, S. Mereghetti, L. Pacciani, A. Pellizzoni, G. Piano, C. Pittori, M. Rapisarda, S. Sabatini, P. Soffitta, M. Trifoglio, A. Trois, S. Vercellone, and F. Verrecchia. Variable Gamma-Ray Emission from the Crab Nebula: Short Flares and Long "Waves". *Astrophys. J.*, 765(1):52, Mar 2013. doi: 10.1088/0004-637X/765/1/52.

J. Takata, S. Shibata, K. Hirotani, and H. K. Chang. A two-dimensional electrodynamical outer gap model for γ-ray pulsars: γ-ray spectrum. *Month. Not. Roy. Astr. Soc.*, 366(4):1310–1328, March 2006. doi: 10.1111/j.1365-2966.2006.09904.x.

Anisia P. S. Tang, J. Takata, J. J. Jia, and K. S. Cheng. A Revisit of the Phase-resolved X-Ray and Gamma-Ray Spectra of the Crab Pulsar. *Astrophys. J.*, 676(1):562–572, March 2008. doi: 10.1086/527029.

M. Tavani, A. Bulgarelli, V. Vittorini, A. Pellizzoni, E. Striani, P. Caraveo, M. C. Weisskopf, A. Tennant, G. Pucella, A. Trois, E. Costa, Y. Evangelista, C. Pittori, F. Verrecchia, E. Del Monte, R. Campana, M. Pilia, A. De Luca, I. Donnarumma, D. Horns, C. Ferrigno, C. O. Heinke, M. Trifoglio, F. Gianotti, S. Vercellone, A. Argan, G. Barbiellini, P. W. Cattaneo, A. W. Chen, T. Contessi, F. D'Ammando, G. DeParis, G. Di Cocco, G. Di Persio, M. Feroci, A. Ferrari, M. Galli, A. Giuliani, M. Giusti, C. Labanti, I. Lapshov, F. Lazzarotto, P. Lipari, F. Longo, F. Fuschino, M. Marisaldi, S. Mereghetti, E. Morelli, E. Moretti, A. Morselli, L. Pacciani, F. Perotti, G. Piano, P. Picozza, M. Prest, M. Rapisarda, A. Rappoldi, A. Rubini, S. Sabatini, P. Soffitta, E. Vallazza, A. Zambra, D. Zanello, F. Lucarelli, P. Santolamazza, P. Giommi, L. Salotti, and G. F. Bignami. Discovery of Powerful Gamma-Ray Flares from the Crab Nebula. *Science*, 331:736, February 2011. doi: 10.1126/science.1200083.

The Fermi-LAT collaboration. Fermi Large Area Telescope Fourth Source Catalog. *arXiv e-prints*, art. arXiv:1902.10045, Feb 2019.

Christopher Torrence and Gilbert P. Compo. A Practical Guide to Wavelet Analysis. *Bulletin of the American Meteorological Society*, 79(1):61–78, January 1998. doi: 10.1175/1520-0477(1998)079⟨0061:APGTWA⟩2.0.CO;2.

Virginia Trimble. Motions and Structure of the Filamentary Envelope of the Crab Nebula. *The Astronomical Journal*, 73:535, September 1968. ISSN 0004-6256. doi: 10.1086/110658. URL http://adsabs.harvard.edu/abs/1968AJ.....73..535T.

Virginia Trimble. The Distance to the Crab Nebula and NP 0532. *Astronomical Society of the Pacific*, 85(507):579, October 1973. doi: 10.1086/129507.

Sidney van den Bergh. A Jetlike Structure Associated with the Crab Nebula. *Astrophys. J. Letters*, 160:L27, April 1970. doi: 10.1086/180516.

VERITAS Collaboration, E. Aliu, T. Arlen, T. Aune, M. Beilicke, W. Benbow, A. Bouvier, S. M. Bradbury, J. H. Buckley, V. Bugaev, K. Byrum, A. Cannon, A. Cesarini, J. L. Christiansen, L. Ciupik, E. Collins-Hughes, M. P. Connolly, W. Cui, R. Dickherber, C. Duke, M. Errando, A. Falcone, J. P. Finley, G. Finnegan, L. Fortson, A. Furniss, N. Galante, D. Gall, K. Gibbs, G. H. Gillanders, S. Godambe, S. Griffin, J. Grube, R. Guenette, G. Gyuk, D. Hanna, J. Holder, H. Huan, G. Hughes, C. M. Hui, T. B. Humensky, A. Imran, P. Kaaret, N. Karlsson, M. Kertzman, D. Kieda, H. Krawczynski, F. Krennrich, M. J. Lang, M. Lyutikov, A. S. Madhavan, G. Maier,

P. Majumdar, S. McArthur, A. McCann, M. McCutcheon, P. Moriarty, R. Mukherjee, P. Nuñez, R. A. Ong, M. Orr, A. N. Otte, N. Park, J. S. Perkins, F. Pizlo, M. Pohl, H. Prokoph, J. Quinn, K. Ragan, L. C. Reyes, P. T. Reynolds, E. Roache, H. J. Rose, J. Ruppel, D. B. Saxon, M. Schroedter, G. H. Sembroski, G. D. Şentürk, A. W. Smith, D. Staszak, G. Tešić, M. Theiling, S. Thibadeau, K. Tsurusaki, J. Tyler, A. Varlotta, V. V. Vassiliev, S. Vincent, M. Vivier, S. P. Wakely, J. E. Ward, T. C. Weekes, A. Weinstein, T. Weisgarber, D. A. Williams, and B. Zitzer. Detection of Pulsed Gamma Rays Above 100 GeV from the Crab Pulsar. *Science*, 334(6052):69, October 2011. doi: 10.1126/science.1208192.

D. Volpi, L. Del Zanna, E. Amato, and N. Bucciantini. Non-thermal emission from relativistic MHD simulations of pulsar wind nebulae: from synchrotron to inverse Compton. *Astronomy and Astrophysics*, 485:337–349, July 2008. ISSN 0004-6361. doi: 10.1051/0004-6361:200809424. URL http://adsabs.harvard.edu/abs/2008A%26A...485..337V.

T. C. Weekes, M. F. Cawley, D. J. Fegan, K. G. Gibbs, A. M. Hillas, P. W. Kowk, R. C. Lamb, D. A. Lewis, D. Macomb, N. A. Porter, P. T. Reynolds, and G. Vacanti. Observation of TeV gamma rays from the Crab nebula using the atmospheric Cerenkov imaging technique. *The Astrophysical Journal*, 342:379–395, July 1989. ISSN 0004-637X. doi: 10.1086/167599. URL http://adsabs.harvard.edu/abs/1989ApJ...342..379W.

Colleen A. Wilson-Hodge, Michael L. Cherry, Gary L. Case, Wayne H. Baumgartner, Elif Beklen, P. Narayana Bhat, Michael S. Briggs, Ascension Camero-Arranz, Vand iver Chaplin, Valerie Connaughton, Mark H. Finger, Neil Gehrels, Jochen Greiner, Keith Jahoda, Peter Jenke, R. Marc Kippen, Chryssa Kouveliotou, Hans A. Krimm, Erik Kuulkers, Niels Lund, Charles A. Meegan, Lorenzo Natalucci, William S. Paciesas, Robert Preece, James C. Rodi, Nikolai Shaposhnikov, Gerald K. Skinner, Doug Swartz, Andreas von Kienlin, Roland Diehl, and Xiao-Ling Zhang. When a Standard Candle Flickers. *Astrophys. J. Letters*, 727(2):L40, Feb 2011. doi: 10.1088/2041-8205/727/2/L40.

M. Wood, R. Caputo, E. Charles, M. Di Mauro, J. Magill, J. S. Perkins, and Fermi-LAT Collaboration. Fermipy: An open-source Python package for analysis of Fermi-LAT Data. *International Cosmic Ray Conference*, 301:824, January 2017.

Paul K. H. Yeung. Inferring the origins of the pulsed γ-ray emission from the Crab pulsar with ten-year Fermi-LAT data. *Astr. Astrophys.*, 640:A43, August 2020. doi: 10.1051/0004-6361/202038166.

Paul K. H. Yeung and Dieter Horns. The Energy-dependent γ-Ray Morphology of the Crab Nebula Observed with the Fermi Large Area Telescope. *Astrophys. J.*, 875(2): 123, Apr 2019. doi: 10.3847/1538-4357/ab107a.

Paul K. H. Yeung and Dieter Horns. Fermi Large Area Telescope observations of the fast-dimming Crab Nebula in 60-600 MeV. *Astr. Astrophys.*, 638:A147, June 2020. doi: 10.1051/0004-6361/201936740.

Roberta Zanin. MAGIC measurement of the Crab Nebula spectrum over three decades in energy. In *International Cosmic Ray Conference*, volume 7 of *International Cosmic Ray Conference*, page 72, January 2011. doi: 10.7529/ICRC2011/V07/0195.

List of Listings

Listings

A.1 Ten-year ephemeris file of the Crab pulsar (Credit: Matthew Kerr) 61
B.1 Python code used to quantify transitional timescales between low-flux and intermediate states of the Crab Nebula (composed initially and mainly by Dieter Horns; modified by Paul K. H. Yeung) 65
B.2 Python code used to fit the PLSF model to the joint spectra of *Fermi* LAT & MAGIC for the pulse phases $P1_M$ & $P2_M$ of the Crab pulsar (composed initially and mainly by Dieter Horns; modified by Paul K. H. Yeung) 67

Acknowledgements

This thesis cannot be accomplished without the integration of scientific and humanistic spirits, as well as the intersection of rational and emotional minds. I am grateful that this project allowed me to investigate the renowned interstellar complex as a citizen of our beloved planet Earth.

First of all, I would like to thank my supervisor Prof. Dr. Dieter Horns for his adequate amount of supervision in these three years, his co-writing of my two first-author journal articles (Yeung and Horns, 2019, 2020), and his encouragement regarding my publication of one journal article as a single author (Yeung, 2020). Thanks must also be given to Dr. Martin Tluczykont and Dr. Andrei Lobanov for their useful comments during our internal group meetings. Moreover, I acknowledge the editors and anonymous referees who were in charge of the reviewing and editing processes of our journal publications.

I would like to express my appreciation to my colleagues from all over the world. My world grows wider because of them. Meanwhile, boundless appreciation must also be given to my family and friends who keep supporting me even when we are separated by thousands of kilometers.

It has really been worthwhile for me to travel a long way to study in Hamburg, because I was easily integrated into such a pluralistic society with mutual respect. I am grateful for the delightful environment where I can manage a good balance among work, life and sleep.

I acknowledge the support of the DFG under the research grant HO 3305/4-1, that we obtained from submitting a project proposal directly related to the sub-topic presented in Chapter 3. This proposal is mainly prepared by my supervisor. Over the past three years, I made good use of this funding for my works, publications and work-related travels. Also, I would like to thank the PIER Helmholtz Graduate School for the additional funding as well as training workshops.

Thanks to the group meetings, journal clubs as well as the international and local conferences, I keep broadening my astrophysical knowledge and sharpening my research intellect through communications with other researchers.

Notably, every failure I experienced is very important to me too, because these failures taught me that there are always more than one paths to success. Perplexities, hesitations and detours are all a part of research as well as a part of life. However, as long as the thoughts of different researchers are integrated and elaborated, a road leading to infinite potentiality will be created. I appreciate the enormous passion in my inner self towards High-Energy Astrophysics.

Furthermore, I give my sincere gratitude to my colleague Dr. Ludmilla Dirson who provided the initial template of this dissertation, and those who helped to improve this dissertation (including Dr. Jhilik Majumdar, Dr. Ludmilla Dirson, Dr. Martin Tluczykont as well as the evaluators Prof. Dr. Dieter Horns and Prof. Dr. Olaf Reimer).

Last but not least, I personally thank *Niantic, Inc.* for developing the augmented reality mobile game *Pokémon Go*, and thank *Nintendo* for developing the video game console *Nintendo Switch*. Their game products serve as my refreshers during my leisure time, so that I can maintain my passion and momentum when I get back to astrophysical research. I also thank those co-players of *Pokémon Go* in DESY Hamburg for enjoying the fun together. "Gotcha! Thesis is published!"

Publications constituting the major parts of this thesis

Refereed publications

Yeung, P. K. H. 2020, *"Inferring the origins of the pulsed gamma-ray emission from the Crab pulsar with ten-year Fermi LAT data"*, A&A, 640, A43

Yeung, P. K. H. & Horns, D. 2020, *"Fermi Large Area Telescope Observations of the Fast-dimming Crab Nebula in 60–600 MeV"*, A&A, 638, A147

Yeung, P. K. H. & Horns, D. 2019, *"The Energy-dependent γ-Ray Morphology of the Crab Nebula Observed with the Fermi Large Area Telescope"*, ApJ, 875, 123

Erratum

Yeung, P. K. H. & Horns, D. 2021, *'Erratum: "The Energy-dependent γ-Ray Morphology of the Crab Nebula Observed with the Fermi Large Area Telescope" (2019, ApJ, 875, 123)'*, ApJ, submitted, arXiv:1903.07527

Eidesstattliche Versicherung

Declaration on oath

Hiermit erklare ich an Eides statt, dass ich die vorliegende Dissertationsschrift selbst verfasst und keine anderen als die angegebenen Quellen und Hilfsmittel benutzt habe.

I hereby declare upon oath that I have written the present dissertation independently and have not used further resources and aids than those stated.

Hamburg
26th August, 2020
Unterschrift